NONLINEAR OPTICAL MICROSCOPY OF HIGHLY PIGMENTED TISSUES

By

Ilyas Saytashev

A DISSERTATION

Submitted to
Michigan State University
in partial fulfillment of the requirements
for the degree of

Chemistry – Doctor of Philosophy

2016

ABSTRACT

NONLINEAR OPTICAL MICROSCOPY OF HIGHLY PIGMENTED TISSUES

By

Ilyas Saytashev

The focus of this dissertation research project was to study the effect of near-IR and IR femtosecond pulses on a living organism via nonlinear optical microscopy (NLOM) of biological specimens. Laser parameters — wavelength, pulse duration, pulse energy and the spatial quality of the beam — were optimized to maximize nonlinear optical signals with minimal photodamage during deep (down to 0.3 mm) tissue microscopy imaging of non-transparent biological specimens. The photodamage in living tissues was assessed. Experimental techniques performed include the following: femtosecond pulse characterization; adaptive spatial and temporal pulse shaping; *in vivo* and *in vitro* depth-resolved multimodal nonlinear optical microscopy imaging; spectrally resolved one- and two-photon excitation fluorescence lifetime measurements; and the scoring of a photodamage on living *D. melanogaster*.

The experimental results are presented in four chapters. Chapter 2 describes three major topics: (1) the technical aspects of delivering compressed femtosecond laser pulses with optimal spatial properties into deep portions of a biological specimen; (2) pulse shaping for selective excitation; and (3) the simultaneous detection of different color two-photon excitation fluorescence (TPEF) optical signals using a single PMT detector. Chapter 3 describes the use of advanced laser sources, such as ultrabroadband Ti:Sapphire and Yb-fiber femtosecond lasers, in depth-resolved multimodal NLOM of biological specimens. A second-harmonic generation (SHG) microscopy of a fixed human skin demonstrated an 80% increase in attenuation length for a sub-40 fs, 1060 nm Yb-fiber oscillator in comparison to a >100 fs, 800 nm Ti:Sapphire laser. Chapter 4 describes the investigation of human red blood cells (RBC) using TPEF, third harmonic generation (THG) and three-photon excitation fluorescence (3PEF) microscopy imaging. Hemoglobin was the primary source of the TPEF signal in RBCs and their membranes, as determined by a comparison of spectrally resolved fluorescence lifetime decays of reagent-grade endogenous fluorophores, as well as linear and transient absorption measurements. THG imaging was performed on RBCs through a blood storage

bag to demonstrate THG's potential application in the non-invasive assessment of stored RBCs. Chapter 5 summarizes the experimental results and *in vivo* assessment of laser-induced damage during NLOM imaging in living *D. melanogaster*. Short-term photodamage occurred via a nonlinear process and was estimated by scoring the mechanical damage and fluorescence increase. In contrast, long-term photodamage exhibited a linear relationship with laser intensity and was scored by lethality, apoptosis and necrosis in irradiated *D. melanogaster* population. The study reveals the benefit of utilizing shorter pulses — 37 fs and shorter — for NLOM imaging of highly pigmented tissues wherein linear (thermal) damage is the greatest contributor to the overall photodamage of the living organism.

My research successfully demonstrates the potential use of femtosecond fiber-based and ultrabroadband solid state laser systems to overcome a key performance limitation of NLOM technology, while providing low barrier-to-access alternatives to current Ti:Sapphire sources. These results should accelerate the movement of noninvasive NLOM into clinical practice.

ACKNOWLEDGEMENTS

I would like to thank Prof. Olga Smirnova, my advisor at Bauman Moscow State Technical University, for recommending that I enter the MSU Ph.D. program. Without her advice, encouragement, and support, I would never have had a chance to study abroad.

Special acknowledgements to Prof. Marcos Dantus — my research advisor for the Ph.D. program in the Department of Chemistry. For the rest of my life, I will remember my advisor's lessons about time, money, and management. Thank you for everything – truly. I would never have finished the program without your supervision. Many thanks to my lab-mates Anton Ryabtsev and Gennady Rasskazov. I have known you both for more than ten years, and I have no doubts that our friendship will last a lifetime. Thanks to my lab-mates with whom I had the honor to work: Dr. Vadim Lozovoy, Dr. Sergey Arkhipov, Dr. Richa Mittal, Dr. Rachel Glenn, Dr. Marshall Bremer, Dr. Bai Nie, Dr. Arkaprabha Konar, Muath Nairat, Nelson Winkler and Kristen Zuraski.

During my Ph.D. program, I had many great opportunities to collaborate with research groups at MSU and other universities. I gratefully acknowledge my collaborators: Prof. Blanchard's, Prof. Beck's and Prof. Spence's groups at the Department of Chemistry, MSU; Prof. Evans' group at Harvard University; Prof. Tromberg and Dr. Mihaela Balu at the Beckman Laser Institute, UCI; Prof. Wise's group at Cornell University; and Dr. Stefano Bonora from IFN – CNR.

I am very grateful to Dr. Bingwei Xu and Dr. Dmitry Pestov from Biophotonic Solutions Inc. for all your help. Your support for the equipment, the opportunity to work with the latest ultrafast lasers, and valuable advice greatly influenced my research.

I would like to give a special thanks to my family, who being on the other side of the world believed in my success – every day, without any doubts and with great financial and moral support.

Last, but not least, my greatest acknowledgement goes to my beautiful girlfriend Mykala Ford and the Ford family. You are my best supporters every day. Thank you for having me in your life. Mykala, you were my every day motivation to finish this dissertation.

TABLE OF CONTENTS

LIST OF TABLES

LIST OF FIGURES

KEY TO ABBREVIATIONS

3D	Three dimensional
3PEF	Three-photon excitation fluorescence
AC	Autocorrelation
AO	Adaptive optics
AOPDF	Acousto-optic programmable dispersive filter
BBO	Beta barium borate
BP	Band-pass
CCD	Charge-coupled device
CW	Continuous-wave
DM	Deformable mirror
DNA	Deoxyribonucleic acid
FAD	Flavin adenine dinucleotide
FP	Fluorescent protein
FS-AOM	Fused-silica acousto-optic modulator
FWHM	Full width at a half maximum
GM	Goeppert-Mayer units
Hb	Hemoglobin
HWP	Half waveplate
IR	Infrared
KDP	Potassium dihydrogen phosphate
LC	Liquid crystal
LP	Low-pass
LSM	Laser scanning microscopy
MEMS	Microelectromechanical systems

MIIPS	Multiphoton intrapulse interference phase scan
NA	Numerical aperture
NAD	Nicotinamide adenine dinucleotide
NADH	Nicotinamide adenine dinucleotide, reduced
NIR	Near-infrared
NLOM	Nonlinear optical microscopy
NOPA	Nonlinear optical parametric amplifier
OPO	Optical parametric oscillator
PBS	Phosphate buffer solution
PCF	Photonic crystal fiber
PMT	Photomultiplier tube
PSS	Physiological salt solution
PVC	Polyvinyl chloride
QWP	Quarter waveplate
RBC	Red blood cell
ROS	Reactive oxygen species
SD	Standard deviation
SHG	Second harmonic generation
SLM	Spatial light modulator
SMF	Single mode fiber
SOD	Second order dispersion
SP	Short-pass
TCSPC	Time-correlated single photon counting
THG	Third harmonic generation
Ti	Titanium
T-L	Transform-limited

TOD	Third order dispersion
TPA	Two-photon absorption
TPEF	Two-photon excitation fluorescence
TUNEL	Terminal deoxynucleotidyl transferase dUTP Nick End Labeling
UV	Ultraviolet
WDM	Wavelength division multiplexer
Yb	Ytterbium

Chapter 1 Introduction

The interaction between light and matter is a fundamental process in the observable world. Naturally occurring examples of a linear dependence on the intensity of incoming light include colors of flowers, reflections in water, and the heating of a black stone by sunlight. These effects can generally be described as interactions between single units of light (photon) and matter (electron, atom, molecule or an ensemble of molecules). Photons from an incoherent light source, e.g., incandescent lamp and sun, are naturally random in their polarization, direction and phase due to spontaneous emission.

In 1931, Maria Goeppert-Mayer predicted that two photons could be absorbed simultaneously [1]. The probability of such an event, described as a two-photon absorption (TPA) cross-section, was calculated to be very small in the order of 10^{-50} cm^4 s photon^{-1} (1 GM); it would require a high intensity light pulse on the order of 10^{10} W/cm^2, which is an unprecedented power density for an incoherent light source. This power density is approximately 10^{11} times higher than the average power density of sunlight on Earth. The fundamental limit for increasing laser peak intensity without ionizing molecules is approximately 10^{14} W/cm^2 [2]. This value corresponds to ionization saturation intensity I_{sat} in complex molecules.

Nonlinear light-matter interactions were not experimentally observed until the 1960s [3], shortly after the laser was invented. High-intensity coherent light sources revolutionized optical applications by facilitating access to nonlinear optical effects in media; this was the foundation of nonlinear spectroscopy. In 1990, Denk *et al*. [4] applied nonlinear spectroscopy methods on the micrometer scale and generated an image, pixel-by-pixel, by recording a two-photon excitation fluorescence (TPEF) signal from each pixel. This optical signal provided a contrast mechanism for the first nonlinear optical microscopy (NLOM) image.

NLOM has a high sensitivity and specificity for detecting nonlinear optical signals. The primary focus of this dissertation is the systematic exploitation of light-tissue interactions for maximizing the detection of nonlinear optical signals and minimizing photodamage during NLOM. Discrimination of chemical and morphological changes between cancerous cells and normal cells via different contrast

mechanisms of multimodal NLOM has direct biomedical applications, including diagnostics and therapy. The use of NLOM for noninvasive biopsies for cancer detection is explained in the following section.

1.1 Biomedical relevance of NLOM

Determining the malignancy of a tumor using an established diagnosis protocol can take several weeks because it includes visits to an oncologist, obtaining a tissue sample (biopsy), and further histopathological analysis of the biopsied material. A late or missed diagnosis of a primary cancerous tumor increases the chances that cancer cells will enter the blood circulation where a single cancer cell may lead to a secondary tumor; this significantly lowers the patient's survival. There are two primary risks associated with the above-described diagnosis protocol that increase the probability of metastasis. First, if a patient has a malignant tumor at the time the tumor is diagnosed, the tumor may grow into a blood vessel and cancer cells may be released into the blood circulation. Secondly, there is a risk associated with the invasiveness of biopsy; during a surgical cut or puncture, parts of biopsied tissue can come into direct contact with a blood vessel [5].

Fast non-invasive biopsies promise a higher chance of timely detection of cancerous cells along with a decreased risk of accidental transfer of cancer cells into the patient's blood stream. NLOM provides visual information about processes with sub-micrometer resolution; it is a great candidate for non-invasive biopsies — especially for skin cancer diagnosis. More than two decades after the first demonstration of laser-scanning TPEF microscopy [4], NLOM moved from proof-of-concept experiments that demonstrated the capabilities of different contrast mechanisms in living tissues [6] to becoming a valued tool in clinical research centers. Sub-micrometer resolution, chemical specificity, and precise 3D reconstruction of imaged volume at depths down to 1.2 mm [7] are becoming a necessity in tissue examinations [8] for high specificity and accuracy in diagnosing cancers.

1.2 NLOM imaging methods

A typical NLOM setup is presented in Figure 1. The key components are further discussed in Chapters 2 and 3. The presented laser-scanning microscopy technique utilizes the excitation beam from a femtosecond optical source (laser oscillator or a supercontinuum generator) focused by a high numerical aperture (NA) objective on a sample. The position of the beam on the sample is determined by a pair of galvanometer scanning mirrors. The nonlinear optical signal generated from each pixel is collected by the excitation objective in the backward (epi) direction or by a collection objective in the forward (trans) direction. The collected signal is usually separated from an excitation laser beam by a dichroic mirror and filtered by a combination of short-pass (SP) and/or band-pass (BP) filters and detected by a photomultiplier tube (PMT) detector, CCD, or CMOS camera. By varying the scanning speed of the galvanometer mirrors, the irradiation time of each pixel and the frame rate are adjusted. Multiple image frames are taken and averaged to increase the signal-to-noise ratio.

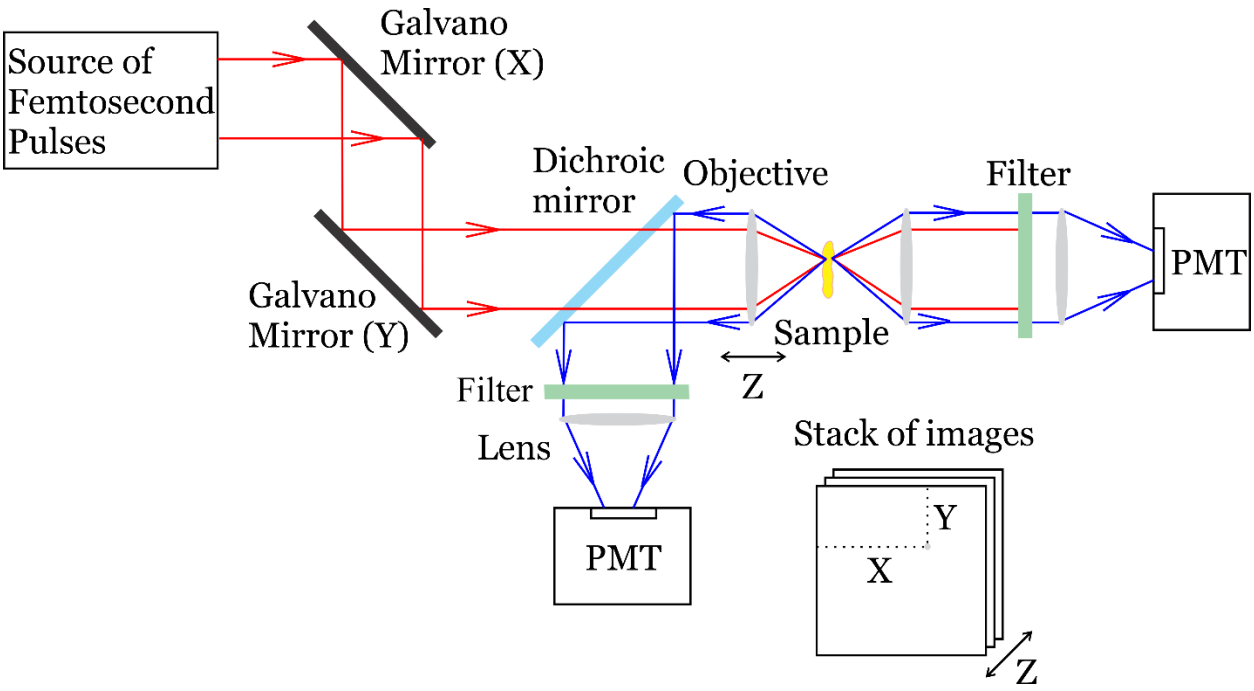

Figure 1. Schematic diagram for NLOM setup.

1.2.1 Harmonic generation

There are multiple nonlinear processes, so called parametric processes, which do not lead to an energy transfer between light and matter. In Jablonski diagrams, such processes are described as transitions to transient "virtual" states and then back to the ground state. The difference is only in the number of photons involved; see Figure 2. When two photons at frequency ω (wavelength λ) are converted into a single photon at frequency 2ω (wavelength $\lambda/2$), the process is referred to as second harmonic generation (SHG) [9]. If three photons at frequency ω are "absorbed" to reach the virtual state and "emit" a single photon at 3ω, it is called third harmonic generation (THG). In a similar manner, one can generalize the process for *n*-harmonic generation; however, one can rarely go beyond SHG and THG for NLOM imaging of biological tissue, because of the requirement for the low linear absorption in spectral regions for the fundamental and harmonic generation wavelengths [8].

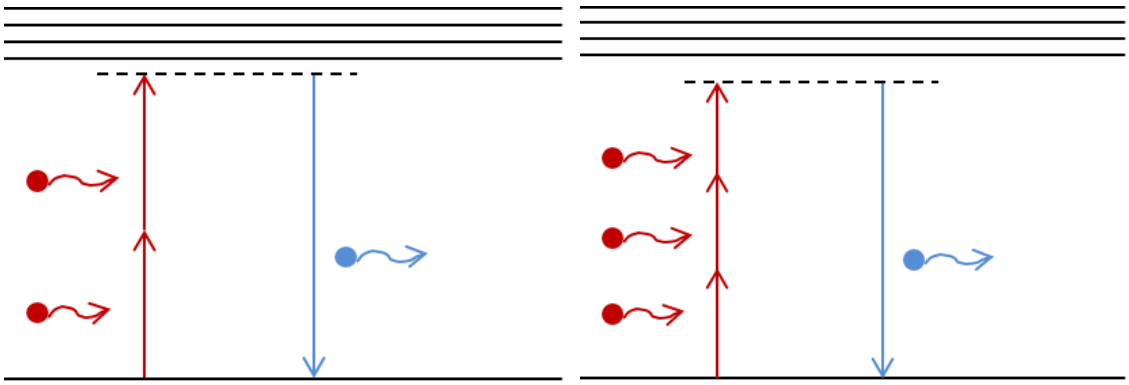

Figure 2. Jablonski diagram for second harmonic generation (SHG, left) and third harmonic generation (THG, right).

For SHG, a non-zero second-order susceptibility is required. In a cento-symmetric molecule, the time-dependent polarization should not depend on the sign of an applied electric field due to the symmetry. This requirement leads to vanishing even components of a nonlinear susceptibility, and therefore no SHG can be generated. The lack of local central symmetry in the media leads to non-vanishing second-order susceptibility. This condition is satisfied at surface monolayers; more importantly, it can be fulfilled by non-central symmetric molecules in bulk materials. In addition, phase matching between fundamental and SHG waves requires birefringence in the media. In NLOM of biological tissues, fibrous protein structures

produce a strong SHG signal due to high second-order susceptibility and birefringence [10]; examples include rat tendons, which are rich in collagen and elastin (Figure 3, left) and protein depositions in bacteria (Figure 3, right). Therefore, SHG imaging is a proper modality to highlight those.

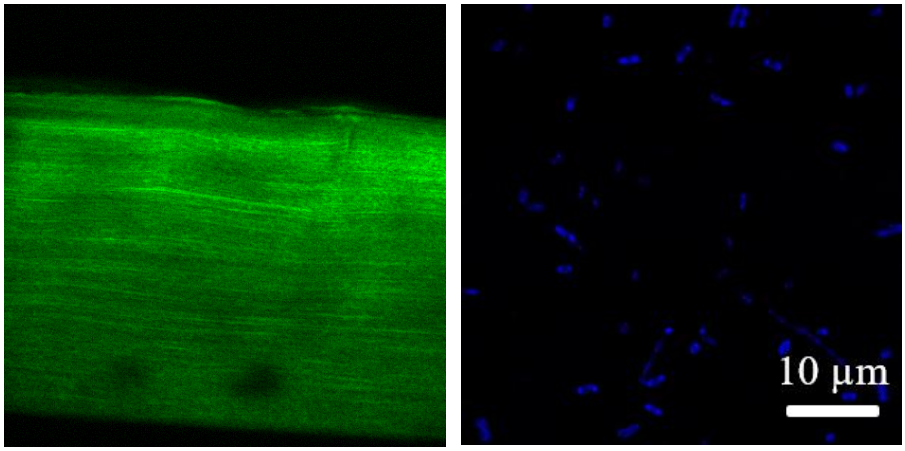

Figure 3. SHG image of a rat tendon (left) and *E.coli* bacteria, producing protein deposits (right). Both images were taken using sub-15 fs pulses centered at 800 nm from a Ti:Sapphire oscillator.

A majority of molecules possess third-order susceptibility, required for THG [11] on a molecular level. For a focused Gaussian beam, the spatial phase, or also called Gouy phase, changes its sign going through a focal plane [12]. Because of this change in sign, the THG before and after the focal plane destructively interferes, and therefore no THG is observed in homogeneous media. An abrupt change in the index of refraction, dispersion, or third-order susceptibility creates a wave vector compensation required for phase matching between the fundamental field, third harmonic, and Gouy phase shift mismatch wave vectors [13] (Figure 4, left). Therefore, THG imaging is most suitable for visualizing interfaces [14], such as lipids in water, membranes, organelles or sub-cellular optical inhomogeneities that are smaller than the beam focusing size [15]. Figure 4, right, shows a THG microphotograph of the trachea obtained from a living, unstained, undissected *D. melanogaster* larva. Lipid cells, trachea, and blood vessels can be easily identified because of the changes of the refractive index at the water interface.

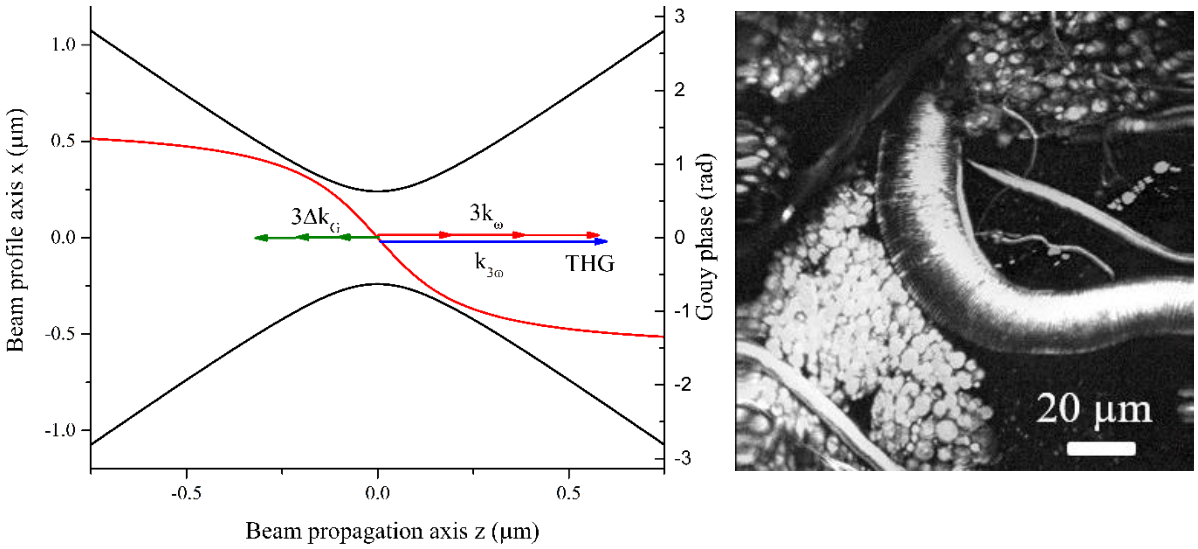

Figure 4. Left panel: schematic representation of Gouy phase in a focused Gaussian beam. The compensation of a mismatch wave vector, introduced by Gouy phase is required for satisfying phase matching condition in THG. Right panel: THG imaging of trachea region 30 μm under the cuticula in unstained, unlabeled undissected *D. melanogaster* larva using Yb-fiber oscillator.

Signal intensity of SHG and THG depends on the laser intensity squared and cubed, respectively. The difference in symmetry or the index of refraction implies different efficiency and, therefore, different intensity of nonlinear signals. Unlike THG, SHG microscopy is only available for non-centrosymmetric structures; therefore, it is important to use THG imaging [11] to provide information about the structure and components inside the living tissue.

1.2.2 Multiphoton excited fluorescence

Unlike SHG and THG, there are non-parametric nonlinear optical processes that involve transitions to real excited states, dephasing, and radiative decay to the ground state; see Figure 5. The radiative decay to the ground state is referred to as fluorescence. Multiphoton excitation fluorescence microscopy has been demonstrated with an absorption of up to four photons [16, 17].

A two-photon absorption (TPA) cross-section describes how efficiently the molecule can absorb two photons of the same energy to become excited. Figure 6 shows a TPA cross-section for a few common fluorophores. Endogenous NADH has a significantly different TPA than fluorescent proteins (FP), which

are designed for genetically encoded labeling in living cells. Because the energy level configurations are specific for different molecules, TPA and TPEF provide a chemical specificity for NLOM. Chapters 2 and 3 demonstrate this chemical specificity through selective excitation of fluorescent molecules.

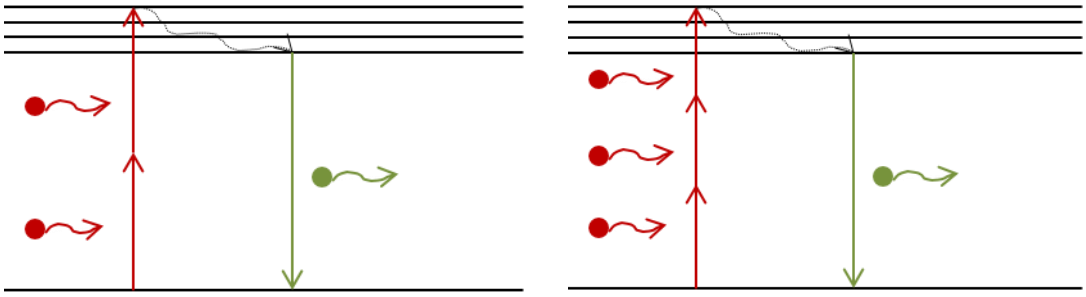

Figure 5. Jablonski diagram for two-photon (left) and three-photon (right) excitation fluorescence.

The probability of the emission of a photon is proportional to the absorption rate; therefore, the higher the TPA, the higher the fluorescence signal is expected to be for a given laser intensity. Further mathematical analysis of the relationship between nonlinear signal, TPA and excitation laser intensity is presented in the following section.

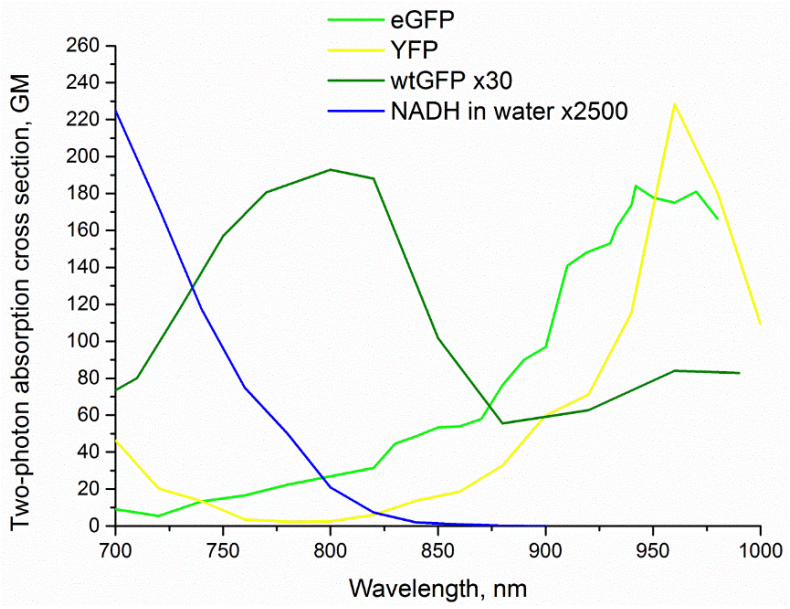

Figure 6. Two-photon absorption cross-section of various fluorophores. Adapted from http://www.drbio.cornell.edu/cross_sections.html

1.2.3 Effect of pulse duration on the nonlinear signal from the living tissue

For a pulsed irradiation, the *n*-photon absorption rate per second is given by:

$$R_a^{(n)} = f \frac{\sigma_n}{(hc/\lambda)^n} \int_0^{1/f} I^n(t)dt \quad (1)$$

where $R_a^{(n)}$ is the *n*-photon absorption rate, *f* is the repetition rate of laser pulses, *h* is Plank's constant, *c* is the speed of light, λ is the center wavelength, σ_n is n-photon absorption cross section, and *I(t)* denotes the slowly-varying intensity of the excitation laser light. If the intensity profile approximates a Gaussian shape, the *n*-photon absorption rate can be estimated as:

$$R_a^{(n)} = R_0 \times {I_p}^n \times \tau = R_0 \times \frac{E_p^n}{\tau^n} \times \tau = R_0 \times \frac{E_p^n}{\tau^{n-1}} \quad (2)$$

where I_p is the peak intensity of the pulse, E_p is pulse energy, τ is full width at the half maximum (FWHM) pulse duration, and R_0 is a constant.

The *n*-photon signal coming out of a sample is proportional to the absorption rate. The signal, in arbitrary units (a.u.) and ignoring the constants, can be calculated as following:

$$S_p^{(n)} \propto \frac{E_p^n}{\tau^{n-1}} \quad (3)$$

Therefore, the total *n*-photon signal is proportional to the pulse energy in the power of *n* and inversely proportional to the pulse duration in the power of *(n-1)*.

Since the efficiency of multiphoton microscopy is inversely proportional to the pulse duration in *(n-1)* power [18], shorter pulses lead to an increased, nonlinear optical signal. This dependence has been confirmed experimentally for two-photon microscopy [19]. Figure 7 illustrates the effect of pulse broadening in NLOM of living, undissected, unstained *D. Melanogaster* larva. While the average laser power was maintained at the same level of 15 mW at the focal plane of a 40x/1.1NA water immersion objective, pulse duration was changed by narrowing the bandwidth of a Ti:Sapphire oscillator output. This example demonstrates a higher TPEF signal when shorter pulses are used. The quantitative signal from lipid cells, measured as the average intensity of pixels 120 to 200 (Figure 7, bottom), is 14.9 and 5.2 for excitation with 13 fs and 37 fs FWHM duration pulses, respectively. The calculated ratio between two-photon signals – 2.86 – is very close to a theoretical prediction of 2.85, based on the ratio of pulse durations.

For broadband lasers, it is critical to ensure the delivery of short pulses to the focal plane of an objective to ensure maximum nonlinear excitation efficiency; methods and instrumentation to achieve this task are described in the next chapter.

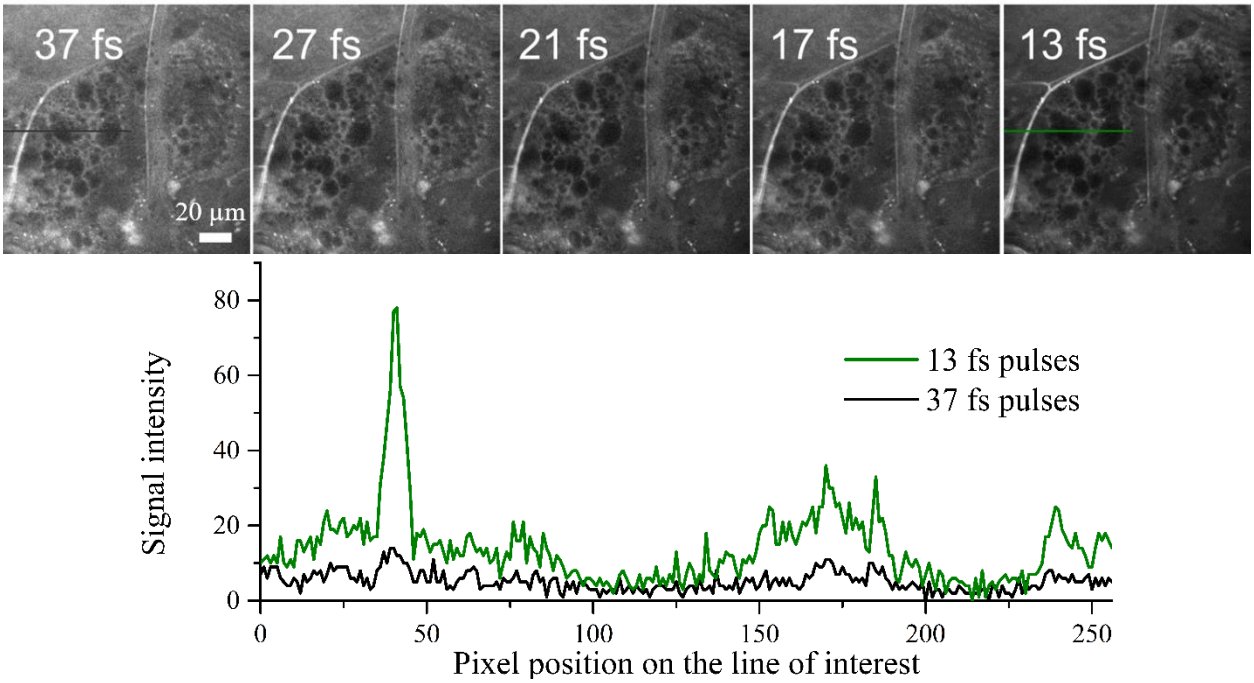

Figure 7. TPEF images of unstained, undissected *D. melanogaster* larva fat tissue region excited by fs pulses of a different FWHM duration from a Ti:Sapphire oscillator with constant 15 mW average power after the objective. The intensity profile of a selected line of pixels shows the benefit of using shorter pulses for NLOM.

Chapter 2 Adaptive spatial and temporal optimization of ultrashort pulses for detection of nonlinear optical signals

Two-photon microscopy is commonly used for obtaining 3D images of thick, up to few hundred micrometers, biological samples [20]. To ensure the delivery of femtosecond pulses at the focal plane of a high NA objective, it is necessary to compensate the accumulated dispersion of the laser pulses during propagation through optical elements in the multiphoton microscopy setup. The overall second order dispersion (SOD) introduced by optical components in typical multiphoton microscopy setup can achieve up to 8000 fs^2; the main contribution of 6000 fs^2 is from a high NA objective. For example, a 100 fs pulse almost doubles in duration after a 40x/1.1NA objective; a 12 fs pulses passing through the same objective would be broadened 116 times, becoming 1.4 ps in duration. It is necessary to compress the pulse at the focal point of the objective [19] to maximize the intensity of laser pulses for effective nonlinear excitation in multiphoton microscopy.

A non-Gaussian spatial profile of a laser beam, misalignment and imperfections in optics lead to optical distortions of a focused laser beam, also called aberrations. Additionally, the image quality degrades with depth in the sample because of aberrations that are generated by the refractive index change induced by the sample morphology [21, 22]. The presence of aberrations increases the size of a focusing spot; this decreases the intensity of a focused beam and, consequently, the efficiency of multiphoton excitation (see Equation 1). A theoretical limit for the focused spot size in the optical system without aberrations is defined by a diffraction [23]. To achieve a spot size that is closest to a diffraction limit, we introduced adaptive optics (AO) compensation of aberrations into the NLOM setup.

The results of spatio-temporal adaptive pulse shaping have demonstrated twice higher brightness level in images with a wavefront correction compared to ones without a wavefront correction. Methods for selective excitation, quadrature detection of fluorescence are described in this chapter.

2.1 Pulse characterization and pulse compression for multiphoton microscopy

The laser field can be described in terms of spectral amplitude, *E(ω)*, and spectral phase, *φ(ω)*, which are related to the temporal field, *E(t)*, and temporal phase, *φ(t)*, via Fourier transform. Laser intensity, which is proportional to the absolute value of the field squared ($|E|^2$) in both the time and spectral domains, cannot be directly measured in the time domain because of the slow response of any measuring device compared to the pulse duration. However, the spectral power density, *I(ω)*, can be routinely measured by a spectrometer. For a fixed spectral amplitude, *E(ω)*, changes in the spectral phase *φ(ω)* would change the temporal shape of the pulse as can be seen from a Fourier transform. To have the shortest pulse duration, the spectral phase should be either constant or linearly dependent on frequency *ω*. In this case, the pulse profile is determined by the Fourier transform of the spectral amplitude alone (transform-limited pulse).

Pulse broadening associated with linear chirp, or second order dispersion (SOD), for the pulse with a Gaussian-shaped spectrum can be described as the following [24]:

$$\tau/\tau_{TL} = \sqrt{1 + (4ln2)^2 \left(\varphi''/\tau_{TL}^2\right)^2} \qquad (4)$$

where φ'' is the quadratic term of the phase $\varphi(\omega) = 0.5\varphi''(\omega - \omega_0)^2$; τ_{TL} is a FWHM duration of a transform-limited (T-L) pulse. While grating pairs, static prisms and chirp mirrors, which are commonly used compression tools in multiphoton microscopes, easily compensate for linear chirp, they lack the ability to fully compensate higher order dispersion. It is critical to characterize and compress the laser pulses by measuring the spectral phase at the focus of an objective and applying the same negative phase (compensation mask) as shown in Figure 8, left [25].

A folded 4-f pulse shaper (Figure 9), which is placed after the oscillator and before the microscope, measures and compresses the laser pulses at the focal point of the objective. By placing the KDP (or BBO) crystal at the focal point of the objective and monitoring the SHG signal using a spectrometer, it is possible to measure and compress laser pulses using adaptive pulse compression via multiphoton intrapulse interference phase scan (MIIPS) [26]. This process ensures that all accumulated phase distortions, including

those that come from the not fully compressed laser source output itself and those accumulated from the laser output to the destination (focal spot of an objective), are corrected. Adaptive pulse compression [26] makes it possible to optimize (maximize) the amount of the nonlinear signal and perform pulse compression for different objectives and optics that might be necessary to add during NLOM imaging.

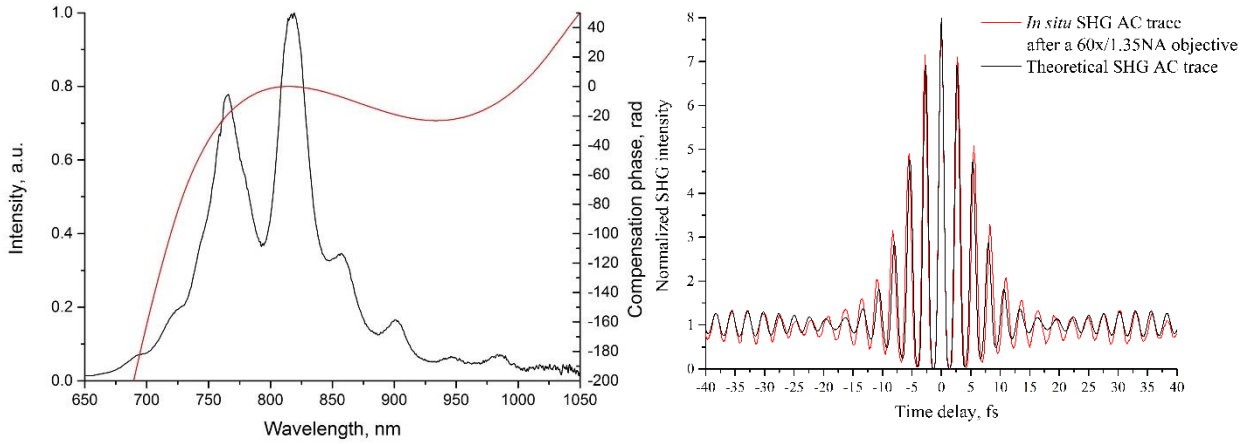

Figure 8. Left: fundamental IR spectrum (black) with compensation phase applied (red); Right: experimental (red) and theoretical (black) SHG AC comparison of a compressed laser pulses at the focal spot of a 60x/1.35NA objective.

In this example, the dispersion compensation is performed using the pulse shaper (Figure 9) [25, 26] as follows. A thin doubling KDP crystal, mounted on a microscope cover slide, is placed at the focus of the objective. The generated SHG signal from the crystal is collected by a spectrometer connected to a computer, which is also used to control the liquid crystal spatial light modulator (LC-SLM). The MIIPS software scans the reference phase functions across the spectrum of the pulses and uses the SHG spectral information to calculate the corresponding spectral phase distortions. After the first iteration, a compensation mask is generated and applied to the SLM to correct the phase distortions. These iterations are repeated several times until the pulses are compressed to within 99% of the theoretical transform limit, as defined by the Fourier transformation of the fundamental laser spectrum. The negative phase to that measured is applied by the pulse shaper to render the T-L pulses at the focal plane of the objective.

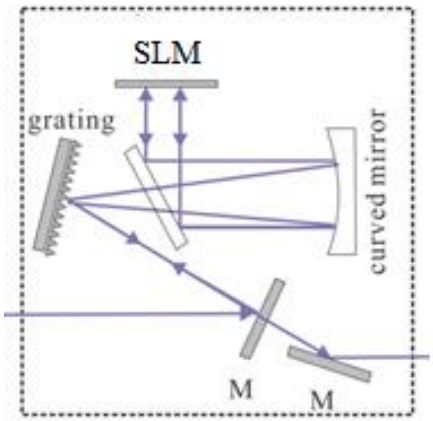

Figure 9. Schematic layout of a folded 4-f pulse shaper.

After pulse compression, the pulse shaper is used to create a two-pulse replica and to scan one of them in time to obtain an *in situ* interferometric autocorrelation [27, 28]. The experimental and calculated interferometric autocorrelation traces are also compared and match very well (Figure 8, right).

The following subsection demonstrates an example of pulse shaping of femtosecond pulses centered at 400 nm for studying molecular dynamics in Coumarin 460.

2.1.1 Deformable mirror for adaptive pulse shaping at 400 nm wavelength

4f pulse shapers based on a liquid crystal spatial light modulator (LC-SLM) has been proven to be an indispensable tool that provides phase and amplitude control over laser pulses ranging from the visible to the near-IR region, making the possible to take experimental coherent control on many physicochemical processes [29-33] and study molecular dynamical properties at the femtosecond timescale [34-37]. However, the LC-SLM draws back on wavelengths longer than 1.6 μm and shorter than 400 nm [38]. MEMS- [39] and AO-based [40] 4-f pulse shapers have been shown to be useful for pulse shaping around 400 nm; with deep UV pulses, FS-AOM [41] and AOPDF [42] shaping were proposed for use in molecular dynamics and quantum control experiments. However, the complexity of MEMS mirrors, acoustic absorption in AO crystals, and the interdependence of optical frequencies in AOPDF [43] limits the versatility of such instruments. Recently, it was shown how to utilize a deformable mirror (DM) in the Fourier plane of a 4-f shaper to phase shape mid-IR and ultra-broadband pulses [44, 45]. To study the

molecular fluorescence response of a UV absorbing dye Coumarin 460, the DM was utilized for shaping the 400 nm pulses.

The aluminum-coated bimorph DM [46] is composed of a 2 mm thick BK7 passive substrate glued to a 200 μm thick piezoelectric ceramic actuator. The piezo actuator is divided into 32 segments each connected to a +/-125 V voltage amplifier. The mirror size was 40 mm x 10 mm. The initial shape of the deformable mirror was spherical and it was possible to remove it with the application of a bias voltage of 40 V to all the actuators with a residual rms deviation from flat of 8.32 nm (123 nm Peak to Valley) as reported in Figure 10. The deformable mirror was operated in an open loop with a similar procedure as previously reported [44]. In brief, the DM was calibrated using a ZYGO interferometer (Zygo Corporation, Middlefield, CT) with the acquisition of the deformation given by each single actuator *e(x)* (so-called influence functions). For example, the deformable mirror deformation by the application of +125V to several electrodes is reported in Figure 10. To operate the deformable mirror, we modelled it as a linear device; therefore, the shape of the deformable mirror surface *S(x)* can be calculated as the linear combination of the influence functions.

$$S(x) = \sum_{i=1}^{32} e_i(x) c_i, \qquad (5)$$

where the control vector *c* [-1/+1] is proportional to the voltage applied to each single electrode.

The calculation of the control vector *c* that generates a determined DM *S(x)* can be carried out inverting Equation 5. To this purpose, we mounted the deformable mirror in the experimental setup as illustrated in Figure 11A and mapped the wavelength position on the DM surface with the use of a spectrometer. In this way, we were able to calculate the DM shape necessary to generate a determined spectral dispersion according to the formula:

$$\Delta\varphi(x) = 2\frac{2\pi}{\lambda(x)}\Delta S(x) \qquad (6)$$

where $\Delta\varphi(x)$ is the spectral phase and $\lambda(x)$ is the wavelength map on the deformable mirror. As an example, Figure 10 reports the DM shapes necessary to generate SOD (quadratic phase), which are then used in the experiment.

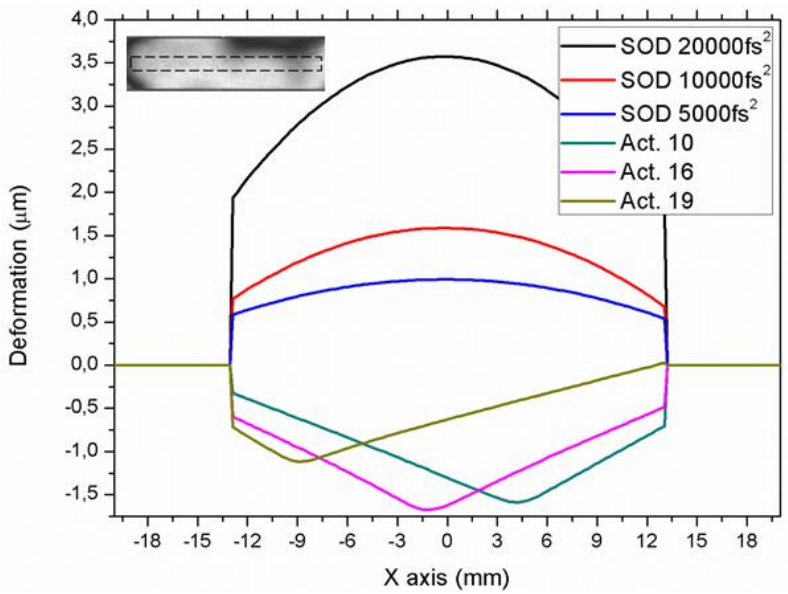

Figure 10. Example of measurement mirror deformation caused by the application of 125V to the electrodes 10, 16, 19 and examples of mirror deformation relative to the generation of second order dispersion. The inset reports the interferogram relative to the deformable mirror surface in the flat position measured with the Zygo interferometer.

Near infrared (NIR) pulses centered at 800 nm (Figure 11B) from a regeneratively amplified Ti:Sapphire laser at a 1 kHz repetition rate (Spectra-Physics, Santa Clara, CA) were compressed using a MIIPS-HD (Biophotoinc Solutions Inc., East Lansing, MI) phase and amplitude pulse shaper placed after the amplifier [25, 29, 47]. Compressed NIR T-L pulses out of the MIIPS-HD shaper were directed into a BBO crystal to generate the second harmonic pulses centered at 400 nm wavelength (Figure 10C). These pulses were sent into another 4-f pulse shaper with a 4 cm DM in the Fourier plane as shown in Figure 11A. In order to spread a 400 nm centered spectrum across the DM, we used a 2000 mm^{-1} aluminum UV coated grating. In this configuration, the beam illuminated 24 mm on the deformable mirror, which corresponds to about 20 actuators.

By changing the curvature of a DM, the spectral phase was applied to 400 nm centered femtosecond pulses. In order to calibrate the DM shaper, 800 nm pulses were used and SHG yield was compared with a calibrated MIIPS-HD shaper (Figure 12).

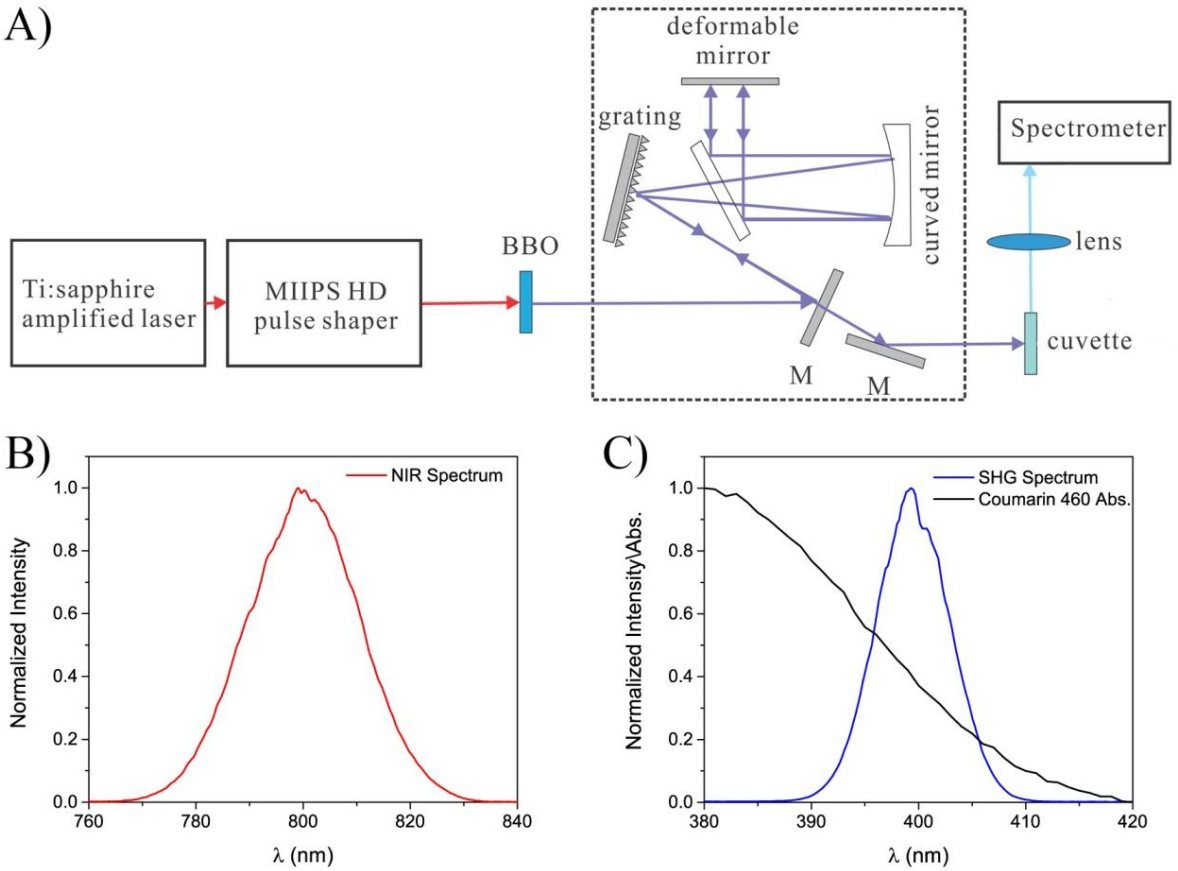

Figure 11. (A) Schematic diagram of an experimental setup; (B) NIR spectrum of a Ti:Sapphire amplified laser; (C) spectrum of 400 nm pulses, used for fluorescence study.

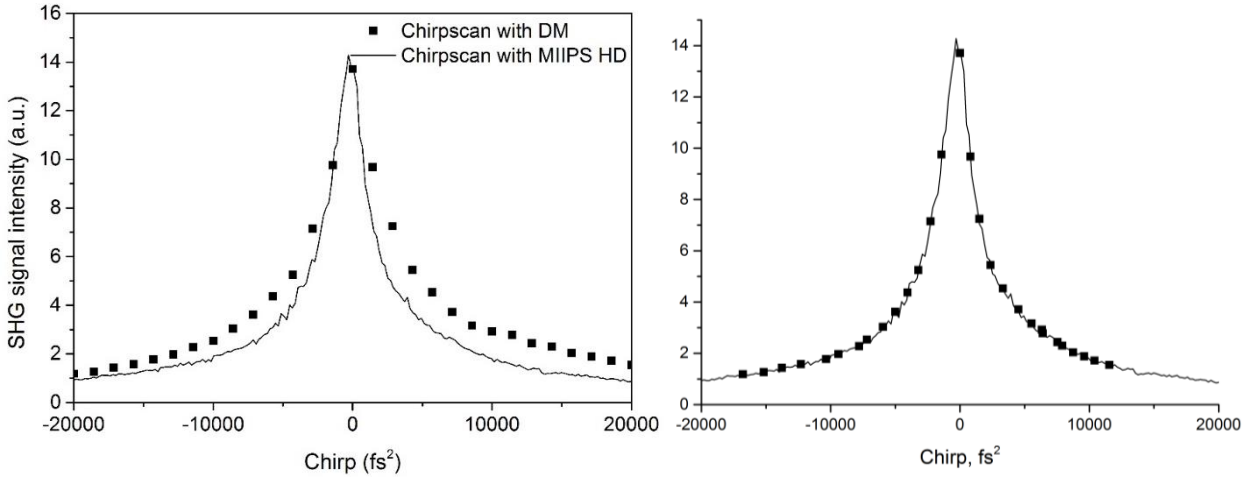

Figure 12. The comparison of an integrated SHG yield versus chirp (SOD) applied by a MIIPS-HD pulse shaper and a pulse shaper with a DM to 800 nm centered pulses before (left) and after (right) correction.

The output 400 nm centered pulses were used to study the fluorescence behavior of Coumarin 460 dye (Exciton, 100 μM in methanol). The fluorescence spectrum was collected at a right angle using a lens and a compact spectrometer while introducing a quadratic phase mask using the DM. The high frequency components (blue part of the pulse) arrive before the low frequency components (red part of the pulse) for a negatively chirped pulse, while the order of arrival is reversed for a positively chirped pulse.

The obtained integrated fluorescence signal from Coumarin 460 as a function of spectral chirp was normalized with the collected signal using T-L pulses (Figure 13). A depleted fluorescence signal was obtained using negatively chirped pulses compared to positively chirped ones. The fluorescence depletion by a negatively chirped pulses can be accounted for by using the arrival order of the frequencies from blue to red, which allows stimulated emission to occur and enhance the excited state depletion before fluorescence is achieved. On the other hand, fluorescence enhancement can be seen when excitation is carried out using positively chirped pulses, in which the arrival order of the frequencies is from red to blue, an order that doesn't permit stimulated emission to occur. Once the excited state is reached the time ordering of frequencies acts as it can stimulate the transition back to the ground state and back again to the excited state [34]. Moreover, the fluorescence enhancement gradually increases as the positive chirp value increases, an effect that was previously seen using the cyanine dye IR144 [48], which is known to have a decrease in its dipole moment upon electronic excitation, hence undergoing polar solvation [49]. Coumarin 460 structure has several coupled lone pairs on O and N that are conjugated with the π electronic system, in which some lone pairs can contribute to ground state resonance structures that do not contribute to the excited state. Therefore, a change in its dipole moment is caused upon excitation, hence permitting polar solvation. Moreover, it is also known that for N-substituted coumarins (including Coumarin 460), the fluorescence quantum yields and the life times are sharply reduced in polar solvent [50]. This fact indicates the sensitivity of Coumarin 460 toward the intermolecular environment, in which the early dynamical responses are highly sensitive to positively chirped pulses [34].

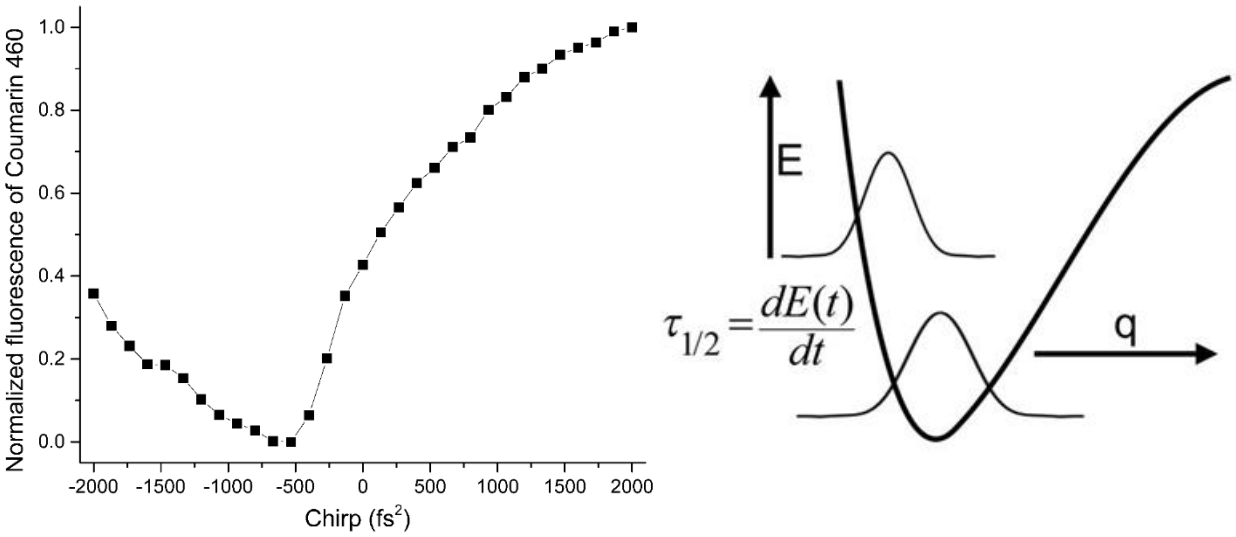

Figure 13. Left: normalized fluorescence intensity of Coumarin 460 as a function of spectral chirp on the 400 nm excitation pulse. Right: a diagram of an excited state potential energy of a molecule representing the rate of energy relaxation.

An interesting feature in Figure 13, left, is the maximum fluorescence depletion point, which is at around -500 fs^2, a feature that is associated with the intra- or inter-molecular energy relaxation of the electronically excited state of dye molecule and appears when the rate of relaxation is equal to the changing carrier frequency of the chirped pulse (Figure 13, right). This method makes it possible to directly measure the rate of relaxation of excess energy delivered by a laser pulse in the samples.

2.2 Adaptive lens for multiphoton imaging optimization

Adaptive optics is often implemented in optical setups incorporating a deformable mirror and a wave front sensor. This possibility is impractical in deep tissue microscopy; therefore, the literature presents different solutions. Booth *et al.* [21] demonstrated that aberration correction can be obtained in microscopy using an image-based optimization algorithm without the use of the wavefront sensors. This technique has been successfully applied to confocal [21], two-photon [22], multiharmonic [51], and single molecule microscopy [52]. Recently, pupil segmentation with liquid crystals correctors has been used to correct aberrations in thick samples with two-photon microscopes.

To increase the images contrast, it is necessary to achieve the highest possible intensity on the sample, thus reducing both temporal and spatial spreading of the laser pulse because of dispersions and

aberrations. The optimization of the image contrast has been demonstrated in both time and space separately. In this study, an automatic technique to achieve both space aberrations and time dispersion compensation of the sample on the same microscope is demonstrated.

The Yb-fiber oscillator with 40 MHz repetition rate pulses [53] was coupled to a 4-f pulse shaper MIIPSBox640 (Biophotonic Solutions Inc., East Lansing, MI) in order to eliminate spectral phase distortions and achieve T-L pulses at the focus of a Zeiss LD-C Apochromat 40x/1.1NA water immersion objective. Adaptive optics lens were placed in the beam path between the pulse shaper and a Nikon TE200 inverted microscope, modified for performing NLOM laser scanning (Figure 14). A two-photon signal (a combination of SHG and TPEF) was filtered out of an excitation beam by a LP dichroic mirror and a SP filter in epi-direction and collected by a PMT detector.

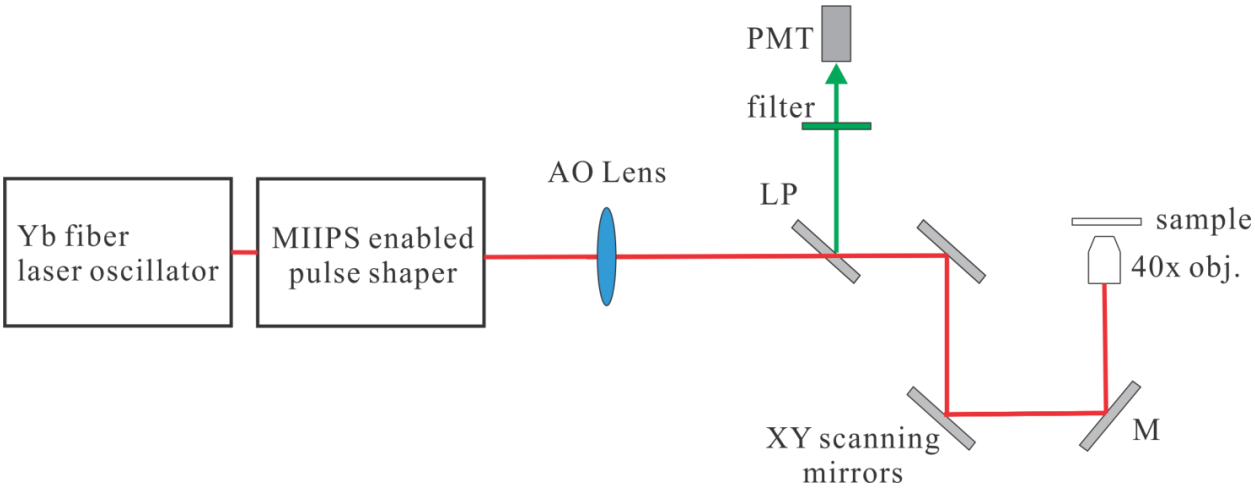

Figure 14. Schematic diagram of a laser scanning microscopy setup with temporal and spatial shaping of an excitation laser beam.

It is necessary for such short pulses to compensate for the dispersion introduced by optics on the beam path and the objective. Without such compensation (pulse compression), the estimated pulse duration is about 3 ps. The accumulated spectral phase distortions were measured and corrected using MIIPS. With a compensation mask applied, the FWHM pulse duration is estimated to be around 45 fs.

As shown in Figure 15, the compensation phase has a significant parabolic contribution that primarily comes from the objective (~ 6000 fs^2) and the output of the Yb-fiber laser itself (~ 35000 fs^2).

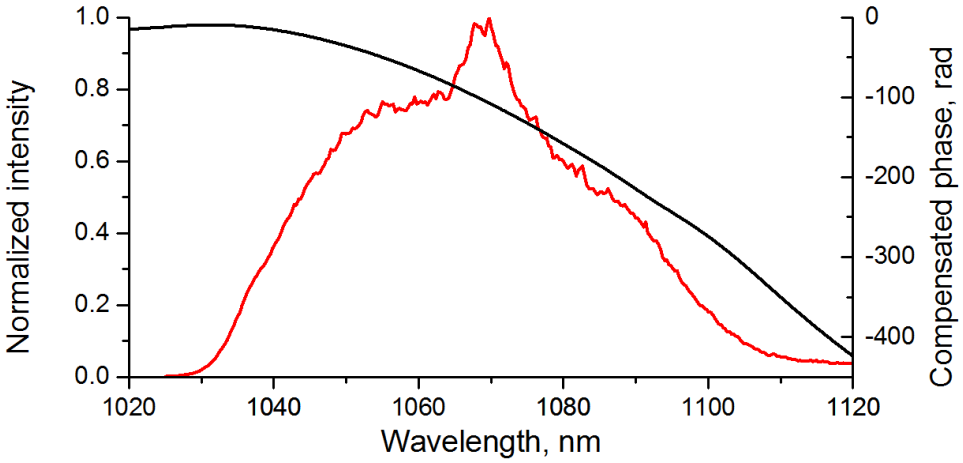

Figure 15. Laser spectrum with applied compensation mask for achieving T-L pulses at the focal spot of an objective without the adaptive optics lens.

Since any dispersive element introduces phase distortion, it is necessary to measure and compensate for the phase distortion introduced by the adaptive optics lens. Figure 16 shows the compensated phase of a laser pulse going though such a lens.

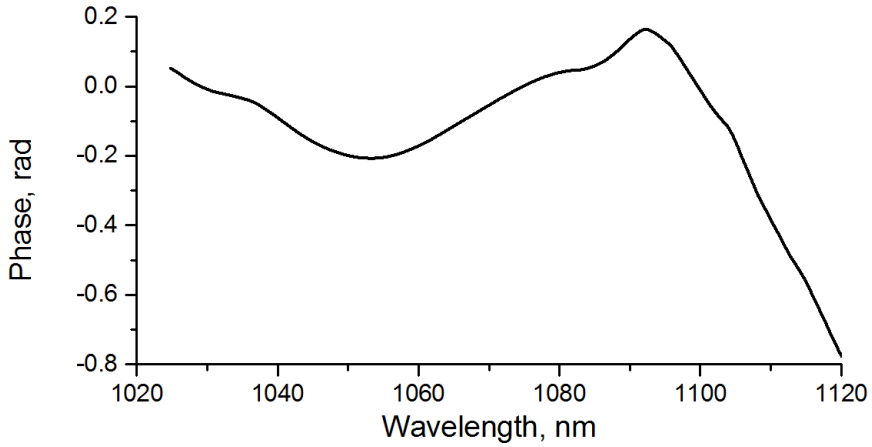

Figure 16. A measured and corrected phase distortion, introduced by AO lens.

As a first step, the laser source aberration was measured with a wave front sensor (Mercury, Adaptica srl, Italy) before the laser beam entered the microscope. As reported in Figure 17, the laser presents a small aberration of 0.10 waves rms mainly due to astigmatism and spherical aberration (see Figure 17 inset a). The adaptive optics system conducted a wavefront correction for both system aberrations and sample induced aberrations.

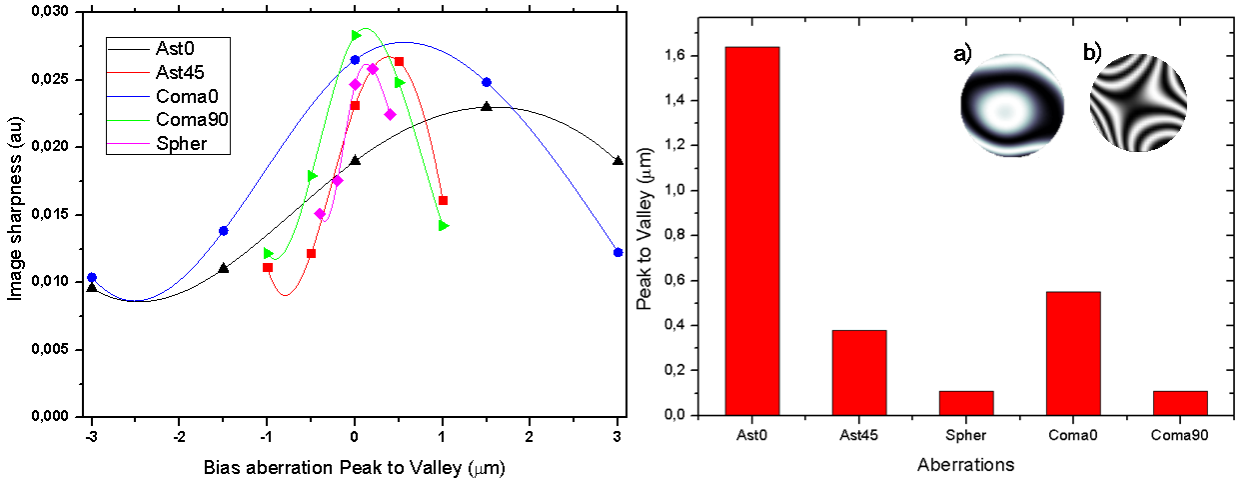

Figure 17. Left panel: Image sharpness during the optimization process. Right panel: histogram of the aberration that optimized the microscope image. Inset aberrations represented as interferograms: a) aberration of the laser source, b) aberration generated by the adaptive lens to optimize the image.

The procedure presented in [54, 55] was used as a correction algorithm. A series of images were acquired applying a bias aberration and measuring a merit function based on the integral of the intensity square of the image [21]:

$$M = \int I^2(x, y)dxdy \quad (7)$$

Astigmatism, coma, and spherical aberration were corrected by the following procedure. For each type of aberration, five values of a bias aberration were applied, the merit function values were acquired and then fitted with a 4th order polynomial curve. After each aberration scan, the maximum value in the fitted curve, which corresponds to the highest sharpness of an image, was used. As a preliminary test, TPEF microscopy images of polystyrene microspheres were taken (Figure 18).

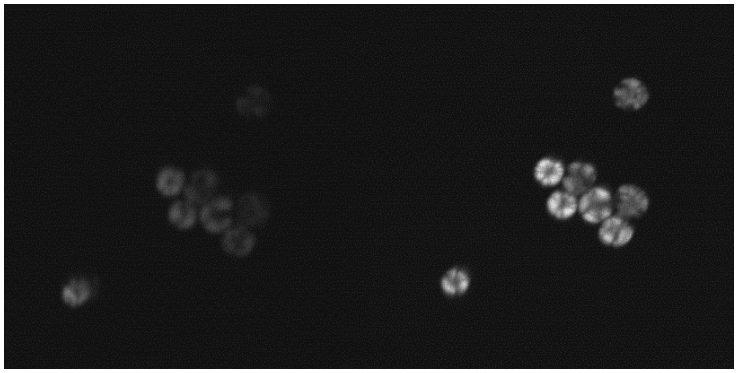

Figure 18. TPEF LSM imaging of polystyrene microspheres. Left panel – no wavefront correction; right – wavefront corrected with adaptive optics lens.

To demonstrate this method in biological samples, undissected unlabeled lab strain of *D. melanogaster* in the embryo and larva stages were imaged. This strain does not express any fluorescent proteins and the entire signal comes from endogenous fluorophores. All microphotographs were obtained from a 75 μm x75 μm area. The results of the adaptive optics optimization are shown in Figures 19-20. The average laser power at the focus point of an objective was 15 mW. Images were reconstructed by averaging tens of frames and montaged together in order to have the same brightness/contrast settings. Temporally uncompressed pulses gave no detectable nonlinear signal; therefore, images for comparison are demonstrated only for wavefront correction on and off.

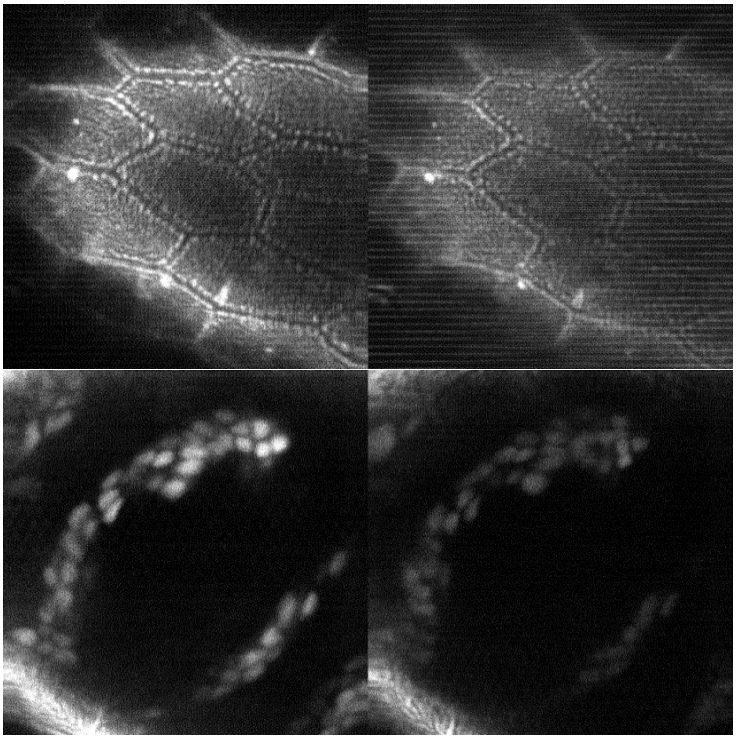

Figure 19. *In vivo* multiphoton images of undissected living lab strain *D. Melanogaster* embryo with (left column) and without (right column) AO correction. Surface of a shell (top row) and 50 μm in-depth imaging of cells (bottom row), 75 μm x 75 μm area represented.

The surface of the *D. Melanogaster* embryo is shown in Figure 19 (top row). As can be clearly seen, SN of a wavefront corrected image is much higher. An image of the same specimen from about 50 μm depth is show in a bottom row. As an example of the wavefront applied by the adaptive lens in the shell of

the embryo, we reported in Figure 17 the values obtained during the wavefront optimization process. With respect to the optimization relative to the laser source, we corrected the system aberrations and the sample induced aberrations. Figure 17 inset b shows that the wavefront, which optimized the signal of the embryo shell, was mainly astigmatic with some contribution of spherical aberration and coma.

For the in-depth imaging of a *D. Melanogaster* larva, the trachea region, which is located approximately 30 μm under the cuticula (larva skin), was chosen. Figure 20 shows the signal from the trachea walls and fat tissue around it, which is barely noticeable on the picture without adaptive lens correction.

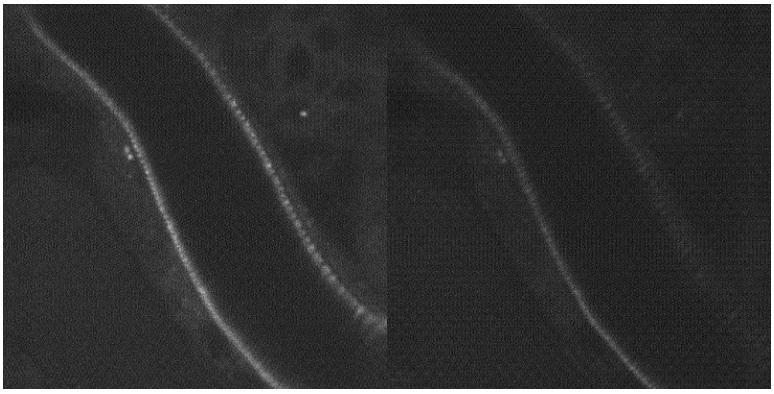

Figure 20. *In vivo* multiphoton images of a trachea region (30 μm under cuticula) of undissected living lab strain *D. Melanogaster* larva with (left column) and without (right column) AO correction. 75 μm x 75 μm area represented.

The results of this study demonstrate higher image quality of an unstained undissected *D. Melanogaster* in different stages. It was achieved with MIIPSbox640 pulse shaper and adaptive lens, which were implemented on the same two-photon microscopy system in conjunction with combined automatic correction methods, including both spatial aberrations on the sample and a spectral phase without. Adaptive pulse compression using MIIPS adaptive algorithm [19, 25] and wavefront optimization using sensor-less correction algorithm [21, 54] improved the brightness and sharpness in multiphoton imaging, as well as allowed the use of reduced average laser power in order to minimize the effects of photodamage.

2.3 Pulse shaping for selective two-photon microscopy

As it was shown in 1.2.2, the chemical specificity of each fluorophore leads to different TPA spectra. By using differently shaped laser pulses, it is possible to discriminate the chemical compounds based on their nonlinear absorption and emission properties [56].

Ultra-broadband laser sources excite the molecules in the broad range of their two-photon absorption spectrum. Most of the fluorophores are designed to work with confocal (one-photon excitation) microscopy. The absorption peak is typically in the blue range of the visible spectrum and the fluorescence is red shifted relative to the excitation wavelength with spectrum anywhere from blue to near infrared, depending on the designed spectroscopy properties of a particular fluorescent label. The two main disadvantages of single photon excitation – high background from an excitation beam and low depth resolution – are eliminated by using two-photon excitation. Producing ultra-broadband excitation increases the probability of exciting multiple fluorophores simultaneously; however, in order to create a multi-color image multichannel detection is required (Figure 21).

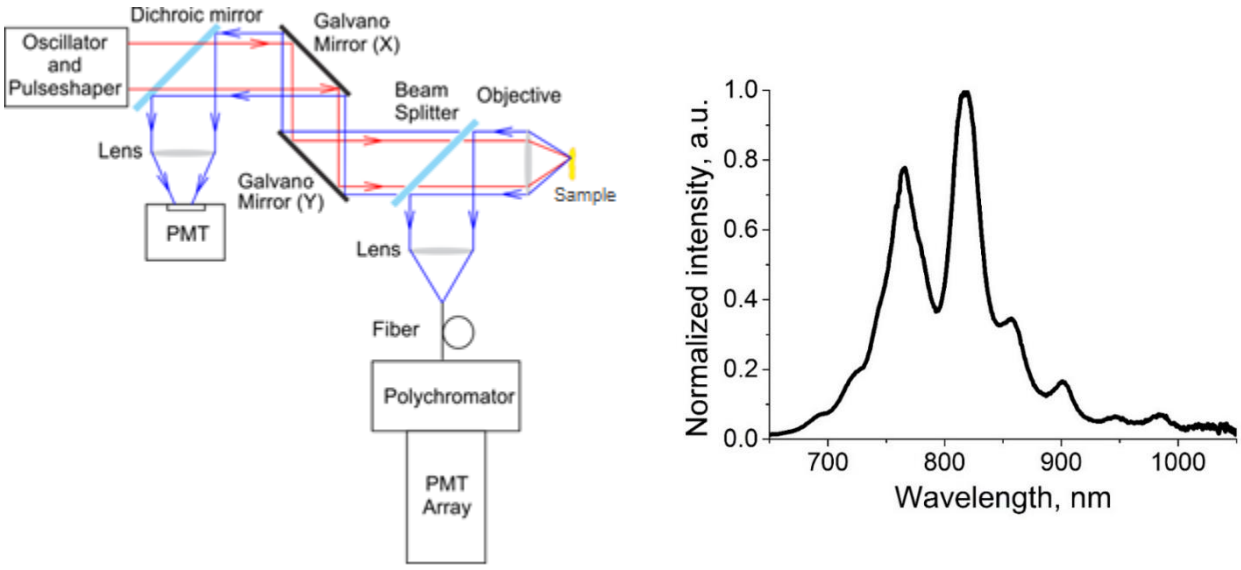

Figure 21. NOLM setup (left) and ultra-broadband laser spectrum at the focus of a microscope objective (right).

The laser beam is scanned by two galvanometer mirrors (QuantumDrive-1500, Nutfiled Technology, Inc.) and coupled into a water-immersed objective (Zeiss LD C-APOCHROMAT 40x/1.1) mounted on an adapted Nikon TE-200 inverted microscope. Laser pulses are compressed to their transform limit at the focus of the objective. With the sample placed at the focus of the objective, the generated SHG or TPEF emissions are collected in the Epi direction. The SHG/TPEF signal is separated from the fundamental light using a dichroic mirror (700DCSPXR, Chroma Technology Corp., Bellows Falls, VT) and is further filtered by a short-pass emission filter (ET680-SP-2P8, Chroma Technology Corp., Bellows Falls, VT). The SPC-830 (Becker & Hickl GmbH, Berlin, Germany) time-correlated single photon counting (TCSPC) system, capable of wavelength-resolved detection via polychromator and a PML-16-C multichannel PMT detector, was used for detection of nonlinear optical signals in different wavelength regions.

False color images in Figure 22 were obtained by combining photon counts on a multichannel PMT from regions of 380-430 nm (Blue), 460-530 nm (Green) and 540-590 nm (Red). The blue channel shows fluorescence emission from DAPI fluorophore, which is attached to cell nuclei through an antibody; the green channel depicts the distribution of Alexa488 bound to cell membrane; the red channel shows Alexa568 bound to actin filaments and resembles tubular structures and cell's cytoskeleton.

Modifying an amplitude or a phase with an adaptive shaper tailors the excitation pulses for selective excitation of particular fluorescent molecules. Phase shaping utilizes the ability of the photons within the pulse bandwidth to constructively or destructively interfere, which was observed in the change of the SHG by applying a specific phase on the pulse [56]. By utilizing the amplitude shaping, the transmission of pixels from a regions of the ultra-broadband excitation spectrum, which are not absorbed by a specific molecule, was set to zero; while the transmission of excitation spectrum, where specific molecule has maximum TPA, was set to 100%.

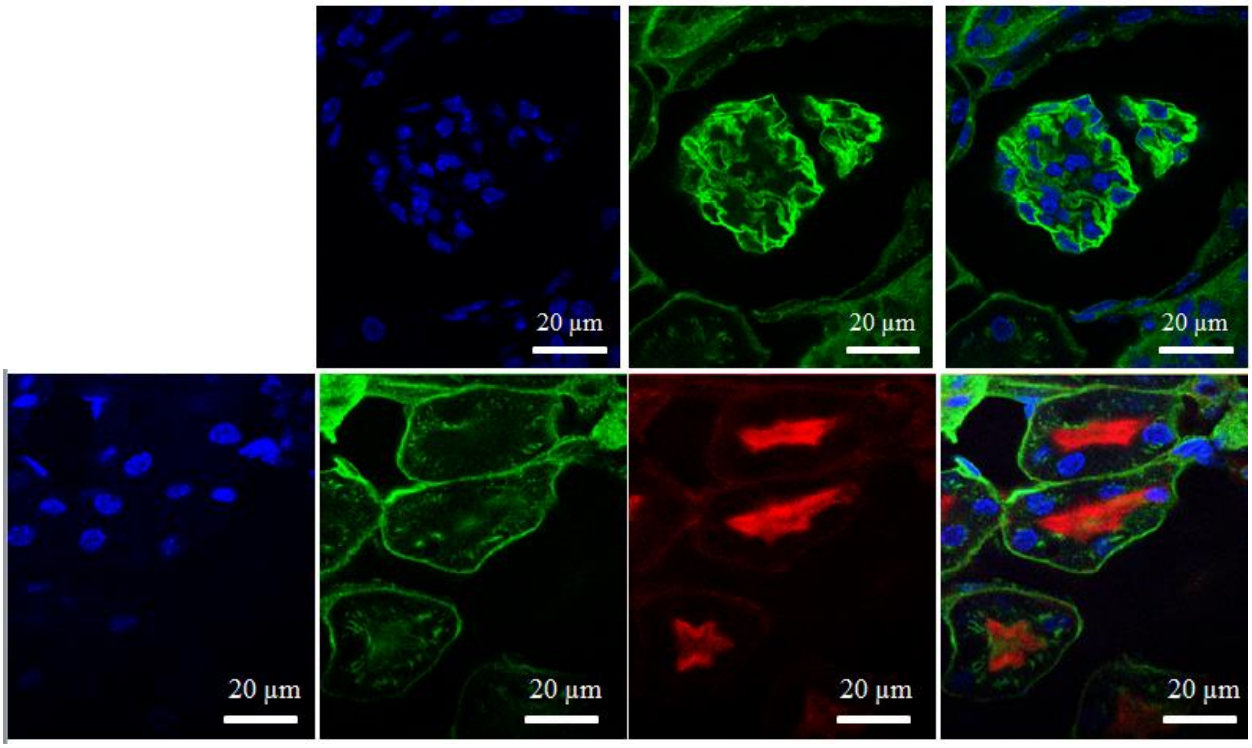

Figure 22. Stained mouse kidney section excited by a broadband laser and detected by a multichannel detector. False color represents signals from different regions of spectrum.

2.3.1 Linear unmixing of spectrally overlapping optical signals

For each fluorophore used in a stained mouse kidney section, the two-photon absorption cross-section spectra were downloaded and plotted (Figure 23 left panel) from the data pool compiled by the Developmental Resource for Biophysical Imaging Opto-Electronics (DRBIO) of Cornell University. For each fluorophore, the TPA contrast was calculated as:

$$Contrast(\lambda, i) = TPA(\lambda, i)/(TPA(\lambda, j)+ TPA(\lambda, k)) \quad (8)$$

where $TPA(\lambda, j)$ and $TPA(\lambda, k)$ are values of TPA for the rest of the two fluorophores.

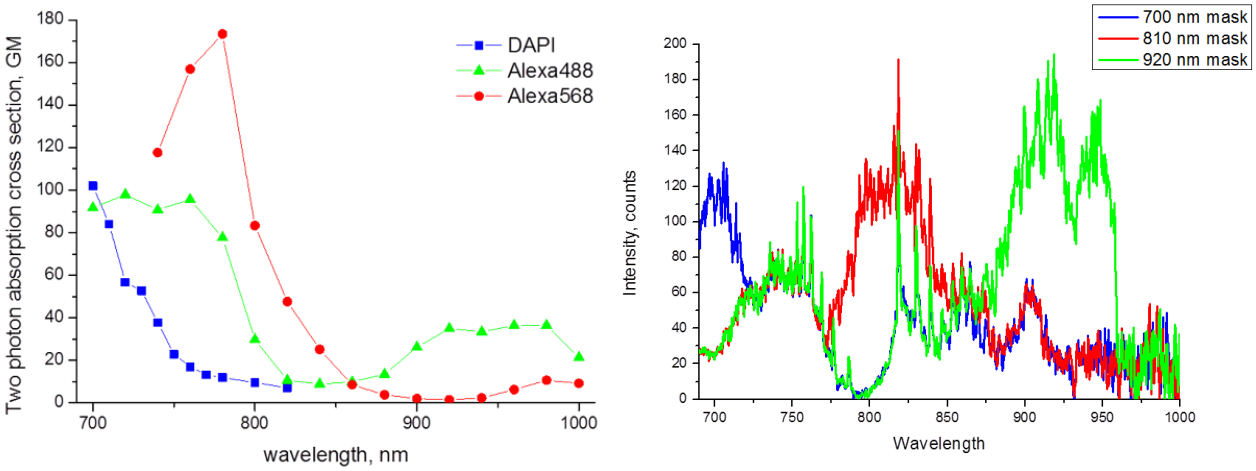

Figure 23. Left: Absorption spectra of fluorophores, used in labeling and staining of mouse kidney section. Right: Spectra of excitation pulses with three different amplitude masks applied.

The wavelength regions where TPA of the particular fluorophore of interest is maximum were found by analyzing the spectra of contrast for each fluorophore allowed finding the wavelength regions. By applying this approach to other fluorophores, three amplitude masks were constructed so that each mask would create pulses with spectra, which highlights the specific molecules that absorb most efficiently. The right panel of Figure 23 shows the excitation spectrum of laser (Figure 21) with applied masks, designed to maximize the excitation of DAPI, Alexa488, and Alexa568 fluorophores.

The imaging procedure is similar to the one described in 2.3, except that all of the TPEF signals were detected on a single PMT (HC20-05MOD) in the epi direction. For the each applied amplitude mask, tens of frames were averaged in order to increase the signal-to-noise ratio.

The resulting images of mouse kidney sections are shown in Figure 24. The top row summarizes images obtained with the amplitude masks applied. Each image still contains the contribution of signals from other fluorophores, other than the one that is primarily targeted by applying the specific amplitude mask. By applying the linear unmixing algorithm, which analyzed the intensity contribution of each fluorophore for each pixel, the images in the bottom row were generated.

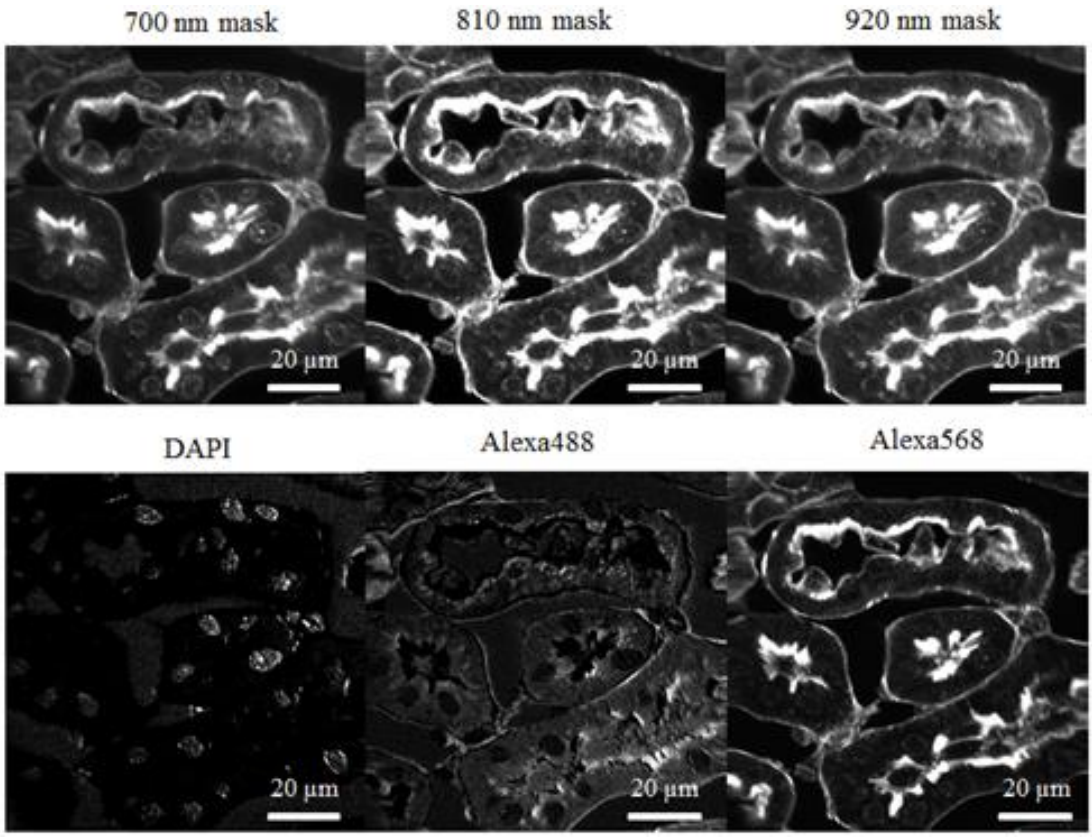

Figure 24. Comparison of reconstructed (top row) and unmixed (bottom row) TPEF microscopy images of a stained mouse kidney section.

Linearly unmixed TPEF images of stained mouse kidney section were false colored and overlaid into one image (Figure 25). Compared to Figure 22, the same nuclei, cell membranes, and actin filaments can be identified, however only a single PMT detector was used.

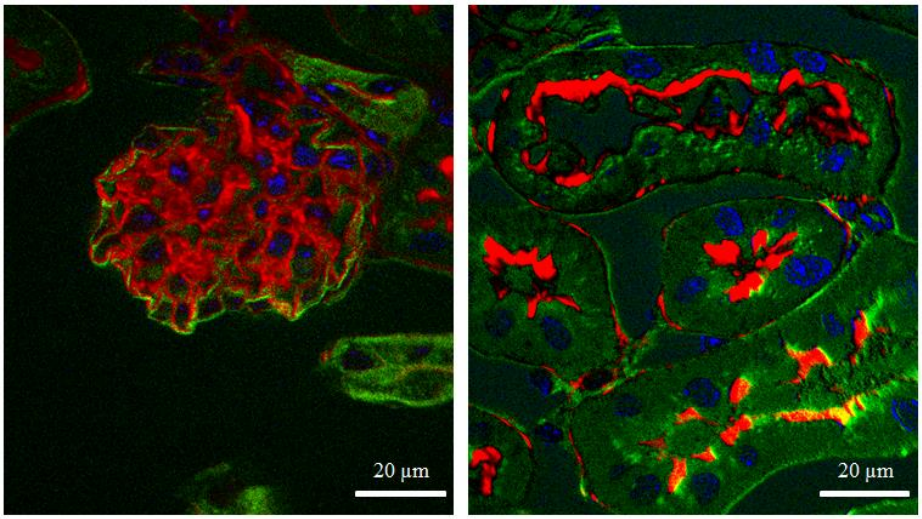

Figure 25. False colored images of a mouse kidney sections. Left: kidney glomeruli; Right: kidney cells.

2.3.2 Quadrature detection of multiplexed optical signal

The broad bandwidth and high peak intensity of femtosecond lasers enable the two-photon excitation of many different fluorophores with high efficiency using a single laser setup. Selective excitation of particular fluorophores can be achieved by a computer controlled pulse shaper, taking advantage of multiphoton intrapulse interference (MII) [26, 47, 56]. Phase shaping, in particular, can maintain the high efficiency, but excite a particular frequency within the two-photon bandwidth with high spectral resolution. Unfortunately, pulse shapers appropriate for microscopy have slow refresh rates, which limits the speed with which multiple fluorophores may be measured with a single detector. Here we achieve 162 MHz rate pulse shaping on a near octave-spanning laser using passive components. With a single photomultiplier tube (PMT) detector, we are able to selectively image two fluorophores with excitation separated by 50 nm.

An ultra-broad bandwidth oscillator and pulse shaper (femtoAdaptiv, BioPhotonic Solutions Inc.) with a central wavelength at 812 nm (Figure 21) and 81 MHz pulse repetition rate is capable of exciting two-photon transitions in the 380 to 500 nm range. Figure 26 shows a typical SHG of a T-L pulse from femtoAdaptiv laser at the focus of a 40x/1.1NA water immersion objective (dash line). The FWHM of SHG spectrum is about 35 nm. Selective excitation [56, 57] in the blue and red portions of the spectrum is achieved by a combination of second order dispersion (SOD) and third order dispersion (TOD) [47].

As shown in Figure 27, the output from the laser was split into two arms with different second order dispersion (SOD). The recombined beams create a train of pulses with spectral phase switching at a 162 MHz rate. Each pulse induces selective TPEF on the sample at wavelengths determined by the amount of SOD and TOD in the beam [58].

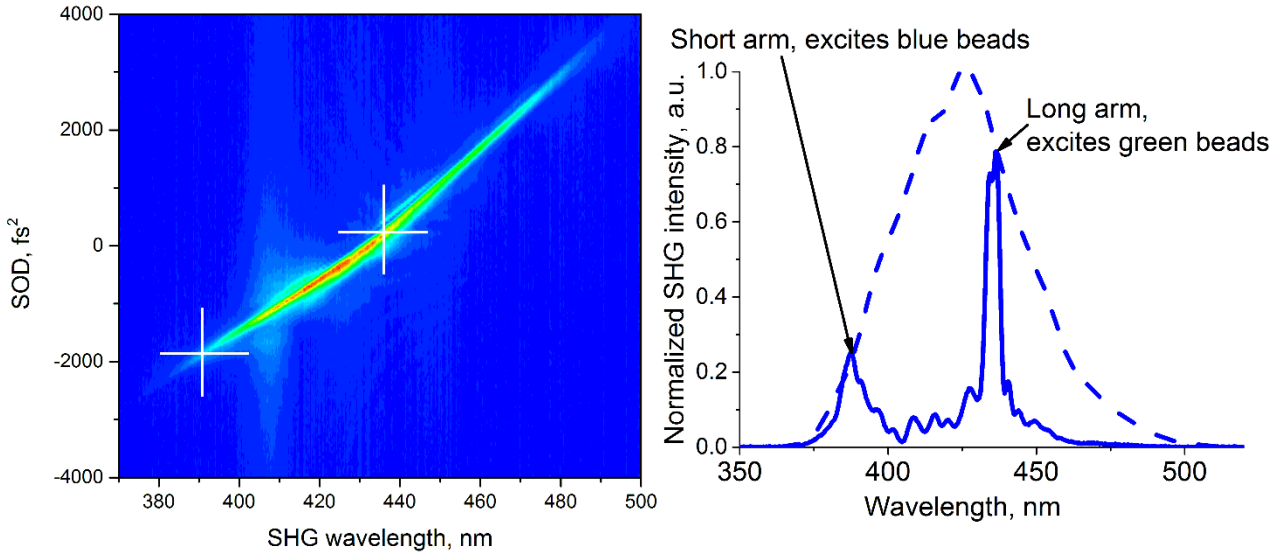

Figure 26. Left panel: MIIPS scan of the laser pulse without compensation mask applied. Right panel: SHG spectrum of laser pulse with applied phase compensation (dashed), pre-chirped and delayed in different arms (solid). All measurements made at the focal plane of a Zeiss LD C-APOCHROMAT 40×/1.1 objective.

Excitation laser pulses with different shapes (typical energy ~110 pJ per pulse at the focus of the objective) are temporally delayed by ~ 3 ns due to the difference in optical path length through two arms of a delay line (Figure 27). The temporal delay between recombined differently shaped pulses is adjusted by the position of M1 mirror to match a quarter (*T/4*) of pulse repetition period out of the oscillator.

Each pulse induced selective TPEF on the sample at wavelengths determined by the amount of SOD in the beam. Fluorescence was detected by a single fast photomultiplier tube (PMT) detector; therefore, the signal from the PMT detector contained fluorescence signals from two different selectively-excited fluorophores separated by ~ 3 ns. The two separate signals are isolated by quadrature detection using a lock-in amplifier as shown in Figure 28. Images are obtained from two different fluorophores simultaneously. This allows for fast frame-rate imaging.

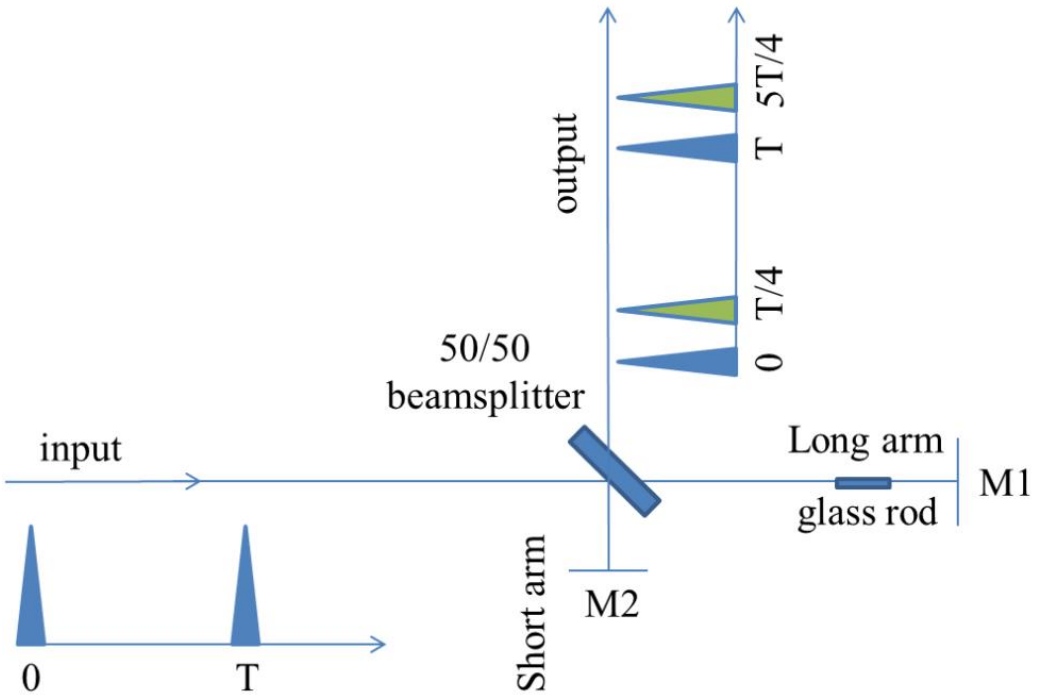

Figure 27. Schematic representation of excitation beam quarter-period delay line with different amount of SOD in arms.

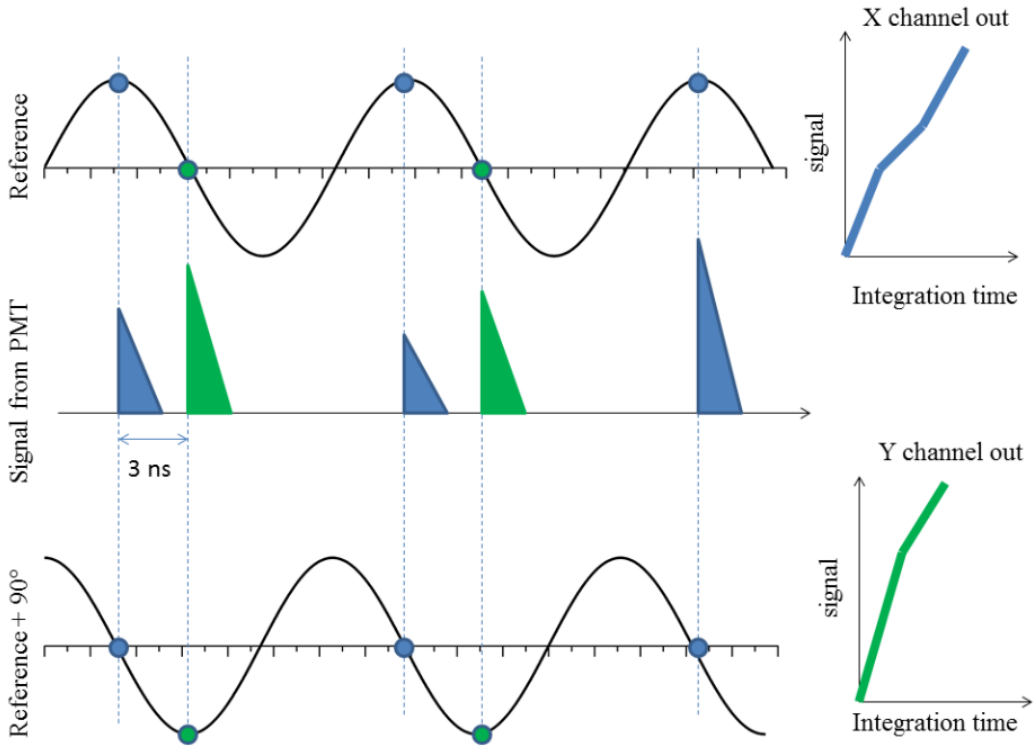

Figure 28. Simultaneous acquisition of signals from two different fluorophores at a single photo-detector by quadrature detection using lock-in amplifier.

The microscopy image (shown in Figure 29) provides a selective signal from 10 μm blue microspheres when detecting signal from the X channel of the lock-in amplifier. The image from the 6 μm beads is obtained when detecting signal from the Y channel of the lock-in amplifier (with 90 degree phase difference). The combination of both signals provides the full image.

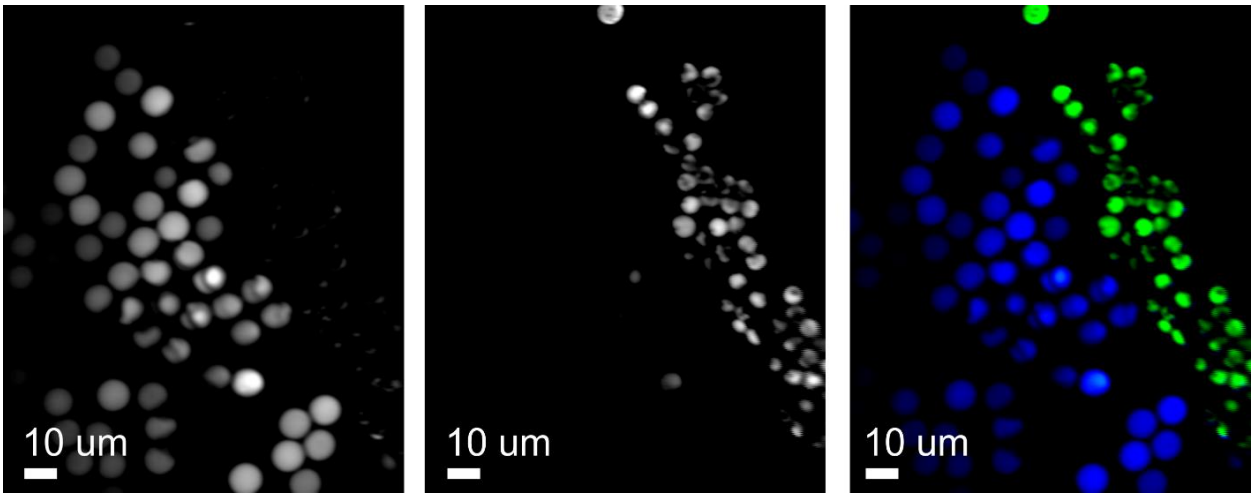

Figure 29. Microscopy images of fluorescent beads, using the signal from X channel (left image) and Y channel (center image) of the lock-in amplifier. False colored image obtained by adding the X and Y channel signals (right image).

Wide tunability of the two-photon excitation wavelength, fast switching rate between the selective excitation, and low photodamage (due to the higher peak intensity of shorter pulses [59]) enables application of this method for *in vivo* dynamic imaging in biological samples.

Chapter 3 Depth-resolved NLOM using ultrafast Yb-fiber oscillators

The conventional source for multiphoton microscopy is a mode-locked Ti:Sapphire laser oscillator with pulses centered around an 800 nm wavelength. This type of laser became an industry standard for use in multiphoton microscopy, because of the capability of producing routine pulses with tens nanojoules of energy and less than 100 fs duration. In our laboratory, a Ti:Sapphire oscillator from KM Labs with a bandwidth up to 100 nm FWHM is routinely used for NLOM with compressed pulses of 12 fs FWHM duration at the focal point of a high NA objective.

Due to benefits such as high contrast ratio, submicron resolution, and depth resolved imaging, multiphoton microscopy has gained broad acceptance in recent years [4, 8, 18]. Modalities such as TPEF [60], SHG, THG [11, 61] provide complementary information from stained, as well as unstained samples. SHG and THG microscopy depend on molecular properties and require no fluorescent labeling, thereby reducing the complexity of biological imaging. Unlike TPEF, the signal increases as the inverse of pulse duration (for SHG) and the inverse of the pulse duration squared (for THG), without the limit imposed by the two-photon absorption spectrum; making SHG and THG amenable to ultrashort pulse excitation.

A number of different ultrafast solid state laser sources, such as Ti:Sapphire at 800 nm [62], Cr:Forsterite at 1230 nm [63], and Optical Parametric Oscillator (OPO) at 1500 nm [11], have been used for multiphoton microscopy. In the past decade, fiber lasers have drawn increasing attention due to their compact size and greater stability [64, 65]. Er-doped fiber at 1550 nm [66] and Yb-fiber at 1060 nm [67] lasers have been used for multiphoton microscopy; however, these lasers have pulse durations greater than 100 fs, longer than those of Ti:Sapphire lasers, requiring higher energy of excitation pulses in order to have comparable nonlinear signal intensity.

Figure 30 demonstrates a several examples of multimodal NLOM imaging using newly developed femtosecond light sources working in a different regions of electromagnetic spectrum (Figure 31): an ultrabroadband Ti:Sapphire oscillator in VIS-NIR; an ultrafast Yb-fiber oscillator in NIR, which was developed by Dr. Bai Nie [68] while being a graduate student at Dantus Research Group; and a supercontinuum light source capable of producing 100 fs IR pulses.

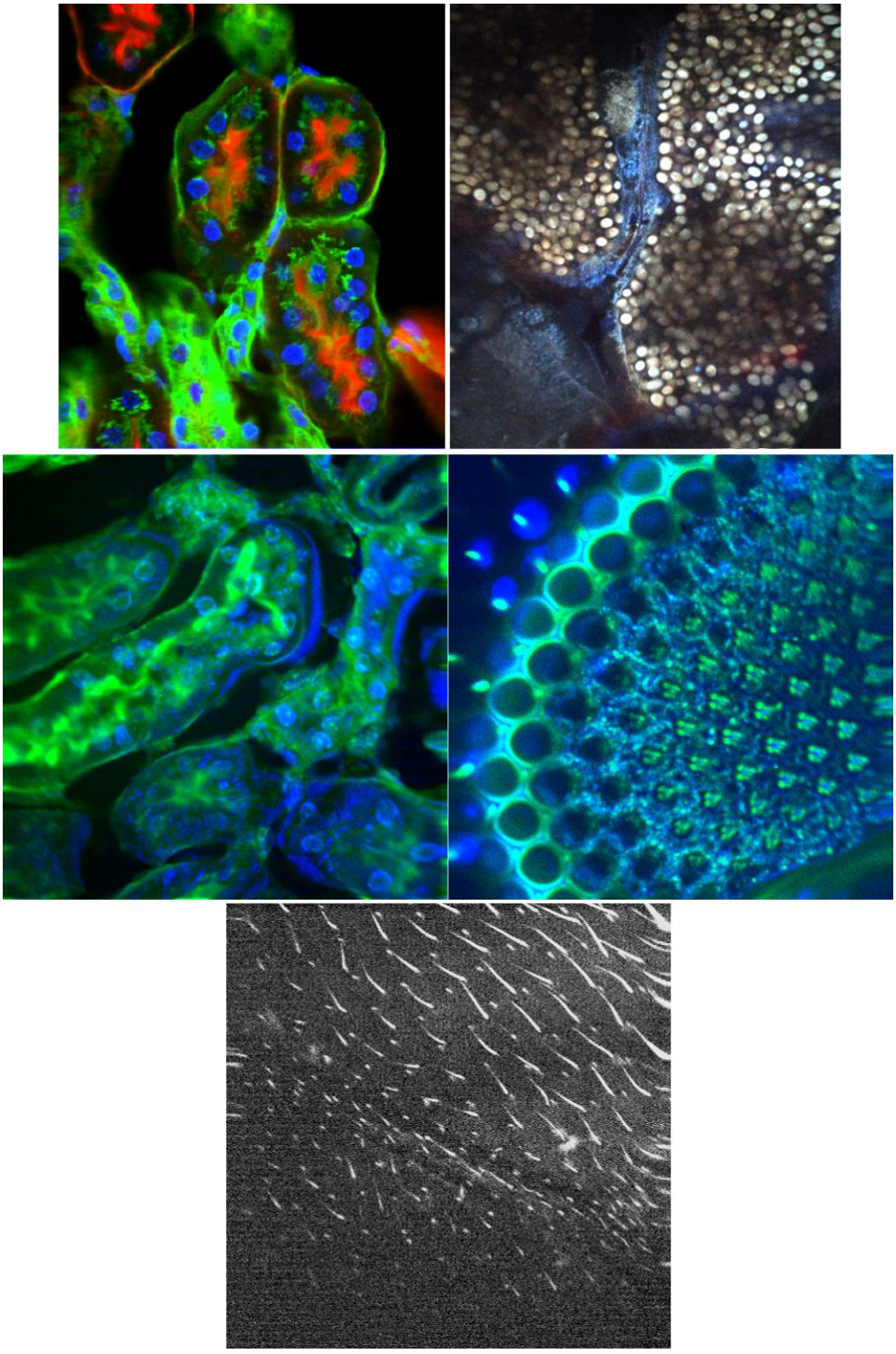

Figure 30. Multiphoton images (SHG, TPEF, and THG) obtained using different femtosecond pulse sources. Top row images obtained using Coherent Vitara, left – stained mouse kidney section; right – undissected unstained *D. Melanogaster* larva. Middle row images obtained using Yb-fiber laser, left – stained mouse kidney section; right – undissected unstained eye of an adult *D. Melanogaster* fly. False colors applied according to the wavelengths of the detected optical signal. Bottom image is a THG image of a fly wing, obtained using IMRA Femtolite 1620 nm centered supercontinuum source.

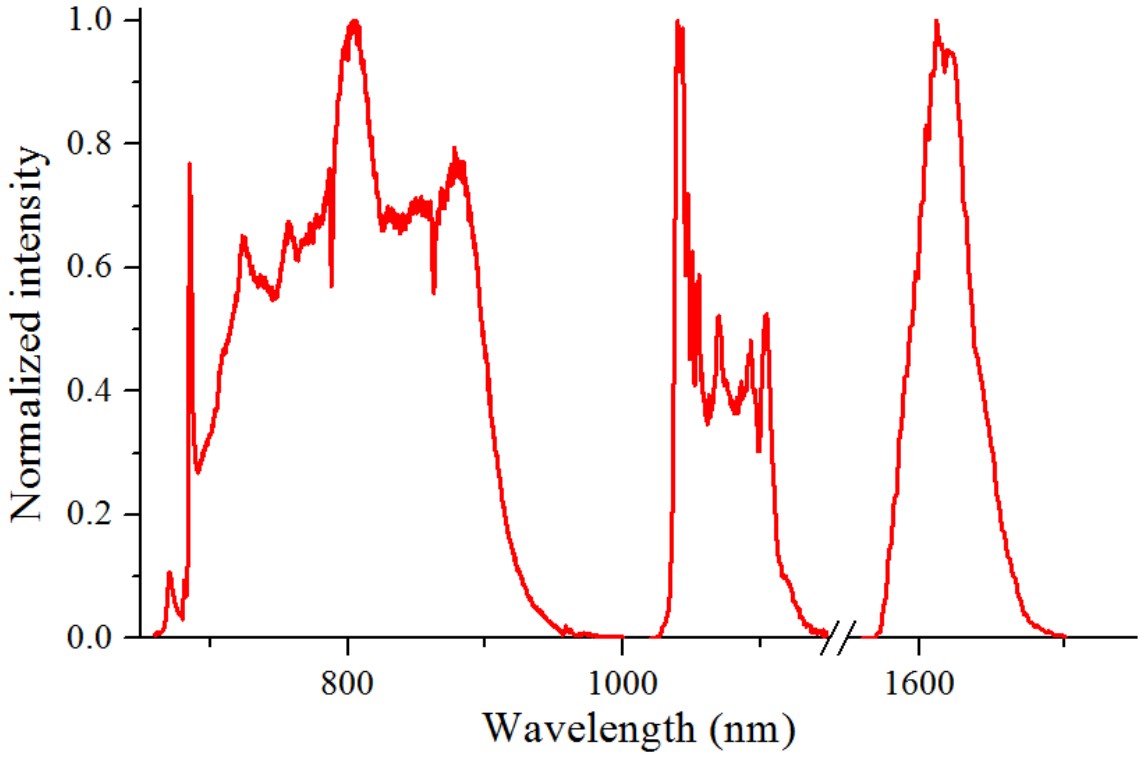

Figure 31. Emission spectra of Ti:Sapphire lasers (650 – 1050 nm), Yb-doped fiber lasers (1000 – 1200 nm) and supercontinuum generation – based light source (1550 – 1700 nm).

In recent years, laser vendors have developed new ultrabroadband Ti:Sapphire lasers, such as Venteon femtoAdaptiv and Coherent Vitara. These lasers are capable of producing pulses with more than 200 nm FWHM and 500 nm bottom to bottom spectrum from 600 nm to 1100 nm (Figure 31). Wide bandwidth enables these lasers to excite multiple fluorophores simultaneously in stained and unstained imaging of biological tissues (Figure 30, top row). Labeling fluorophores, such as DAPI, Alexa488 and Alexa568, provide a strong TPEF signal in a thin mouse kidney section revealing position of nuclei (blue color) within cells, cell membranes (green color) and actin distribution (red). On the other hand, the use of such ultrashort pulses provides nonlinear signals in the unstained undissected *D. melanogaster* larva such as TPEF (yellow) from endogenous fluorophores (NADH, LipDH, FAD [69]) and SHG from fibrous protein structures.

Another class of coherent light sources, which can be used for NLOM are supercontinuum generation light sources. Figure 31 shows a spectrum of a commercial sub-100 fs source with a central

wavelength around 1620 nm Femtolite (IMRA America Inc., Ann Arbor, MI). The THG imaging was demonstrated (Figure 31, bottom row) using this source on a fruit fly wing. Sharp structures such as hair and wing surface provide strong THG due to a difference in the index of refraction with air.

With the rapid development of fiber laser technology, Yb-doped fiber lasers with less than 50 fs pulse duration and tens of nanojoules pulse energy become a viable option for NOLM. Unlike images, obtained with ultrabroadband Ti:Sapphire oscillators, TPEF and 3PEF signals from DAPI, Alexa488 and Alexa568 were not detected due to low two- and three-photon absorption at 1060 nm. SHG (green) and complimentary THG (blue) modalities revealed the structure of thin mouse kidney section and a fruit fly eye (Figure 31, middle row). Compact design, robustness, temperature/humidity tolerance, and most importantly, sub-50 fs pulse duration, make these lasers a very good candidates for future implementation for commercial and medical use.

This chapter will demonstrate the applications of ultrafast Yb-fiber lasers based on self-similar evolution [65] with different configurations for depth-resolved NLOM of undissected *D. melanogaster in vivo* and normal human skin tissue *in vitro*.

3.1 THG and SHG imaging of *D. Melanogaster* larvae using sub-50 fs Yb-fiber laser

Due to the benefits of high contrast ratio, sub-micrometer resolution, and depth resolved imaging, multiphoton microscopy has proved to be a powerful tool for studying living tissues [4, 18]. The harmonic generation modalities, such as SHG and THG, do not require sample staining and labeling procedures, which makes them preferable for non-invasive *in vivo* microscopy imaging of biological tissues. In addition, SHG and THG provide complementary information due to their different optical-response mechanism. It is found that SHG or THG efficiency is inversely proportional to the pulse duration or pulse duration square, respectively [19, 59, 70], therefore, ultrashort laser pulses are preferred to achieve good multiphoton efficiency for both SHG and THG imaging. For clinical use, a compact and environmentally stable laser is necessary. In the past decade, fiber lasers have emerged as ideal ultrafast light sources [71]. In this study we tested an Yb-fiber oscillator [68], capable of delivering pulses as short as 50 fs at 1060 nm central

wavelength, for multiphoton microscopy imaging. The capability of this laser for multiphoton microscopy is evaluated with different samples, including prepared microscopy slides with stained mouse kidney and intestine sections and unstained living whole *Drosophila Melanogaster* larva. Images generated by different modalities such as TPEF, SHG, and THG are compared.

An Yb-fiber oscillator is operated at 43 MHz with an average power up to 400 mW. This laser is based on an all-normal dispersion cavity and is similar to the design of the laser described in ref. [68]. The output laser beam is guided through a 4-f folded pulse shaper (MIIPS Box 640, BioPhotonic Solutions), which is used to compensate the high-order (second order and higher) phase distortions to deliver T-L pulses at the focal plane of a microscope objective. Output from the pulse shaper is directed to a laser-scanning multiphoton microscope. The laser beam is scanned by galvanometer mirrors (QuantumDrive-1500, Nutfield Technology, Inc.) and coupled into a water-immersed objective (Zeiss LD C-APOCHROMAT 40x/1.1). The generated SHG and TPEF emissions from samples are collected in the Epi direction, filtered out using a dichroic mirror (700DCSPXR, Chroma Technology Corp.) and a short-pass emission filter (ET680-SP-2P8, Chroma Technology Corp.). A photomultiplier (PMT, HC20-05MOD, Hamamatsu) is used to collect the SHG/TPEF signal. THG, which is primarily generated in the forward direction, is collected by a UV compatible objective (HP ReflX, NT59-886, NA 0.28, Edmund Optics). The THG signal is also separated from the excitation light by a 410 nm short pass filter and detected by a PMT (H10720-210, Hamamatsu) whose signal is amplified (SRS445, Stanford Research Systems). The focal plane is moved to different layers using a step motor capable of making precisely controlled 2 μm height steps. All the SHG or THG images are then incorporated into a 3D image.

Excitation laser pulses were compressed to about 50 fs at the focal plane of the objective using MIIPS algorithm. After pulse compression, samples were loaded onto the focal plane of the objective. To calibrate the microscope, two stained commercial samples (mouse kidney and mouse intestine, Molecular Probes) that have uniform thickness of about 10 μm are imaged.

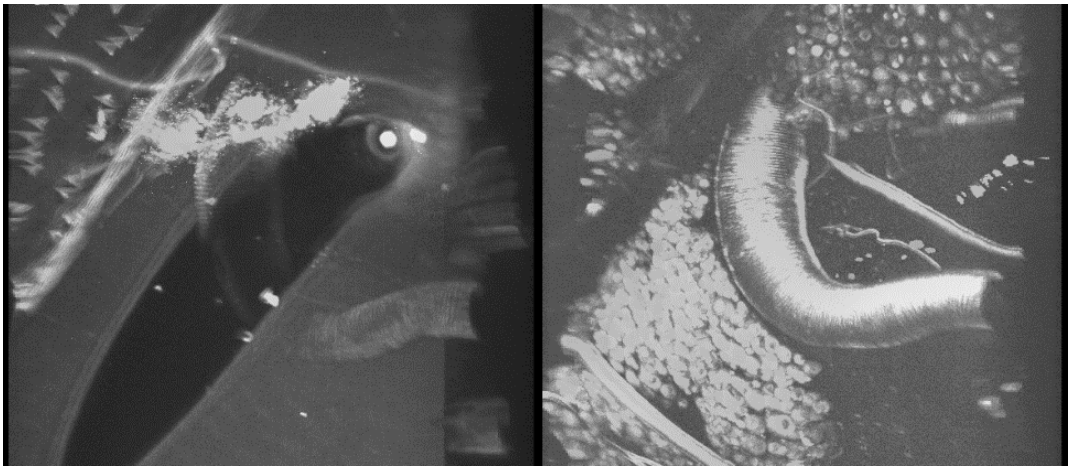

Figure 32. Projection of 3D images at 30° angle for SHG (left) and THG (right) microscopy of the third instar D. Melanogaster larva. Images are of the same 150 μm x 150 μm region centered at the trachea, but different contrast mechanisms highlight different organs.

Beyond imaging labeled and stained samples, depth-resolved imaging of unstained live tissue is of greater importance. Depth resolved images of third instar *Drosophila* larva with a total scanned depth of 90 μm are shown in Figure 32. She signal detected in the Epi direction is mainly from two- or three-photon excited fluorescence. On the forward direction, primarily a THG/three-photon excited fluorescence signal is detected. The THG 3D image shows many more structures; for example, the THG image provides a strong signal from the location of lipid cells, blood vessels, and the trachea, while most of the SHG signal comes from the skin layer, rich with chitin, and the trachea's fibrous tissue.

3.2 THG and SHG imaging of human skin

In vivo, label-free NLOM of human skin is under investigation for a broad range of clinical applications spanning from skin cancer detection and diagnosis [20, 72, 73] to characterizing and understanding keratinocyte metabolism [74], skin aging, [75, 76], pigment biology [74], and cosmetic treatments [77]. NLOM signals are derived from several sources including cellular co-factors, melanin, and extracellular matrix (ECM) proteins. Although exceptionally rich in both anatomic and functional contrast, NLOM has a relatively limited penetration depth in turbid materials. This is due to the fact that focused laser beam experiences multiple light scattering, which diminishes the instantaneous excitation intensity and non-linear signal generation. As a result, there is considerable interest in exploring how light source performance can

be optimized to improve imaging depth. Ti:Sapphire lasers, commonly used in NLOM imaging, are generally able to access the superficial dermis of human skin to depths of 150 – 200 μm. The penetration depth primarily depends on the material scattering length at the excitation wavelength, the efficiency of the non-linear excitation process, the excitation average power, repetition rate, pulse width, and the detection geometry. Adjusting these parameters in order to improve the penetration depth has been explored in several studies using Ti:Sapphire and OPO-based femtosecond lasers as excitation light sources [78-82]. *Sun et al.* have shown that reduced light scattering using a Cr:Forsterite 1230-1250 nm source can increase penetration depth up to 300 μm for harmonic generation imaging of human skin [83]. Improvements in the penetration depth can also be achieved when using shorter laser pulse widths [80]. Depth resolved imaging studies require higher average laser powers, however this can cause thermal damage to tissue, which is an issue of concern [70, 84]. Photothermal absorption of tissue is wavelength dependent, and so is the damage threshold. Heating following laser exposure at 800 nm is five times greater than at 1060 nm, and the damage threshold at 800 nm is three times lower than at 1060 nm [85]. With the development of next generation fiber lasers, it is possible to imagine combining these technical features with more compact, portable, and inexpensive light sources that could facilitate clinical translation of NLOM technology.

Fiber-based laser sources have been used for NLOM imaging of thin tissue cross-sections [70, 82, 86], mouse brain [7], and human skin tissue [87] using fluorescence labeling. In this work, we evaluate the performance of a sub-40 fs 1060 nm Yb-fiber laser for label-free NLOM imaging of human skin. The effect of excitation wavelength and pulse width on penetration depth in thick, turbid tissues is determined by comparing the fiber laser to an 800 nm Ti:Sapphire laser source. We employ the depth-dependent decay of second-harmonic generation (SHG) signals as a standard metric for evaluating performance.

The excitation laser sources used were a Ti:Sapphire oscillator (MIRA 900; Coherent Inc; 220 fs, 76 MHz, 600 mW output power, tuning wavelength 720-980 nm) tuned to 800 nm for this study; and an Yb-fiber laser (BioPhotonic Solutions Inc., USA; 1060 nm, sub-40 fs, 39.2 MHz, 200 mW temporally compressed output power). The prototype Yb-fiber laser, with self-similar pulse evolution [70], has an integrated adaptive phase-amplitude pulse shaper MIIPS-HD (BioPhotonic Solutions Inc., USA) based on

a 4-f configuration with a two dimensional spatial light modulator. The purpose of the pulse shaper was to control high-order phase distortions introduced by the high-NA objective and other dispersive elements in the beam path. The 1060 nm pulses were compressed to nearly-T-L duration using MIIPS, [47] and their FWHM duration was measured by interferometric autocorrelation using the microscope detection unit (BioPhotonic Solutions Inc., USA) at the focal plane. Each of the two excitation beams (800 nm and 1060 nm) was directed towards our home-built laser-scanning microscope and focused into the sample by an Olympus objective (XLPL25XWMP, 25X/1.05NA water). The nonlinear signals from the sample were epi-collected and directed towards two photomultiplier tubes (R3896, Hamamatsu) by a dichroic mirror (Semrock, Inc 510 LP). The dichroic mirror was used to split the emission signal into two spectral channels defined by the emission filters: 440 SP; 375/110 BP and 720 SP; 535/150 BP (Semrock Inc).

We used discarded human skin tissue (fixed in formalin) to test the effect of sub-40 fs, 1060 nm excitation laser pulses on depth penetration in this sample. For each excitation wavelength (800 nm and 1060 nm) we acquired five stacks of images as optical sections of about 430 x 430 μm^2 (512x512 pixels) at different depths ranging from 0 to 200 μm (2 μm step). In the sample studied in this work, the main contrast mechanisms for 800 nm excitation are based on TPEF signals from keratin, melanin, and elastin fibers, and SHG signals from collagen fibers. When using 1060 nm as excitation, the epidermis is visualized by the THG contrast derived from refractive index discontinuities at interfaces, while dermal contrast is derived from the collagen fiber SHG.

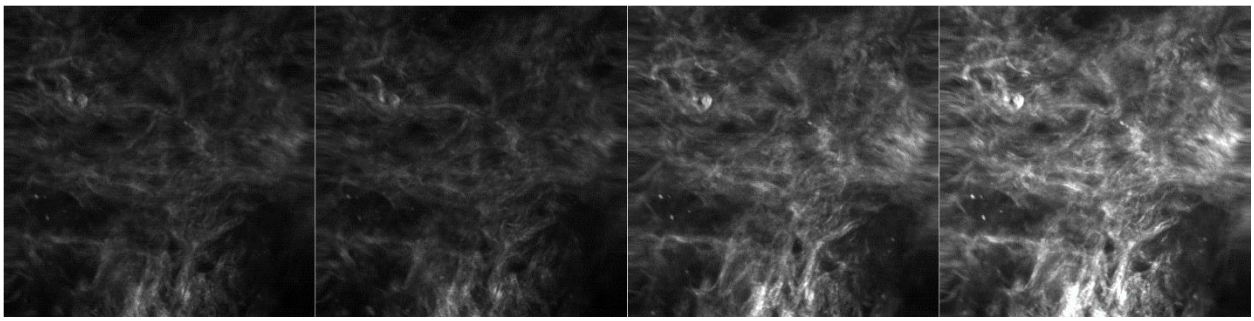

Figure 33. 150 μm x 150 μm SHG images of the same region of human skin at 90 μm depth, acquired with 1060 nm excitation wavelengths. (a,b) Positive and negative 7×10^6 fs^4 fourth order dispersion applied to T-L pulses; (c) 43450 fs^2 SOD pre-chirped pulses; (d) fully compressed T-L laser pulses were used. Brightness settings were kept the same for all four images for comparison.

With the variety of laser sources available for the NOLM, laser manufacturers offer built-in pulse compression. However, the remaining uncompressed higher order dispersion in the laser pulses can degrade the SHG signal. Figures 33 a,b were obtained under conditions that emulate having a pedestal in the time domain; Figure 33c was obtained emulating the use of a prism or grating compressor. Figure 33d shows the microphotograph, obtained with fully compressed T-L pulses. Figures 33d and 33c demonstrate 2.5 and 2 times greater intensity than either Figures 33 a or b. This is a clear indication of the benefit of an adaptive pulse shaper for multiphoton imaging when sub-40 fs pulses are being used.

Figure 34 shows merged images of human skin acquired at the same depth with 800 nm and 1060 nm excitation. THG imaging of keratinocyte structure in human skin epidermis using 1230 nm as excitation has been reported by CK Sun *et al.* in several studies [75, 83]. THG is not generated by elastin fibers in human dermis, although signals from elastic cartilage have been observed [88].

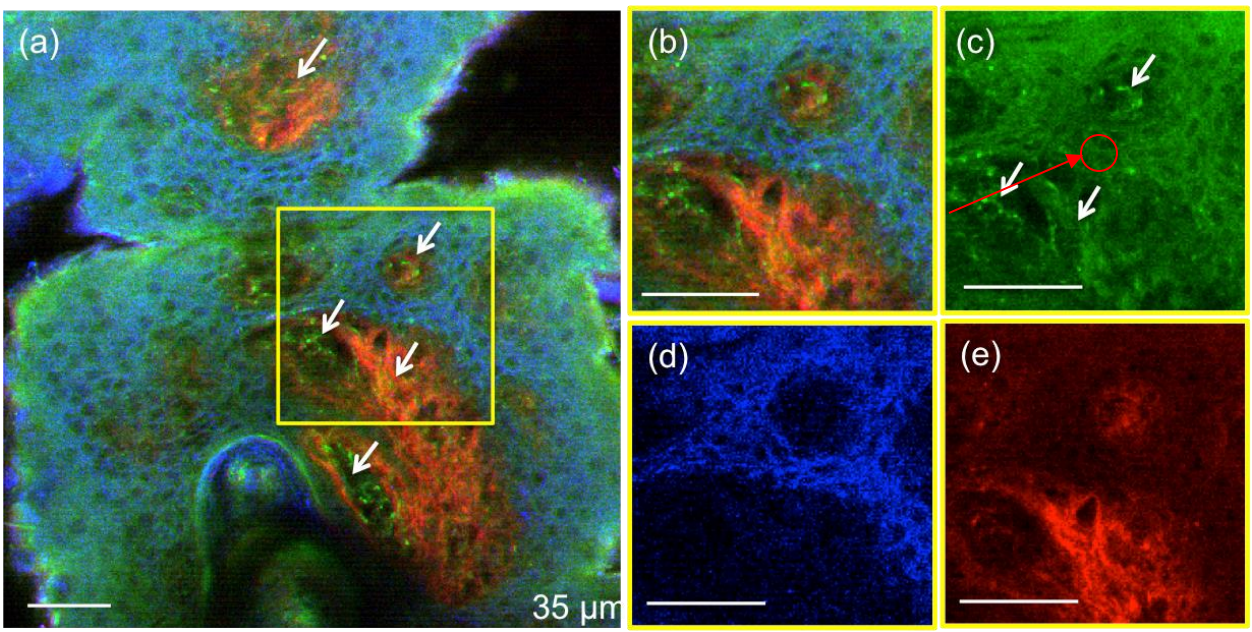

Figure 34. Multimodal NLOM images of human skin acquired with 800 nm and 1060 nm excitation wavelengths at the same depth. (a) Epidermal-dermal junction in human skin imaged by THG (blue) and SHG (red) using. 1060 nm and by TPEF (green) using 800 nm as excitation wavelengths (z=35 µm). TPEF signal originates from keratin in the epidermal keratinocytes and from elastin fibers (arrows) in the superficial papillary dermis, while THG signal highlights the keratinocytes only; SHG signal originates from collagen fibers. (b) Multimodal NLOM image corresponding to the inset in (a) representing contribution from three channels: (c) TPEF signal from keratinocytes and elastin fibers (arrows) (d) THG signal from keratinocytes and (e) SHG signal from collagen fibers. Scale bar is 50 µm.

Figure 35 shows representative images corresponding to one of the stacks acquired in the same location of the sample by using 800 nm and 1060 nm as excitation. The images in Figure 35 (a-c, f-h) represent en-face (x-y plane) images acquired at different depths. The cross-sectional (x-z plane) images shown in Figure 35 (d, e) were obtained from 3D image reconstruction of en-face stacks using Amira (FEI Inc.).

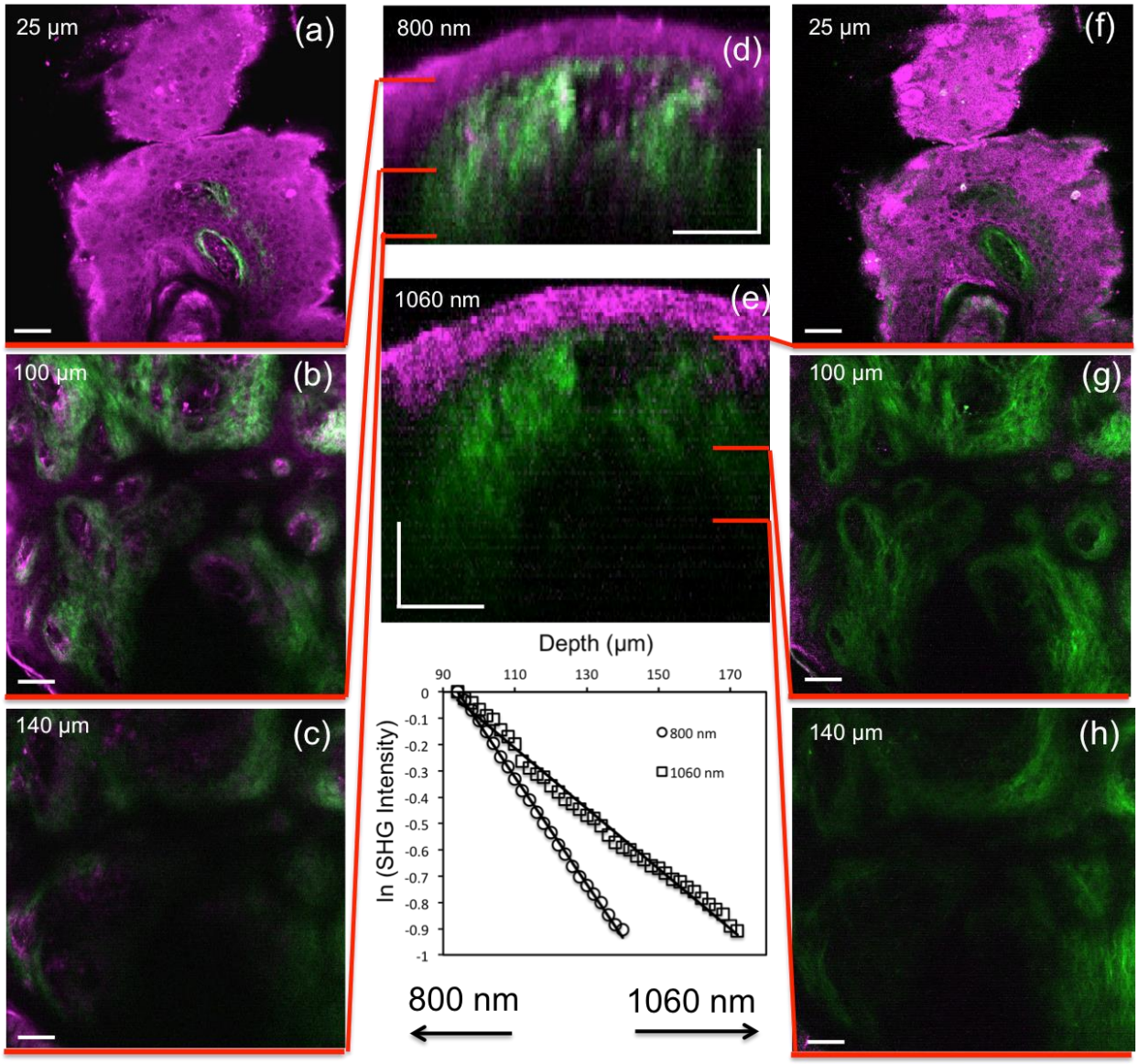

Figure 35. *Ex vivo* imaging of human skin using 800 nm (Ti:Sapphire laser) and 1060 nm (Yb-fiber laser). Horizontal sections (x-y scans) at different depths corresponding to 800 nm excitation wavelength (a-c). The optical sections show images of the epidermal cells through the TPEF signal (magenta, z = 25 µm); collagen fibers (green; SHG signal) and elastin fibers (magenta, TPEF signal) (z = 100 µm; 140 µm). Vertical sections were obtained from 3D reconstruction for 800 nm (d) and 1060 nm (e) excitation wavelengths (40 mW for 800 nm and 20 mW for 1060 nm). Horizontal sections (x-y scans) are shown at different depths corresponding to 800 nm and 1060 nm excitation wavelengths (a-c), (f-h), respectively. The optical sections show images of the epidermal cells through the THG signal (magenta, z = 25 µm) and collagen fibers (green; SHG signal) (z = 100 µm; 140 µm). Scale bar is 50 µm. The plot represents the SHG signal attenuation (logarithmic scale) with depth, for 800 nm and 1060 nm excitation wavelengths.

To compare the penetration depth attained by each excitation wavelength, we adjusted the average laser powers (40 mW for 800 nm and 20 mW for 1060 nm) such that the average intensity of the SHG signal corresponding to the sample surface (z=0) was similar for both wavelengths. The laser power and all the other experimental parameters were kept the same during the data acquisition. The SHG signals measured in the dermis of the skin sample are plotted versus depth in Figure 35 on logarithmic scale. The signal calculated at each depth represents the average of the pixel's intensities in the SHG images at that particular depth. The SHG intensity decay curve was normalized to the maximum intensity value for each wavelength.

The SHG intensity decays as a function of depth, *z* according to: $I_{SHG} \sim exp\ (-Az)$, where *A* is the attenuation coefficient that includes the sample absorption and scattering properties at both the excitation and emission wavelengths. The inverse of *A* yields a *1/e* attenuation length of 49 μm for 800 nm and 88 μm for 1060 nm, an increase of about 80% for the Yb-fiber laser source. Similar results were obtained for all five stacks acquired in the sample, which shows that 1060 nm, sub-40 fs pulses can provide deeper penetration in highly scattering samples, such as skin.

In summary, these results demonstrate the potential of fiber-based laser systems to be used as excitation light sources for NLOM imaging of highly turbid media. Despite their current lack of tunability, short-pulse, >1 μm wavelength fiber lasers can provide a low-barrier-to-access alternative to conventional Ti:Sapphire lasers. They are of particular interest in applications related to *in vivo* imaging of human skin as they can deliver up to 80% improvement in SHG imaging depth compared to conventionally used Ti:Sapphire lasers. An additional benefit for *in vivo* human skin imaging is related to the THG contrast mechanism which, unlike TPEF, does not involve absorption and might allow for the use of higher excitation powers. With continued development of expanded wavelengths, powers, and pulse characteristics, these systems are expected to increase in use, particularly in skin studies where assessment of 3D morphology is important.

3.3 Multimodal imaging with sub-30 fs Yb-fiber laser

Additionally, we tested a novel fiber laser source, capable of delivering a very broadband spectrum centering at 1030 nm. The output pulses were compressed to the T-L duration as short as ~21 fs FWHM [65] using a pulse shaper with MIIPS [25, 26]. This source was evaluated for multi-modal microscopy using fluorescent polystyrene microspheres and unstained biological samples including guppy fish (*Poecilia reticulata*) tails and fruit fly (*Drosophila melanogaster*) wings. Images generated by multiphoton fluorescence SHG and THG were compared.

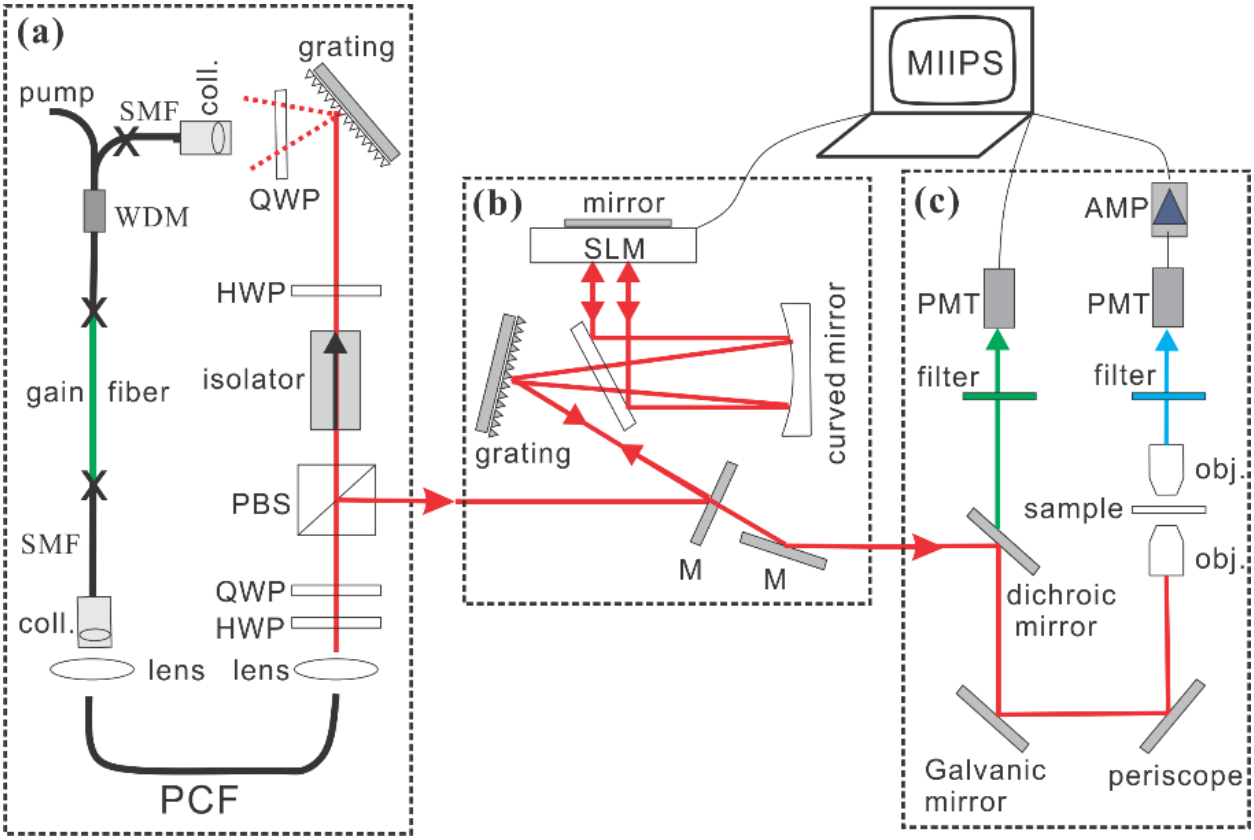

Figure 36. Schematic of imaging setup using PCF rod. (a) Fiber laser cavity layout. SMF: single mode fiber; WDM: wavelength division multiplexer; HWP and QWP: half- and quarter-waveplate; PBS: polarization beam splitter. (b) 4f-folded pulse shaper. SLM: spatial light modulator; M: mirror. (c) Microscope setup. AMP: amplifier; PMT: photomultiplier.

The experimental setup is demonstrated in Figure 36. The Yb-fiber laser oscillator (Figure 36a) generates a broadband spectrum centered at 1030 nm with ~50 mW average output power at a repetition rate of 62 MHz. It is based on an all-normal dispersion cavity scheme and utilizes a segment of normal dispersion photonic crystal fiber (PCF) inside the cavity. Using a narrow intra-cavity spectral filter formed by grating and collimator [89], formation of amplified self-similar pulses is achieved in the gain medium. The self-similar pulses are further extended in both time and spectral domain in the PCF segment. This novel scheme enables the laser spectral bandwidth to exceed the gain bandwidth and leads to pulse durations as short as 20 fs. It introduces a new class of fiber lasers with the potential to generate few-cycle pulses. The laser used in this work provides 10 times lower pulse energy and much shorter pulse duration compared to Yb-fiber laser used in chapters 3.2 - 3.3.

A folded 4-f pulse shaper (MIIPSBox640, BioPhotonic Solutions) (Figure 36b) with a dual mask 640-pixel SLM is used to measure and compensate the phase distortions of the pulses at a desired point [25, 26]. Due to the reflection efficiency of the grating and mirrors inside the shaper, the average laser power out of the pulse shaper was limited to 25 mW. The output pulses are then guided through the microscopy imaging setup (Figure 36c), similar to the design described in chapter 3.2.

The spectrum of the laser pulses used for NLOM is shown in Figure 37a. The laser beam is focused using a 20x objective on a BBO crystal and a 1 mm thick glass slide to generate SHG and THG signals separately, which are measured using a spectrometer. The SHG and THG intensity is obtained by integrating the spectra. By adding second order dispersion to the laser pulses using the pulse shaper, the pulse duration increases and the corresponding multiphoton signal decreases as shown in Figure 37(e), where both SHG and THG signals are normalized to the results with a pulse duration of 50 fs. The dependence of the intensity of SHG and THG on laser pulse duration changes according to $\tau^{-1.01}$ (slope= -1.01±0.02) and $\tau^{-2.2}$ (slope= -2.20±0.2) dependence respectively. This deviation from the theoretical prediction of τ^{-2} is caused by the noise in the experimental measurements of weak THG signal. These results indicate the critical importance of good dispersion compensation in multiphoton microscopy.

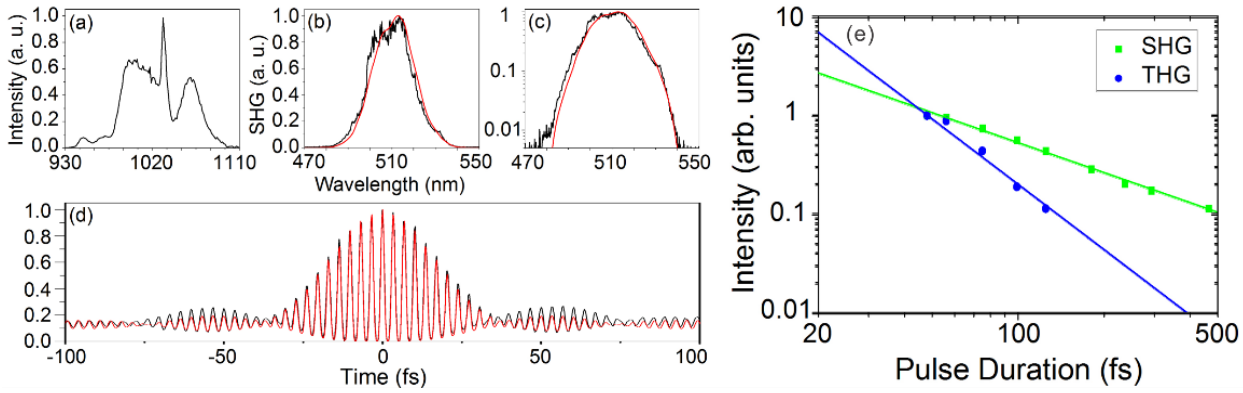

Figure 37. (a) Laser spectrum after the microscope objective. (b) Comparison of experimental (black) and calculated (red) SHG spectrum. (c) Comparison of SHG spectrum on Log-10 scale. (d) Comparison of experimental (black) and calculated (red) interferometric autocorrelation trace. (e) Dependence of intensity of SHG and THG on laser pulse duration.

As seen in Figure 37(d), the measured interferometric autocorrelation FWHM of the pulses at the focal point of the objective is around 38 fs. This corresponds to a FWHM pulse duration of 27 fs, which is longer than 21 fs for the compressed pulse duration measured before the objective. Non-uniform spectral transmittance of the objective, which decreases from 70% to 50% through the 950 nm to 1150 nm spectral range, decreases the intensity of the longer wavelengths spectral components, leading to a pulse broadening from ~21 to 27 fs. It can be improved by use of an objective with suitable broadband coating. After the pulses are compressed and characterized, the KDP crystal is replaced with the microscopy samples. Bright-field images are taken to ascertain location of samples at the objective focus.

Yellow-green Fluorescein, which has an emission from 470 nm to 650 nm, stained polystyrene microspheres (Fluoresbrite® YG Carboxylate Microspheres 6.50 µm, Polysciences Inc.) are used to test the system before imaging living tissues. The signal in the Epi detection corresponds to TPEF, and the signal in the forward direction corresponds to THG. The imaged area of the sample is controlled by the voltage applied to galvanometer mirrors, as show in Figure 38. By comparing the TPEF and THG images, it is clear that THG images have much better contrast (Figures 38 a, b). By limiting the scanning range, the ~1 µm hole can be seen clearly on the 6.5 µm microspheres (Figure 38 c). Significant THG output is generated in uniform media due to the change of refractive index or the nonlinear susceptibility. The index

of refraction of polystyrene is around 1.57 near 1 μm excitation wavelength , which is a big difference compared to the index of refraction of air around 1. So there is sufficient THG signal generated at the surface of polystyrene microspheres for the detection. Unlike THG, the TPEF is due to the omnidirectional emission from fluorescein and has lower axial resolution, providing brightness from out out-of-focus imaging planes. Meanwhile, the THG signal peaks when the interface is at the beam waist position [11]. This explains why some parts of the microspheres are bright and others are dark. Because the microsphere is 6.5 μm in diameter, when the central part is at the beam waist position, the edges will be out of focus, thus reducing the THG signal. It was reported that the THG signal generated at the glass-air interface is used to illuminate the sample [66], which is not the case in our experiments. Otherwise, the background will be all bright. The signal around the beads is due to the fluid surrounding beads. The index of refraction of water is around 1.33, the change in the index of refraction also creates significant THG signal there.

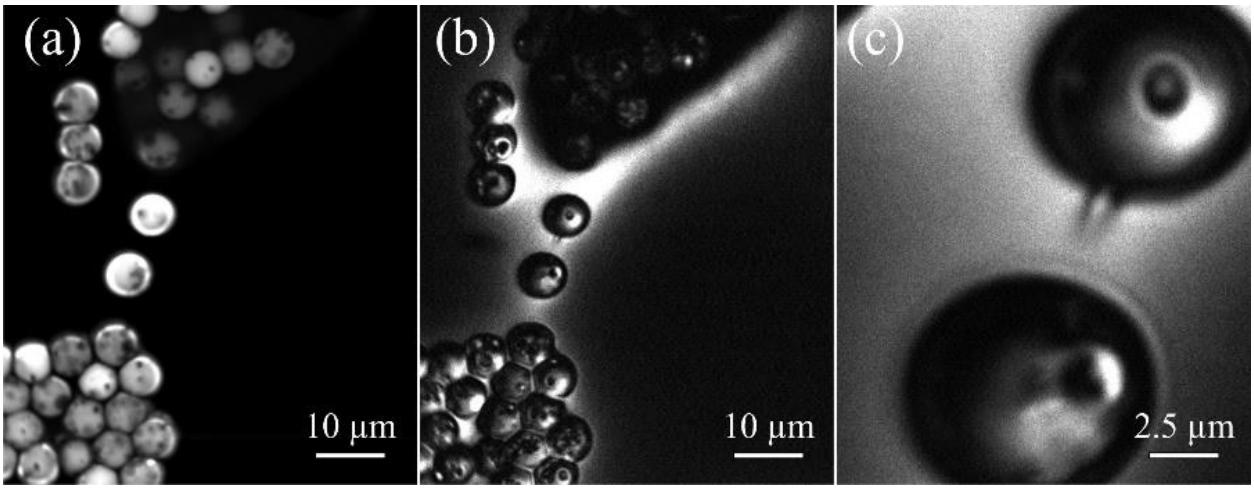

Figure 38. Multiphoton microscopy images of polystyrene microspheres. (a) Two-photon excited fluorescence (TPEF) image (b) THG image (c) THG image of a single microsphere.

After the system is calibrated, unstained samples of a fruit fly wing and a guppy fish tail are used for imaging. The samples are placed onto glass slides, mounted with Tissue-Tek O.C.T. compound (Sakura, CA) and coverglass No.1 (Corning Inc., NY) and allowed to immobilize for 30 min before imaging. The average laser power used for imaging the fish tail is 17 mW. The laser power for imaging fly wings is reduced to 7 mW, because higher power is found to damage the sample. Bright-field images were checked

before and after imaging making sure there is no damage on the sample after excitation (Figure 39 d, h). The SHG (Figure 39 a, c) and THG (Figure 39 b, f) images are shown in false color. By combining SHG and THG images, we can clearly see the complimentary information (Figure 39 c, g). Since the sample of fish tail is thick, comprised of multiple layers of cells, the THG signal is not as intense as the SHG signal in general. However, there is complementary information at the edge of cells provided in the THG images, which is due to the enhanced THG at the interface. For a fly wing, the same process has been done. From the composition of SHG and THG results, it is clearly seen that THG images have better signal from the fine hairs on the wing. The use of sub-30 fs pulses resulted in comparable SHG and THG signal even when using only ~0.1 nJ pulse energy, 7 mW from a 62 MHz repetition oscillator.

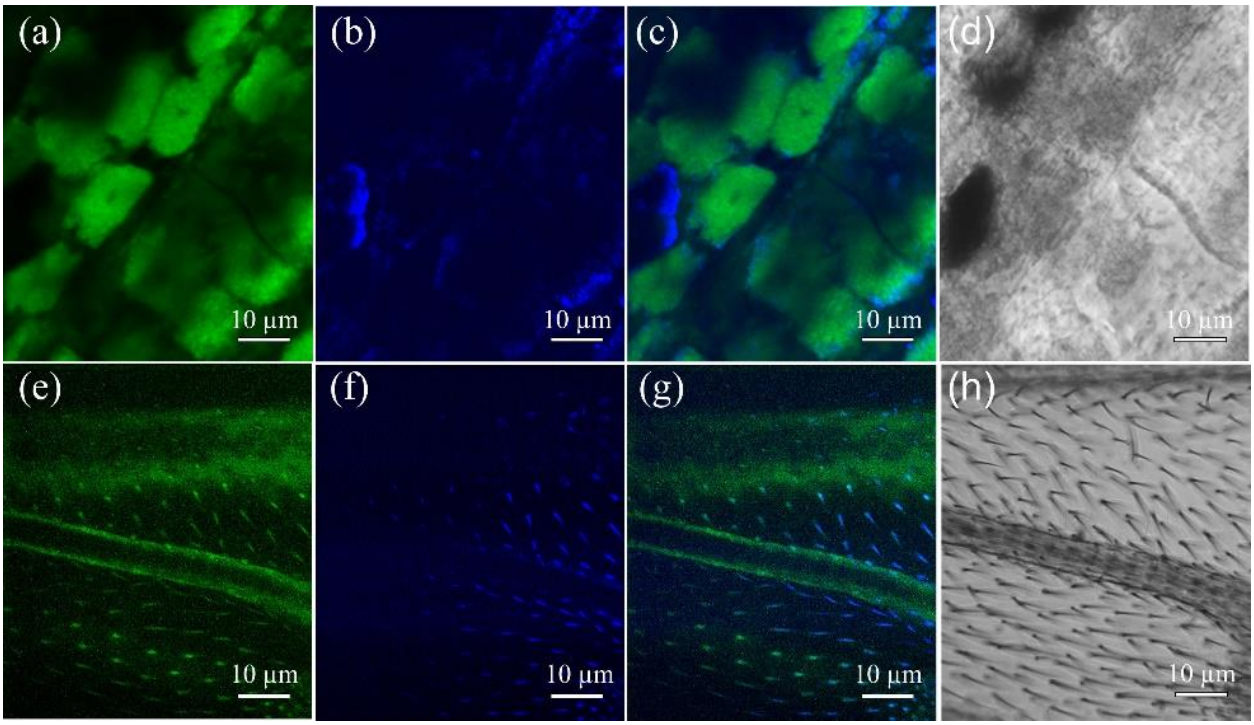

Figure 39. Multiphoton microscopy images of living tissues. (False color) Top line: images of guppy fish (*Poecilia reticulata*) tail. (a) SHG image; (b) THG image; (c) Composition of SHG (green) and THG (blue) images. (d) Bright-field microscope image. Bottom line: images of fruit fly (*Drosophila melanogaster*) wings. (e) SHG image; (f) THG image; (g) Composition of SHG (green) and THG (blue) images; (h) Bright-field microscope image.

Chapter 4 Nonlinear optical microscopy imaging of RBC

TPEF imaging of unstained red blood cells (RBCs) for non-invasive label-free blood analysis and deformability has been deemed undetectable at 800 nm [22, 90, 91]. This assessment is based upon the fact that spontaneous emission is dominated by fast non-radiative decay [22, 90]. RBCs exhibit strong absorption and are known to cast dark shadows in nonlinear fluorescence imaging of capillaries *in vivo* [92]. While increasing laser intensity may yield a fluorescent signal that is strong enough for label-free analysis, the high intensity would likely cause both linear and nonlinear photo-thermal damage to the RBCs, especially when using pulse widths greater than 150 fs. TPEF intensity is highly dependent on the characteristics of the laser source, with shorter pulse durations leading to higher fluorescence emission yields [16, 82]. It follows that short pulse durations may lead to appropriately high levels of TPEF signal, while limiting nonlinear photo-thermal damage for optimal non-destructive imaging.

The long-term storage of RBCs leads to known changes in their health status. Current protocols call for the destruction of these stored blood components after 42 days, even though this degradation is not monitored or tracked. As RBCs age, they lose the important flexibility and deformability that enables them to squeeze through small capillaries to deliver oxygen to tissue; this capability cannot be regained after transfusion occurs [93, 94]. Indeed, the effects of older than 14 days transfused blood on mortality have been the subject of numerous studies [95-98]. Recent work analyzing RBC cell membrane deformability before and three days following surgery found that storage times longer than three weeks led to irreversible damage to RBCs, which are then removed by the liver [93, 94]. If blood could be analyzed quickly and non-invasively prior to a transfusion, it may be possible to assess stored blood for damaged RBCs and thus reduce the risk of postoperative complications. Non-invasive analysis further opens the possibility to examine whether stored blood samples could retain healthy RBCs for times longer than the standard 42 days, thus extending the availability of normally limited blood supplies.

Non-invasive monitoring of RBC health via changes in cellular morphology can be accomplished, in principle, by imaging RBCs through the blood bag. Previous optical imaging studies of RBC morphology

have required breaching the storage bag; these efforts, like those described above, found irreversible changes to the morphology with increasing storage duration [99-101]. Nonlinear optical imaging of RBCs has been accomplished via several different methods including two-photon absorption (TPA) [22, 102], TPEF [91, 103], and THG [104, 105]. For TPA imaging, an intensity modulated pump pulse train at 775 nm and delayed probe at 650 nm were employed based upon the different excited state dynamics of oxyhemoglobin and deoxyhemoglobin [102]. TPEF imaging was accomplished by using bandpass filters to select wavelengths from a femtosecond supercontinuum source spanning 600-750 nm [91, 103]. It was reported that the fluorescence signal severely diminished when the excitation wavelength exceeded 750 nm [91], with the fluorescence emission attributed to two-photon excitation of the Soret band in hemoglobin. THG images of RBCs, on the other hand, were efficiently generated by tuning the excitation wavelength to achieve resonant enhancement via the Soret band [104, 105].

We propose a method to image RBC morphology that does not require breaching the sterile environment of the blood storage bag. This consideration distinguishes the present study from prior work in that it provides a solid foundation for assessing RBC status non-destructively in a clinical setting. Here we explore TPEF, three photon excited fluorescence (3PEF), and THG modalities and compare these different contrast mechanisms to determine guidelines for imaging RBCs in storage while maintaining sterility. Nonlinear imaging with pulses shorter than 50 fs using an Yb-fiber laser has been shown to produce enhanced THG images of tissues [65]; here, we used a short-pulse Yb-fiber oscillator [53] to produce 3PEF and THG images of RBCs. Moreover, TPEF imaging of RBCs performed with a central wavelength of 800 nm is demonstrated for the first time. Linear absorption, TPEF spectra, fluorescence lifetime measurements, and transient absorption are performed to reveal the constituent responsible for the TPEF signal.

4.1 Materials and methods

The laser beam, from either an Yb-fiber [53] or Ti:Sapphire (KM labs, Boulder, CO) laser oscillator, propagates through the pulse shaper (MIIPSBox640, BioPhotonic Solutions Inc., East Lansing, MI) and is scanned by a pair of galvanometer mirrors (QuantumDrive 1500, Nutfield Technology, Inc., Hudson, NH) as illustrated in Figure 40. The estimated pulse duration at the focal plane of the objective is approximately 3 ps before compressing it with MIIPS for both lasers [82]. The measured FWHM pulse duration at the focal plane is 45 fs for the Yb-fiber laser and 15 fs for Ti:Sapphire laser pulses after the compression. A chamber containing prepared RBCs was mounted on the 40x water immersion objective (Zeiss LD-C APOCHROMAT 1.1 NA, Jena, Germany) of the TE200 inverted microscope (Nikon, Tokyo, Japan), modified for multi-photon microscopy.

The combined SHG and TPEF signals from the sample were collected in the epi-direction. Descanning and separation from the incident light was performed using a combination of a 635 nm dichroic mirror (Di02-R635-25x36, Semrock Inc., NY) and a short-pass emission filter (ET680-SP-2P8, Chroma Technology Corp., VT). The SHG/TPEF signal was detected by a PMT detector (HC20-05MOD, Hamamatsu, Japan). In the forward direction, THG and 3PEF were collected by a 15x objective (ReflX for UV, NT59-886, NA 0.28, Edmund Optics Inc., NJ) and filtered by a combination of 410 nm and 680 nm short-pass filters for suppression of the excitation light. This filter combination, however, was not sufficient to distinguish between THG and 3PEF. The signal was recorded by another PMT detector (H10720-210, Hamamatsu, Japan). Separate detection channel signals were digitized by a PC data acquisition board for further image reconstruction using home-built software in LabVIEW (National Instruments, TX). Tens of images were collected at 1 frame per second, averaged, and post-processed using ImageJ (NIH, MD, USA) software.

TPEF spectra and lifetime decay measurements were carried out in the epi direction using a 16 channel time-correlated single photon counting (TCSPC) system (SPC-830, Becker & Hickl GmbH, Berlin, Germany).

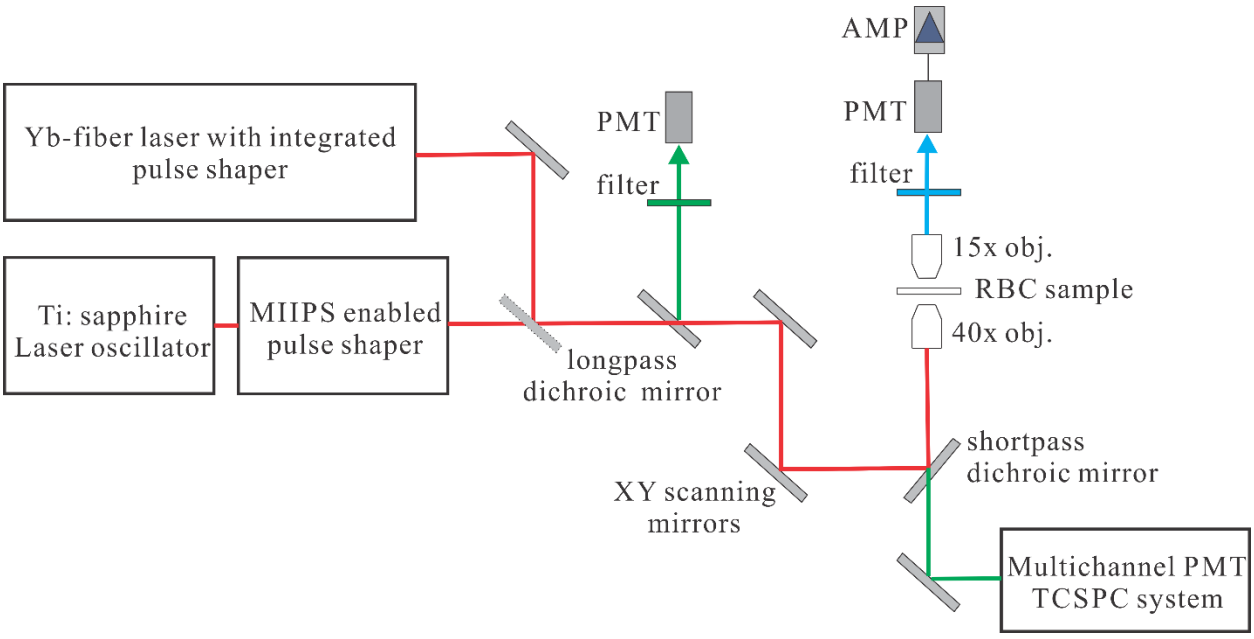

Figure 40. Schematic diagram of the microscopy setup for multi-photon imaging using different lasers. Ti:sapphire or Yb-fiber laser oscillators can be used one at a time.

A separate system was also used to measure the transient absorption properties of hemoglobin, which relies on the sequential stepwise absorption of two photons from the ground state to a final excited state via an intermediate excited state. This was performed with a tunable dual-output pulsed femtosecond laser source (Spectra-Physics Insight DeepSee, Santa Clara, CA), using the fixed 1040 nm output as the pump beam and the tunable output set to 735 nm as the probe beam. Intensity modulation of the 1040 nm beam was achieved using an electro-optic modulator (Thorlabs EO-AM-R-20-C2, Newton, NJ) with 20 MHz modulation. Imaging was carried out on a modified confocal microscope (Olympus FV1000, Center Valley, PA) using a 1.20 NA 60x water immersion objective (Olympus UPLSAPO 60XW, Center Valley, PA). Forward detection was achieved using a photodiode coupled to a lock-in amplifier (APE Lock-in Amplifier, Berlin, Germany) placed downstream of a 710 nm LP filter (Chroma E710LP, Bellows Falls, VT) and a 950 nm SP filter (Thorlabs FES0950, Newton, NJ). This configuration allows the transmission of the 735 nm probe beam to the photodiode while blocking the 1040 nm pump beam, where the lock-in amplifier can detect any intensity modulation transfer from the pump beam to the probe beam at the 20

MHz modulation frequency. The output of the lock-in amplifier is then fed into an Olympus input-output box system and digitized for acquisition by the Olympus Fluoview confocal microscopy control software.

All procedures involving human subjects, including consent forms, were approved by the Biomedical and Health Institutional Review Board (BIRB) at Michigan State University as well as the Massachusetts General Hospital IRB and Institutional Animal Care and Use Committee. Whole blood was obtained from consented healthy human donors by venipuncture and collected into heparinized tubes [106]. Upon collection in a citrate phosphate dextrose buffer solution, the blood was immediately centrifuged for 10min at 500*g* and 4°C. The plasma and leukocytes were removed by filtration and the RBCs were added to an AS-1 storage solution. RBCs were subsequently diluted from ~70% to 0.4% in AS-1 solution for imaging. The blood bag used for storage was manufactured from 200 gauge PVC film (Uline, WI) - the same as used for commercial storage - and hermetically enclosed by thermal splicing [107].

Erythrocyte ghosts (the resulting RBC membrane with all other intracellular components removed) were prepared according to a following wash protocol. RBCs were suspended in PBS, then washed 3x at 500*g* for 10 minutes with the supernatant aspirated off after each wash. Four 40 μL aliquots of compact RBCs suspended in 1 mL lysis buffer (described below) were then centrifuged at 22,000*g* for 15 minutes. After discarding the supernatant, the remaining membranes were washed in lysis buffer 3x at 22,000*g* for 5 minutes. Finally, the supernatant was discarded, and the lysates were pooled. Lysis buffer was prepared by mixing 10 mM Tris-HCl with 0.2 mM ethylenediaminetetraacetic acid (EDTA) at pH 7.2. The linear absorbance of erythrocyte ghosts was measured using a Unicam UV-2 spectrophotometer (ATi Unicam, Cambridge, UK) in a 1 mm quartz cuvette.

4.2 Results

4.2.1 Multiphoton excited fluorescence microscopy imaging of RBCs

TPEF images of human RBCs were obtained with the 800 nm Ti:Sapphire laser as shown in Figure 41. Individual RBCs and their central pallor can clearly be seen.

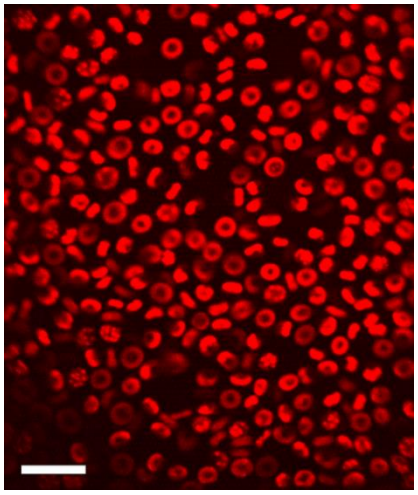

Figure 41. TPEF image of unstained human RBCs imaged by 15 fs pulses with 10 mW average power from the Ti:Sapphire laser tuned to 800 nm.

The possibility of photodamage was carefully considered. At lower excitation power (less than 5 mW) the TPEF/3PEF signals are very weak, but no signs of photodamage were observed in RBC appearance after less than 2 min of exposure. With an increase of excitation power to 10 mW or 22 mW using 800 nm or 1060 nm lasers, respectively, we observed both cell shrinkage and an increase of the fluorescence signal after tens of seconds of exposure. Similar photodamage effects on RBCs have been reported during optical trapping of human erythrocytes [108].

RBC morphology can be clearly seen in Figure 41 and is important for determination of hematologic diseases. In fact, many diseases have normal blood counts but abnormal membrane morphology [109]. Under normal circumstances, mature RBCs are round biconcave disc-shaped cells measuring 7-8 μm in diameter. It is well known that preparation of fresh blood between coverslips can affect RBC appearance, where they can become echinocytes (star shaped RBCs) [110]. Moreover, the blood collection tube is internally coated with EDTA. While its role is to prevent coagulation of collected blood,

there is a possibility that echinocytosis may occur upon contact of RBCs with the EDTA coating. In the blood storage bag, however, the concentration of EDTA is low enough that echinocytosis is not likely to occur. Nevertheless, we expect that other possible morphological deformities such as elliptocytosis, cigar cells, schistocytosis, and sickle cells can be determined by non-destructive TPEF/3PEF imaging.

4.2.2 Nonlinear microscopy imaging of RBCs through PVC bag using Yb-fiber laser

THG microscopy does not require fluorescence from the molecule; THG signal generation only requires a change in the index of refraction at the focus [11]. While THG typically requires high peak intensities for imaging, this limitation is easily overcome by using shorter pulses and a lower average power. In Figure 43, the images were generated with less than 8 mW of average laser power at the objective focus. THG images of RBCs outside the blood bag (i.e. on a glass cover slip) are shown in Figure 42. Compared to TPEF, the RBC membrane boundaries are clearly seen on the THG image. The non-zero background in Figure 42 is a direct result of the out-of-focus THG signal generated from the glass-liquid interface.

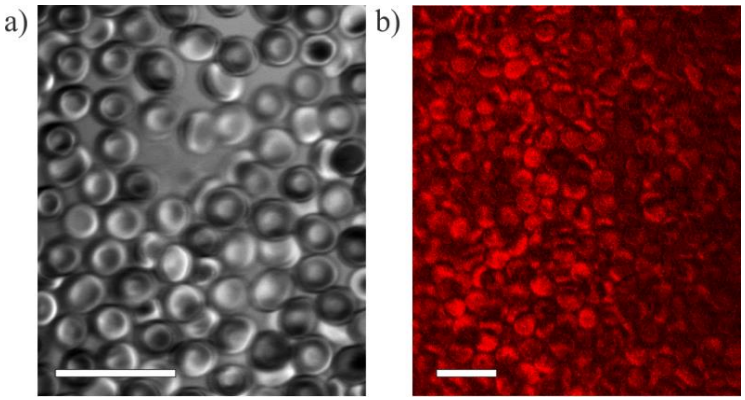

Figure 42. THG microscopy imaging of human RBCs on the glass cover slip obtained using a 1060 nm Yb-fiber laser emitting 45 fs pulses with 8 mW average power. a) Static image; b) a frame from a video of flowing RBCs. Scale bar is 20 μm.

Precise morphology measurements such as RBC size can be performed with or without the blood bag. We used an Yb-fiber laser with a central wavelength of 1060 nm and 45 fs duration pulses to image RBCs through a PVC plastic bag, as shown in Figure 43. The nonlinear optical signal was detected in both trans- and epi-directions, as shown in Figures 43a and 43b, respectively. For the trans-direction acquisition, images were obtained near the edge of the plastic bag where the thickness of the RBC sample was thin and

thus absorption of the THG signal was minimized. In the epi-direction, on the other hand, imaging can be performed anywhere in the bag. The shape of RBCs can be clearly seen in both images. The average excitation power was maintained below 20 mW in order to avoid damaging the PVC bag.

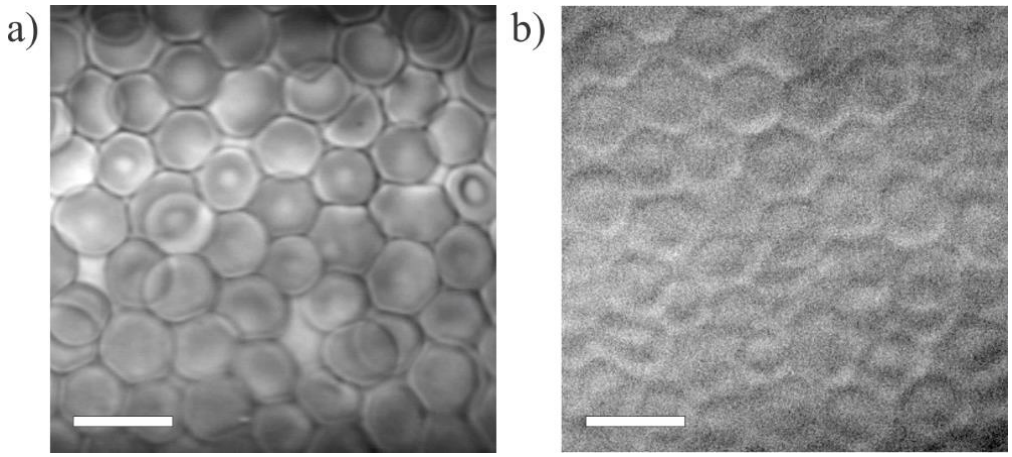

Figure 43. THG images of RBCs detected through the PVC storage bag in trans- direction (a) and in epi-direction (b) excited by 7 mW average power from an Yb-fiber laser. Scale bar is 10 μm.

4.2.3 The source of fluorescence in RBCs

TPEF and 3PEF fluorescence from RBCs and erythrocyte ghosts has a broad emission spectrum from 400 nm to 570 nm with a peak around 480 nm that can be excited by two 800 nm or three 1060 nm photons. This weak fluorescence emission from blood has been attributed to a number of sources in past studies, including flavin-containing molecules such as flavin adenine dinucleotide (FAD) and riboflavin, nicotinamide adenine dinucleotide (NADH) [111], hemoglobin [91, 102] and its fluorescent catabolites – biliverdin and bilirubin. Although tryptophan is a major endogenous fluorophore, it does not emit fluorescence in the spectral window of interest. We investigated TPEF emission from RBCs, erythrocyte ghosts, NADH, biliverdin, bilirubin, riboflavin and hemoglobin. The TPEF lifetime decays were measured and compared with one-photon excited (355 nm centered 12 ps laser pulses) fluorescence lifetime decays for the same samples (Figure 44). Bilirubin, RBCs and erythrocyte ghosts did not exhibit detectable fluorescence upon one-photon UV excitation and are thus not present in Figure 44a. Table 1 summarizes fluorescence lifetimes for one-photon excitation measurements, while Table 2 shows TPEF lifetimes obtained by fitting decay curves using single and double exponential decay model fits.

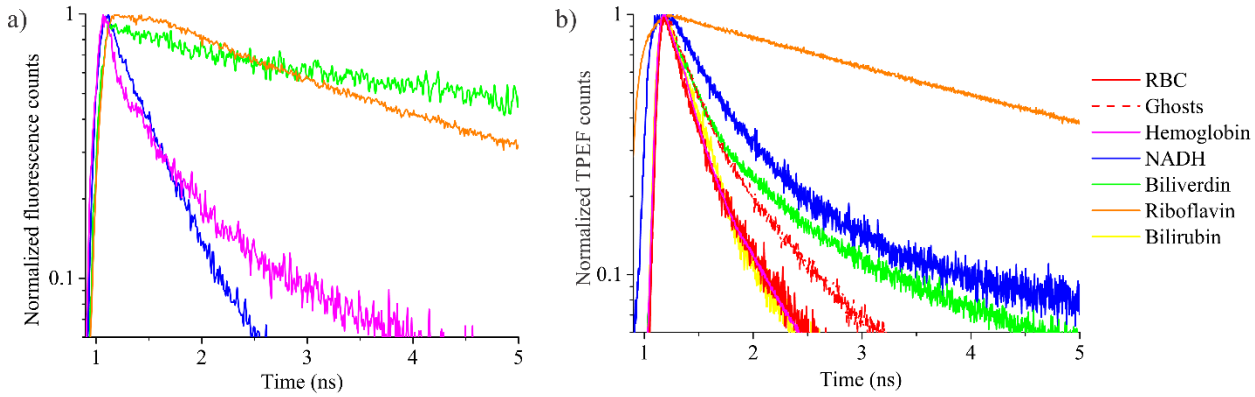

Figure 44. (a) One-photon excitation (355 nm, 12 ps) fluorescence decay curves of hemoglobin, NADH, biliverdin and riboflavin compared to (b) TPEF (800 nm, 15 fs) decay curves for RBCs, their membranes and reagent-grade hemoglobin, biliverdin and NADH.

Table 1. Fluorescence lifetime decays obtained from fitting one-photon excitation (355 nm) curves using single and double exponential models.

	A1, a.u.	τ1, ps	A2, a.u.	τ2, ps
20 μM NADH in PSS	0.95±0.04	412±32	0.05±0.04	2416±400*
100 μM NADH in PSS	0.99±0.03	441±29	0.013±0.031	3093±400*
50 μM Riboflavin in PSS			1	3513±9
2 g/L Hemoglobin in PSS	0.68±0.04	223±3	0.32±0.04	1547±15
1 mM Biliverdin in PSS			1	3272±300

Table 2. Fluorescence lifetime decays obtained from fitting two-photon excitation (800 nm) curves using single and double exponential models.

	A1, a.u.	τ1, ps	A2, a.u.	τ2, ps
12 g/L Hemoglobin in PSS	0.88±0.04	280±20	0.12±0.04	1260±300
50 μM NADH in PSS	0.85±0.05	520±40	0.16±0.05	2140±470
50 μM Biliverdin in PSS	0.77±0.02	320±20	0.22±0.02	2180±140
50 μM Bilirubin in PSS	0.98±0.01	330±10	0.02±0.01	3700±1500
50 μM Riboflavin in PSS			1	4000±50
Ghosts in PSS	0.75±0.07	320±40	0.25±0.07	1340±250
RBCs in PSS	0.83±0.06	260±30	0.18±0.06	1170±280

TPEF emission spectra of RBCs, their membranes, and commercially obtained fluorophores are shown in Figure 45a. To measure quantitatively the similarity between TPEF spectra, we calculated the Pearson correlation coefficients between the fluorescence spectrum of RBCs and that of other samples, as summarized in Table 3. Both bilirubin and riboflavin's weak Pearson correlation coefficients of 0.552 and 0.208, respectively, suggest that they are not responsible for RBC fluorescence. Furthermore, riboflavin was omitted from the comparative plot of TPEF peak wavelength vs. fluorescence lifetime (Figure 45b), because its lifetime is over an order of magnitude longer than that of RBCs and ghosts. We therefore conclude that the observed TPEF emission from RBCs and ghosts indeed originates from hemoglobin.

Table 3. TPEF emission spectra similarity coefficients.

RBC	Ghosts	Hemoglobin	NADH	Biliverdin	Bilirubin	Riboflavin
1.000	0.995	0.975	0.939	0.883	0.552	0.208

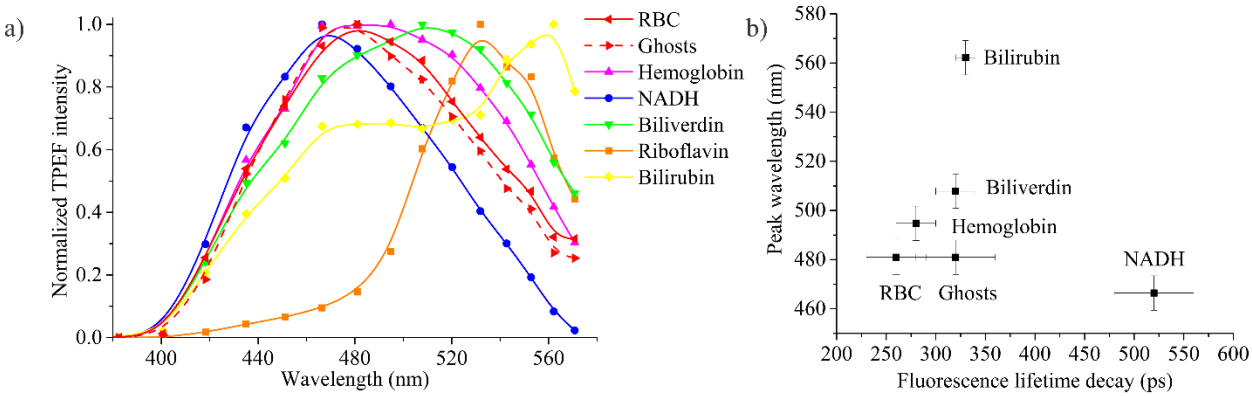

Figure 45. (a) TPEF (800 nm, 15 fs excitation) emission spectra for RBCs, erythrocyte ghosts and reagent-grade fluorophores. (b) TPEF peak wavelength vs decay lifetimes for RBCs, their membranes and reagent-grade hemoglobin, biliverdin and NADH.

It is well known that RBCs are densely packed with large amounts of hemoglobin. Hemoglobin is also bound to the membrane, as has been determined after several washes [112]. The absorption spectrum of hemoglobin originates from heme, having an intense Soret or B-band (~400-430 nm, depending on the oxidation state) and weak transition to the Q-band (~550 nm). It is known that the fluorescence emission of hemoglobin is undetectable with one-photon excitation; however, TPEF imaging of hemoglobin has

recently been demonstrated using two-photon excitation wavelengths ranging from 550 nm to 750 nm [113]. TPEF of hemoglobin excited at 800 nm has not been reported in any prior work, despite hemoglobin's large two-photon absorption at longer wavelengths, with a maximum around 825 nm [102].

Further confirmation of the participation of hemoglobin was obtained by comparing transient absorption decay curves for pure hemoglobin and purified RBCs in Figure 46a. In these experiments, we monitor transmission of 735 nm photons as a function of time following excitation with 1040 nm photons. Absorption at 1040 nm is likely associated with the absorption of oxyhemoglobin at that wavelength. The similarity between the two suggests that the fluorescent signal from RBCs is the result of an excited state of hemoglobin, as opposed to other potential fluorophores. Background signal from the PBS solution appeared strictly when the two pulse trains were overlapped, likely due to the optical Kerr effect from the water solvent [114]. To confirm the presence of hemoglobin in the RBC membrane, we washed erythrocyte ghosts up to 4 times using the washing protocol above and the absorbance was measured after each consecutive wash (Figure 46b). We found the level of hemoglobin reached a plateau instead of continuing to decrease, indicating the presence of bound hemoglobin within the RBC ghosts.

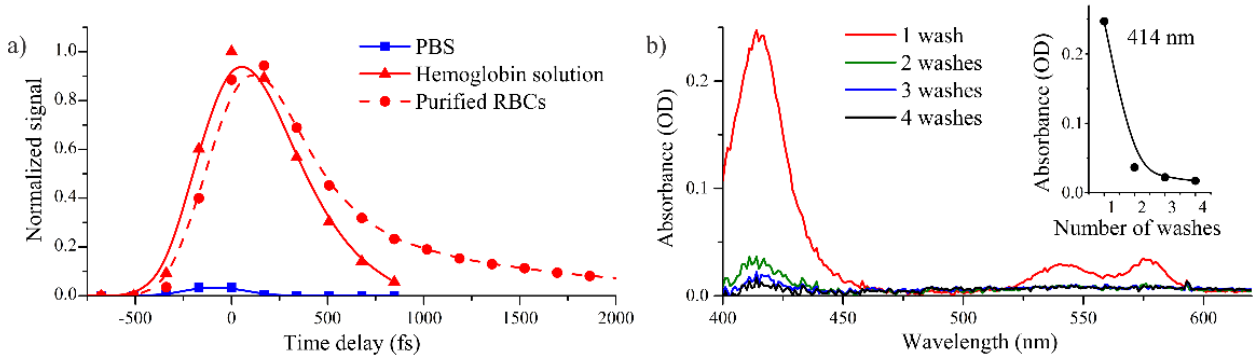

Figure 46. a) Transient absorption measurements of PBS, hemoglobin solution and purified RBCs following 1040 nm pump and 735 nm probe. b) Absorption spectra of PBS solution with ghosts washed 1 to 4 times. Inset shows absorbance of ghosts after varying number of washes, probed at 414 nm. Spectra were corrected for background and Rayleigh scattering.

Chapter 5 Study of photodamage induced by fs NIR pulses on a living organism

Photodamage is known to be a major concern in laser scanning imaging of living biological samples via multiphoton microscopy [4, 115]. Multiphoton imaging systems are capable of directly imaging tissues through nonlinearly excited fluorescence and second harmonic signals [116]. The use of near-infrared (NIR) femtosecond pulses can provide high resolution images of tissue morphology even without the use of contrast reagents [117]. Using focused ultrafast laser pulses in the NIR also makes it is possible to reach deeper tissue layers compared to UV light irradiation [118]. However, the photodamage that results from using laser irradiation has been an outstanding concern in regard to sample perturbation for *in vivo* imaging, especially for purposes of medical diagnostics [119, 120]. There are a number of nonlinear multiphoton optical process contributors that may lead to phototoxicity in cells [115, 121, 122], including the generation of reactive oxygen species [122, 123] and free radicals [124, 125], direct DNA damage [125-127], and plasma formation [124, 128]. Linear photodamage from heating due to infrared laser irradiation [129-131] is a problem that is particularly detrimental to pigment-rich and highly-vascularized tissues [120, 131].

The availability of a wide variety of commercial laser sources prompts the question of optimal energy parameters for safer imaging of living tissues. Due to the complexity of evaluating the short and long term effects of laser irradiation on living tissues, the ideal approach for determination of safer *in vivo* imaging conditions is still in debate. Adequate and reliable detection of laser-induced photodamage is an important part of the solution to this problem and numerous evaluation methods have been developed to target such damage in living tissues. Most of these methods are mechanism-specific techniques and include: tracking DNA damage by detecting DNA strand breaks [124, 125, 132, 133] and DNA repair proteins [125, 127], the level of apoptosis [134], mutagenicity risks [117], etc.; alternatively, observing oxidative stress and mitochondrial dysfunction thru monitoring of reactive oxygen species [117], H_20_2 [135], or NADH [69, 130, 136]; and checking for changes in the functional activity of the cells by scoring the resting [Ca^{2+}] level [69, 115] or cell viability (cloning efficiency) [8, 119, 122].

It is also known that a small increase in local temperature of even a few degrees centigrade may induce significant damage in living tissues. For example, viability of human adipocytes dropped from 89% to 20% when subcutaneous temperature increased from 45 to 50°C during a 1 minute exposure, while only 40% of viability was lost during three minutes of exposure at 45°C [137]. This thermal damage consists of two stages, both affecting cell injury and necrosis. The first stage is due to heat-induced protein denaturation and cell death, and the second is the result of an intense inflammatory reaction, which, due to increased vascular permeability, causes burn shock [138, 139]. This can eventually lead to a disruption of intracellular ion homeostasis, nuclear and cell membranes, leading to cell swelling and the release of injurious lysosomal enzymes and inflammatory messenger molecules. Endogenous self-adjuvant (also termed as damage-associated molecular patterns) released during necrotic cell death could also induce sterile inflammation and immune responses [140]. In addition to thermal injury, physical (mechanical) trauma could be another cause of the development of the necrotic process in tissues [140].

The second major mechanism of photodamage induced by the laser pulses is DNA damage [125, 126, 141, 142]. Apoptosis is a prominent route of cell death following the introduction of DNA damage [143, 144], and it has been shown that DNA strand breaks may trigger apoptosis [143]. To link DNA damage with apoptosis, proteins [145, 146] or free radicals, particularly reactive oxygen species (ROS) [144, 147, 148], can be used, both of which can be formed by various photochemical processes (including femtosecond NIR laser pulses) [124, 149]. For example, the formation of ROS is also a mechanism contributing to DNA damage [125]. Relying on these data we chose to consider apoptosis observed in irradiated tissues as resultant of DNA damage.

The fluorescence signal and observation time are limited by phototoxic effects [121, 150]. The photodamage study on Chinese hamster ovarian cells irradiated with femtosecond laser pulses within the range 120–1000 fs with 10 mW mean power (for 150 fs pulses at 780 nm: 800 W peak power and 1.2×10^{12} W/cm² peak intensity) showed that photodamage strongly depends on pulse duration, following approximately a P^2/τ dependence (where P is mean power and τ is the pulse duration full-width at half maximum), and is likely based on a two-photon excitation process rather than a one- or a three-photon event

[122]. Relying on the imaging experiments on rat neocortical neurons stained with Ca^{2+} indicator dye, another group formulated a power law with an exponent of 2.5 for the rate of fluorescence increase and proposed that a two-photon excitation mechanism is mainly responsible for the cumulative photodamage of pulses with duration ≥75 fs [121]. Similar results were obtained in experiments on bovine adrenal chromaffin cells, stained with Ca^{2+} indicator dye and irradiated with 190 fs pulses at 840 nm. It has been shown that the photodamage threshold is proportional to the integral (over space and time) of laser intensity raised to a power ~2.5 [115]. Authors proposed that destructive photodamage of biological samples is caused by a multiphoton process, maybe a mixture of two- and three-photon absorption, or by a two-photon absorption followed by partially saturated secondary process. They suggested that, at low excitation intensities, damage may be dominated by a two-photon absorption process, but higher order mechanisms become important at higher excitation powers, while no significant one-photon absorption (heating) takes place [151].

The opposite conclusion was made in the *in vivo* study, where 120 fs pulses (76 MHz repetition rate) and continuous-wave (CW) irradiation were delivered to rhesus's paramacular retinal regions over 0.25 sec at 800 nm. Nearly identical damage thresholds indicated a primarily thermal tissue damage mechanism [152]. Thermal mechanical damage (the formation of cavitation) associated with one-photon absorption of infrared excitation light by melanin granules was reported in studies on skin specimens [84]. The experimentally established thermal mechanical damage threshold was consistent with a simple heat diffusion model for skin under femtosecond pulse laser illumination.

Another possible mechanism for the photodamage produced by femtosecond laser pulses is destructive intracellular optical breakdown or ablation [151, 153, 154]. Because ultrashort laser pulses are extensively employed in applications of micro- and nanostructuring, nanosurgery and biophotonics [155, 156], there are many experimental studies on various ablation effects, produced by femtosecond laser pulses in living cell and tissues [154, 156-162].

Femtosecond pulses may produce ionization of transparent material via two different processes: 1) multiphoton ionization and 2) avalanche ionization [159, 161, 162]. Some authors consider these processes

to be achieved by the high peak intensity of these pulses which can reach ~10^{13} W/cm^2 [159]. Voronin and Zheltikov estimated the critical number of free electrons generated within the laser-tissue interaction region per photon emitted as a nonlinear optical signal (a measure of the "noninvasiveness" of nonlinear optical imaging techniques) for a broad variety of biomarker dyes and bioactivity reporter proteins. The threshold is exceeded above 10^{12} W/cm^2 [163]. For example, ionization of water in the focal volume of a 0.65 NA objective requires 0.1 μJ using 100 fs pulses at 800 nm [158]. The use of the high NA objectives allows production of the ionization and associative ablation using femtosecond pulses with even lower pulse energy. For example, low millisecond exposure of sub-20 femtosecond 75 MHz near infrared laser pulses with an average power of less than 7 mW (<93 pJ) using an objective with NA=1.3 produced transient nanopores in the cell membranes of human pancreatic and salivary gland stem cells [160]. Tight focusing using high numerical aperture microscope objectives allows for a reduction of the pulse energy, enhanced precision, and limits additional undesirable nonlinear side effects observed during optical breakdown and plasma formation (self-focusing, filamentation and plasma-defocusing) [155].

The energy from the recombination of ions and electrons (separated by ionization) contributes to highly unstable conditions and can lead to a microexplosion, shockwave, and bubble formation [158], which result in mechanical disruption of tissues [164, 165]. Moreover, ionization can also induce chemical reactions, for example the formation of ROS and the direct breaking of chemical bonds in cellular structures [159], which can also lead to biological effects in treated cells and tissues [128]. For example, near infrared 170 fs laser pulses operating at 80 MHz repetition rate and at mean power of >7 mW evoked the generation of reactive oxygen species such as H_2O_2 in rat kangaroo kidney epithelium cells, leading to their apoptosis-like death [134].

Despite a respectively high number of publications on femtosecond laser photodamage, we found few studies conducted with undissected and unlabeled living animals (*in vivo*). Many *in vitro* studies showing a variety of photodamage processes are set at similar power levels with similar exponents in suspensions of fluorescently stained living cells [115, 121, 151, 166].

In the present intravital imaging study, we analyzed the photodamage produced by 19 fs, 42 fs, and 100 fs laser pulses at average powers of ~5 mW and ~15 mW centered at a 800 nm wavelength in the undissected and unlabeled samples of living *Drosophila* larvae (*in vivo*). Using these experimental conditions, we tested whether the laser-tissue interaction process resulting in photodamage in living organism is linear or non-linear. We also compared our data on the ablation *in vivo* with the predictions of theoretical models of laser ionization.

Here we explore the incidence of death in developing *D. melanogaster* (irradiated in the larva stage) as a result of photodamage and determine its dependence on laser parameters for 100 fs and 37 fs pulses. We score the levels of necrosis and apoptosis induced by the laser in the larvae as additional parameters to determine possible mechanisms involved in the observed deaths. Mathematical modeling is used to analyze the experimental data. A sigmoidal dose-response function is found to fit our data and allows us to determine three regions. The first region, where there is no statistical difference between irradiated larva and control (not irradiated); the second region where death increases with laser energy, and a third region where the majority of the larvae die. We identify the second region as the region of interest for nonlinear optical imaging, because greater pulse energy causes much brighter images. The goal of our project, within the context of the second region, is to determine if longer or shorter pulses are best for nonlinear optical microscopy such as TPEF. Comparison between the dependence of deaths on the level of two-photon signal for each pulse duration provides evidence that for a given TPEF signal intensity, shorter pulses cause less lethality than longer pulses. The quantitative analysis of experimental data showed that photodamage, scored as lethality in populations of living *Drosophila* larvae evaluated 14 days post exposure, following irradiation with 37 fs or 100 fs laser pulses (1 kHz repetition rate) at 800 nm during 10 minutes, has a mostly linear character on energy fluence per pulse.

5.1 Materials and methods

5.1.1 *Drosophila* culture and sample preparation

A wild type strain of *Drosophila melanogaster* (a gift of Dr. Chuck Elzinga from Michigan State University) was used in this study. The flies were grown at room temperature in culture vials with instant *Drosophila* fly culture media supplemented with yeast (all were purchased from Carolina Biological Supply Company, Burlington, NC). Experiments were performed during the third instar larvae, collected from the upper part of the medium in the vial and rinsed with distillated water and anesthetized with FlyNap (Carolina Biological Supply Company, Burlington, NC) for 30 min prior to the preparation of whole-body (undissected) samples. The whole-body samples of living *Drosophila* larva were prepared by using the protocol developed by us to accommodate *in vivo* imaging. An anesthetized larva is placed on the glass slide (VWR International, Radnor, PA), embedded with O.C.T. Compound Tissue-Tek (Sakura Finetek USA Inc., Torrance, CA) and mounted with cover glass No. 1 (Corning Inc., Corning, NY). The larva immobilized inside the mounted preparations is surrounded by spaces occupied with bubbles of atmospheric air; this allows the animal to breath inside the sample during the experiment. The mounted sample was allowed to solidify for more than 1 hour prior to the procedure of irradiation and imaging. Several preliminary experiments showed that larvae immobilized in the mounted samples were alive during many hours after solidifying: all the larvae in the disassembled chambers demonstrated active movement and were reactive to mechanical stimuli. Checking the larval heart beat after irradiation with the use of light microscopy also showed life in all of the larvae. We used the same methods to verify signs of life in the animals during the experimental series.

5.1.2 Irradiation and imaging of living *Drosophila* larvae using laser scanning microscopy system

The ability of ultrashort femtosecond near infrared laser pulses with various durations (19 fs, 42 fs and 100 fs) and intensities to induce photodamage in living tissues of whole (undissected) organisms was tested by placing the whole-body embedded samples of *Drosophila* larvae under the focused laser pulses (spot diameter ~364 nm estimated from diffraction limit) scanned on the larval inner tissues (32 μm × 32 μm in

size, the formal resolution ~0.063 μm/pixel, the scanning amplitude 0.25) for 300 seconds. Before and after applying this intensive irradiation in the fields of 32 μm × 32 μm in size, the 16-times expanded (128 μm × 128 μm in size, the formal horizontal resolution ~0.25 μm/pixel, the scanning amplitude 1.0) same-centered area of the same sample was additionally scanned during 100 sec using the same pulses. Laser irradiation was simultaneously accompanied by imaging of the same fields of larval tissue.

Half of the irradiated and analyzed tissue samples in each experimental group belonged to larval adipose tissue, other samples were imaginal discs, trachea, salivary gland, and mixed tissues. Each individual group of irradiated tissue samples was obtained from up to ten larvae. Experiments were carried out on several groups of analogous tissue samples according to laser exposure conditions, including several pulse durations, specifically 19 fs, 42 fs and 100 fs. Additionally, after measuring the average power after the objective ranging from 5 mW to 15 mW, the peak intensity was calculated to vary in the range from 1×10^{12} to 16.5×10^{12} W/cm^2 (See Table 4) as calculated. The MIIPS software was used to obtain either transform-limited pulses (19 fs or 42 fs) or linearly chirped pulses (42 fs or 100 fs).

Two-photon imaging of whole-body samples of non-labeled larval tissues were carried out simultaneously with irradiation. Two-photon fluorescence images of the tissues of embedded living larvae were acquired using an inverted Eclipse TE-2000 (Nikon, Japan) microscope equipped for multiphoton imaging with a water-immersion LD C-Apochromat 40×/1.1W Corr Objective (Carl Zeiss, Germany), 85 MHz repetition rate broadband Ti:Sapphire Laser (Kapteyn-Murnane Laboratories, Inc., Boulder, CO) with broadband spectrum centered at 800 nm, a pulse shaper with MIIPS adaptive pulse compression, galvanometric scanning mirrors QuantumDrive-1500 (Nutfield Technology, Inc.), a dichroic mirror, a shortpass emission filter (both from Chroma Technology Corp.) and a PMT detector HC120-05MOD (Hamamatsu, Japan). The average power of the excitation beam was measured with a FieldMaxII-TOP power meter (Coherent, Santa Clara, CA) after the objective. Prior to imaging, pulses were compressed to be close to the transform limit and pulse duration was measured ~19 fs after the objective using the pulse shaper. LabVIEW 7.1 software (National Instruments), which was developed in our lab was used to acquire images, 128 μm × 128 μm in size (the formal horizontal resolution ~0.25 μm/pixel, the scanning amplitude

1.0) and 32 μm x 32 μm (the formal horizontal resolution ~0.063 μm/pixel, the scanning amplitude 0.25). The imaging was conducted simultaneously (in the same procedure) with femtosecond laser irradiation.

In general, 100 one-second frames for each one-section view were averaged and transformed into an 8-bit format to generate each final image using the program ImageJ (National Institute of Mental Health, Bethesda, MD). Adobe Photoshop 12.04 (Adobe Systems Inc.) was then used for further adjustments of the brightness in the final images. Thus, for each imaged/irradiated area of tissue we produced five final images: the original, three intermediate images, and then the final image, each obtained respectively at the scanning amplitude 1.0 (the scanning field 128 μm × 128 μm, the formal resolution ~0.25 μm/pixel) and 0.25 (the scanning field 32 μm × 32 μm, the formal resolution ~0.063 μm/pixel). Amplitude 0.25 provides 16-times more pulses per time in the smaller area. The fluorescence images with satisfactory fluorescent signal and contrast were used for scoring and analysis of photodamage.

5.1.3 Irradiation and imaging of whole living larvae and scoring lethality

Sample chambers made of silicon were created in order to irradiate the larvae. These were made by combining a curing agent and Elastomer Base of Sylgard® 184 Silicone Elastomer Kit (Dow Corning Corp, Midland, MI) in a 1:10 ratio and then thoroughly mixing. This solution was poured over a 35x10 mm Petri dish (Becton Dickinson, Franklin, NJ), containing a metal cylinder with a 1.9 mm diameter and a height of 9.2 mm placed at the center, and allowed to crystallize for 48 hours. The silicone slab was then extracted from the Petri dish using a plastic or wooden stick and the metal cylinder was removed, creating a precise cylindrical channel. A schematic diagram of the chamber is shown in Figure 47.

Experiments were carried out on three groups of larvae, according to laser exposure (short pulses, long pulses, and no irradiation). To expose the groups to the laser pulses, larvae were extracted from the vials in small amounts of media and gently rinsed with distilled water. Using a 7-mL transfer pipette (USA Scientific, Ocala, FL), two of the freshly harvested larvae were then transferred into the silicon chamber laid on a folded piece of Kimwipes® paper (Kimberly-Clark Inc, Roswell, GA). Once transferred, the chamber with the two larvae was placed onto the lid of the Petri dish, and the excess water in the chamber's

channel was drained off with a twisted piece of Kimwipe. The chamber with the larvae was then covered with cover glass No. 1 (Corning Inc, Corning, NY) and used for irradiation under the laser beam. The larvae were irradiated for 10 minutes in the setup shown in Figure 47.

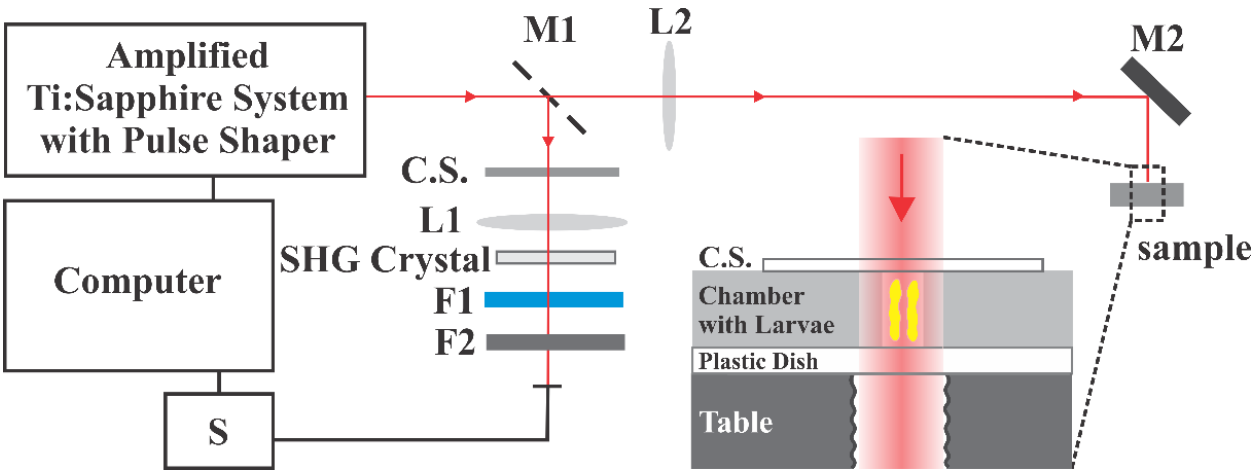

Figure 47. Schematic diagram for irradiating larvae M1 is a flip mirror to change the beam path between the characterization arm and irradiation of the sample; M2 is a mirror used to direct the laser vertically onto the sample and through a hole in the table; L1 and L2 are F=1000 mm lenses; C.S. is a cover slip; F1 is a blue filter; and F2 is a neutral density filter.

To ensure homogeneous irradiation of the entire larva body, the laser parameters were adjusted to mimic the total energy fluence and peak intensity (several PW/m^2) used for typical two-photon fluorescence imaging [8, 133]. Our setup used a regenerative amplified femtosecond laser system with Ti:Sapphire oscillator (Kapteyn-Murnane Laboratories Inc., Boulder, CO) and Spitfire amplifier (Spectra-Physics, Newport corp., Irvine, CA) that was compressed and shaped by a MIIPSBox640 (BioPhotonic Solutions Inc., East Lansing, MI). The laser pulses, centered at 800 nm, with a Gaussian shape spectrum of ~26 nm bandwidth were corrected to produce maximum output power with a 1 kHz repetition rate. The MIIPS software was used to obtain either transform-limited pulses with a FWHM duration of ~37 fs or linearly chirped pulses (1290 fs^2) with a pulse duration of 100 fs. No difference in lethality of *D. melanogaster* was found for positive or negative linear chirp. In order to adjust the energy fluence of the pulses, the beam diameter was changed by moving the focusing lens (See Figure 47, *L2*). In all cases, the beam diameter was

greater than the irradiation chamber, ensuring that the whole of the larva organisms were fully bathed by the laser beam without the need for scanning.

After irradiation, the larvae were gently flushed out of the chamber into a Petri dish with a pipette and transferred into a vial with freshly prepared fly culture media. This procedure was repeated 4 more times (5 runs in total) to obtain 10 larvae irradiated in the same conditions for a given day. The larvae were put in the same vial (which was incubated at a temperature of 21-22ºC) and were counted for survival every other day for a total of 15 days. In order to obtain each individual experimental group of larvae, this irradiation procedure was performed over several days (n=50-70 in 5-7 experiments). Only groups exposed to the laser pulses with high energy fluence resulted in a high early death rate (up to 100%) which reduced the number of surviving larvae (n=20) for the higher energy group. Control experiments for larva that were not irradiated were also performed and scored (n=140, 14 experiments).

Three parameters of lethality were calculated based on the data obtained from these experiments. Total lethality was determined by calculating the difference between the number of larvae before irradiation and the number of flies that developed, divided by the number of larvae before irradiation. In contrast, early (larva) lethality is the number of larvae before irradiation minus the number of pupae that survived, divided by number of larvae before irradiation. This parameter was used to characterize the percentage of deaths during the third instar larvae stage of development that occurred prior to the development of pupae. The delayed deaths of pupae were also calculated by taking the difference between the number of pupae and flies, divided by the number of pupae that survived. This measurement was used to evaluate the deaths that resulted during the pupae stage. To score the relative impact of the early (larva) and delayed (pupa) development stages on total lethality in the population, we calculated the contribution of each stages' lethality (%) to the total lethality observed for each experimental and control group. Averages with standard errors for all parameters were also calculated for each group. Finally, the significance of difference ($P<0.05$) between experimental and control groups was scored using a two-tailed Mann-Whitney U-test.

A digital camera Canon t2i with a Canon MP-E65mm f/2.8 1-5x Macro lens set at 65mm and an attached flash was used to image several of the irradiated larvae in order to document the visible changes

in appearance following irradiation. The larvae were anesthetized with FlyNap (Carolina Biological Supply Company, Burlington, NC) for 10-15 minutes prior to imaging. The images were acquired with an exposure time of 5 milliseconds, an aperture of f/16.0, and an ISO value of 400 approximately 5-20 minutes after irradiation, as well as 3 hours later.

5.1.4 Terminal deoxynucleotidyl transferase dUTP Nick End Labeling (TUNEL) and Image processing for TUNEL-assay

The ability of laser pulses with various durations and intensities to induce apoptosis in larvae was scored by measuring the total brightness of TUNEL-positive cells in salivary glands superficially located in the larva's body. Six or more experiments for each laser treatment condition were done over several days. The laser treatment was performed as described previously, and the larvae were incubated in *Drosophila* fly media (Carolina Biological Supply Company, Burlington, NC) for 3 hours after irradiation. After incubation the salivary glands and imaginal tissues were collected from dissected larvae, and then fixed and stained for DNA fragmentation (TUNEL-assay) according to the protocol for visualization of apoptosis [167, 168] with the modifications given in the appendices.

The images of the fixed, TUNEL-stained salivary glands and imaginal discs were acquired using the same setup and technique described in section 3.2.2. In total, 80 two-photon images for each one-section view were averaged and transformed into 8-bit format to generate each final image using the program ImageJ (National Institute of Mental Health, Bethesda, MD). Adobe Photoshop 12.04 (Adobe Systems Inc.) was then used for further adjustments of the brightness in the final images. Those images containing fluorescent antibody labeling for DNA fragmentation were used for apoptosis analysis. The proportion of TUNEL-positive cells in the images was calculated from a ratio of the area of cells with DNA fragmentation to the total area of the salivary gland in the image by selecting and measuring these regions using ImageJ. The same program allowed us to measure the relative brightness of apoptotic cells. The relative brightness of TUNEL-positive cells in each image was scored as a ratio of their average brightness to the average brightness of the surrounding tissue. To characterize the apoptosis intensity in the samples, we calculated

the product of a portion of the TUNEL-positive cells and their relative brightness. To score the significance of differences between the groups, a two-tailed Mann-Whitney U-test was applied, where a probability of $P<0.05$ was considered as significant. Values of the presented parameters are given as the mean ± standard error of mean.

5.1.5 Calculation of peak intensity of femtosecond NIR laser pulses used for irradiation

Average power Pav and repetition rate f were measured by a power meter and oscilloscope respectively. The repetition rate *f* had a constant value, it was used to calculate the period of laser pulses:

$$T = 1 / f \quad (9)$$

The energy of a single pulse is:

$$E = Pav \times T = Pav / f \quad (10)$$

For Gaussian shaped pulses used for irradiation, a pulse duration *tau* was measured as a full width at half maximum.

The intensity of a laser pulse is power divided by the irradiation area. Therefore for a fixed area, power and intensity have the same Gaussian shaped profile in the time domain, which can be described by the following expression:

$$P(t) = P0 \times \exp(-t^2 / t0^2) \quad (11)$$

where *P0* is a peak power and $t0=tau/(2\sqrt{ln2})$ is a parameter of a Gaussian function.

By integrating the power, we obtained the expression for the pulse energy:

$$E = P0\ t0\ \sqrt{\pi} = 1.064\ P0\ tau \quad (12)$$

The relationship between the pulse energy and average power provides us the calculation of a peak power:

$$P0 = Pav / (1.064\ f\ tau) \quad (13)$$

The intensity profile in the spatial domain can be described as the following:

$$I(x,y) = Ipeak \exp(-8\ (x^2 + y^2)/d^2) \quad (14)$$

where $Ipeak$ is the peak intensity and d is a beam waist.

Since the laser beam was tightly focused into a spot which has size of light diffraction limit, we calculated a value of the beam waist using Abbe's formula:

$$d = \lambda/2NA \quad (15)$$

where λ is the wavelength of the light, NA is numerical aperture of the objective lens. For our conditions: λ = 800 nm, NA = 1.1, the beam waist d = 364nm.

By integrating the intensity over the pulse area, we obtain the relationship between peak intensity and peak power:

$$Ipeak = 8\ P0\ /\ (\pi\ d^2) \quad (16)$$

$$Ipeak = 8\ Pav\ /\ (1.064\ f\ tau\ \pi\ d^2) \quad (17)$$

Values of the peak intensity calculated for different conditions of pulsed irradiation are presented in Table 4.

Table 4. Calculated peak intensities of femtosecond pulses with different pulse duration and average power during the NLOM imaging and irradiation of *D. Melanogaster* larvae.

Average power Pav, mW	Peak intensity $Ipeak$, *TW/cm²*		
	19 fs	42 fs	100 fs
5	5.5	2.5	1.05
15	16.5	7.5	3.15

5.1.6 Lethality as a function of *n*-photon signal

Lethality as a function of energy fluence per pulse and pulse duration can be described by the dose-response relationship [169] as modified for our case:

$$L(E_p, \tau) = C + \frac{1-C}{1+10^{-\frac{E_p - E_m(\tau)}{E_s(\tau)}}} \quad (18)$$

where L is the lethality fraction, E_p is the energy fluence per pulse (J/m^2), τ is the pulse duration, C is the lethality fraction of the control group, E_m is the energy dose required to kill half the population proportional to the equation, $((1-C)/2 + C)$, and E_s is the energy sensitivity characteristic of the organism.

The normalized non-linear (average order n) signal, S, can be expressed as,

$$S^{(n)} = {E_p}^n/\tau^{n-1} \quad (19)$$

The lethality proportional signal can be derived by combining Equations 18 and 19. When we limit the equation to two-photon induced emission, we obtain the relation,

$$L(S^{(2)},\tau) = C + \frac{1-C}{1+10^{-\frac{\sqrt{S^{(2)}}\times\tau - E_m(\tau)}{E_S(\tau)}}} \quad (20)$$

In the intermediate region of the dose-response curve, we assume an *l*-order process is the primary cause of death. By repeating the experiment for two pulse durations, we obtain:

$${E_1}^l/{\tau_1}^{l-1} = {E_2}^l/{\tau_2}^{l-1} \quad (21)$$

We solve for *l* in this equation by taking the natural logarithm to obtain:

$$l = \frac{\ln(\tau_2/\tau_1)}{\ln\left(\frac{E_1\times\tau_2}{E_2\times\tau_1}\right)} \quad (22)$$

Using Equations 20 and 22 (calculations are given in appendix III):

$$S^{(n)}(\tau) = \big(E(\tau)\big)^n/\tau^{n-1} = \left(\frac{E_1}{\tau_1^{\frac{l-1}{l}}}\right)^n/\tau^{\frac{n}{l}-1} \quad (23)$$

5.2 Results

5.2.1 Effects of irradiation of live larvae with 15 mW average power NIR laser pulses of 19 fs, 42 fs and 100 fs duration

Intensive irradiation using transform-limited NIR pulses with a duration of 19 fs and a peak power of 9.2 kW at a scanning amplitude of 0.25 induced photodamage in all samples of irradiated living tissues (100%, *N*=16). The damage was observed as a bubble formation, resulting in the ruptures of cellular plasma membranes ("merging cells"), and resulted in partial or complete ablation of the tissue in the irradiated area (Figure 48 B-E).

The photodamage was consequently accompanied by two types of endogenous fluorescence enhancements. The first intracellular photoenhancement demonstrated a characteristic "mitochondria-co-localized" pattern, which was observed on a periphery of the cell's cytoplasm until the plasma membrane was destroyed by irradiation. The intracellular photoenhancement is replaced by the enhancement of

fluorescence in the destroyed tissues (post-damage photoenhancement). Signs of cellular damage appeared in the living tissue within a few seconds after starting the laser irradiation (median: 6 sec, mean ± SD: 8±8 sec). The zone of photodamage and post-damage photoenhancement was found to spread out into the surrounding non-destroyed tissues, which means that this fluorescence could emanate from post-damage cell lysates. Only one sample of the adipose tissue showed the photodamage of cellular membranes without significant photoenhancement. Two samples showed homogeneous (without a characteristic pattern) photoenhancement in cytoplasms of the cells with undamaged plasma membranes. This intracellular homogeneous photoenhancement in the cells with undamaged plasma membranes is a sign of destruction of the intracellular membranes (of organelles and compartments). The use of the same pulses at the scanning amplitude 1.0, in which the dwell time is 16 times lower than at scanning amplitude 0.25, dramatically reduced photodamage in irradiated living tissues (Figure 48A).

The longer transform-limited and chirped (chirp: ~258 fs^2) NIR pulses with the same 42 fs pulse duration, 15 mW average power, and 4.2 kW peak power scanned with amplitude 0.25 also produced bubble formation, which was accompanied by subcellular and post-damage photoenhancement in all samples (100%, n=21). However, the area and intensity of photodamage were smaller and did not spread beyond the area of irradiation like in the previous experiments (Figure 48 G-K and M-P). Irradiation with 42 fs pulses required significantly more time (median: 99 sec, mean ± SD: 107±65sec) to induce bubble formation in the samples than the analogous treatment with 19 fs pulses ($P<0.001$, two-tailed U-test). The subgroups of samples treated with the transform-limited (median: 99sec, mean ± SD: 102 ± 70sec) and chirped pulses (median: 104 sec, mean ± SD: 115 ± 59sec) did not differ by this parameter ($P>0.05$, two-tailed U-test).

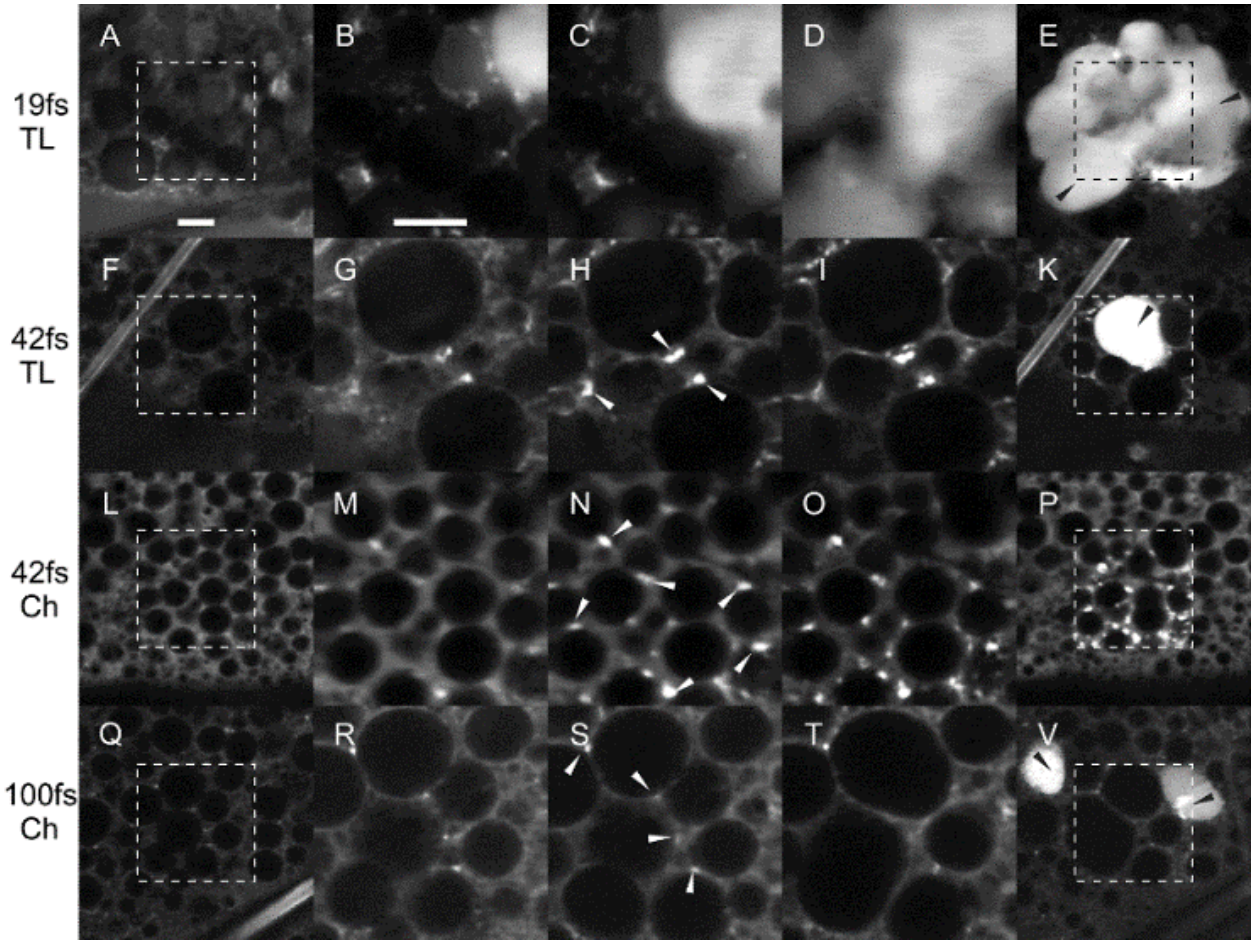

Figure 48. Fluorescence images of living tissues of *Drosophila* larvae, obtained with the use of femtosecond NIR pulses of different pulse duration and same average power (15 mW). The panels represent the images of 4 samples. Each image is produced by summation of 100 one-second frames of the same optical section of the sample. Each row represents a sequence of images, obtained with use of pulses of different durations. The first and last columns consist of images received in the beginning (the panels A, F, L and Q) and the end (E, K, P and V) of imaging experiments at scanning amplitude 1.0. The middle three columns represent a sequence of three images (for each sample), received at an amplitude of 0.25 which provides 16-times more pulses per time in the smaller area of irradiation scanned during 300 seconds, centered as the images obtained at amplitude 1.0. Each image of columns is produced by summation of 100 one-second frames of the same optical section of the sample. Photoenhancement, accompanied by photodamage in the irradiated tissues (indicated by black arrowheads in panels E, K and V), usually spreads over the central area (scanned at amplitude 0.25). Intracellular photoenhancement without visible damage of cellular membranes (indicated by white arrowheads in the panels C, G, N and S) resembles the localization pattern of mitochondria in the cells. Scale bar: 10 μm.

By scoring photodamage in the samples (N=32) with a criterion based on ruptured plasma membranes ("merging cells"), we found that 75% were affected. The levels of photodamage in the subgroups of the samples treated with the transform-limited (N=13, Figure 48 G-K) and chirped pulses (N=19, Figure 48 M-P) were comparable: 77% and 74%, respectively. During irradiation of the rest of the samples, the cells acquired the intracellular photoenhancement with characteristic patterns on the periphery of the cytoplasm. When the samples were irradiated with the same pulses at a scanning amplitude of 1.0 (the dwell time is 16 times lower than at scanning amplitude 0.25), we observed stable high-contrast fluorescent images without visible mechanical photodamage (Figure 48 F,L).

Irradiation with 100 fs chirped (chirp: ~669 fs^2) NIR laser pulses with an average power of 15 mW (peak power ~1.7 kW) at the scanning amplitude of 0.25 demonstrated an even lower frequency of photodamage in the living samples: 4 of 7 (~57%) of the samples available for analysis of the bubble formation experienced bubbling; while 6 of 17 (~35%) of the samples were found to be positive for the presence of ruptured plasma membranes (Figure 48 R-V). The time for the manifestation of photodamage in the living tissue (median: 226 sec, mean ± SD: 224±36 sec) with 100 fs pulses was significantly longer ($P<0.01$, two-tailed U-test) than for 42 fs pulsed irradiation, and dramatically extended ($P<0.001$, two-tailed U-test) compared to 19 fs pulses. The intracellular and post-damage photoenhancements were found to be much less intensive and less stable than in the analogous samples irradiated with 42 fs pulses. In some samples, the limited post-damage photoenhancement was found migrating through extracellular space of the cells with non-damaged plasma membranes. The samples irradiated with these pulses at the scanning amplitude of 1.0 (the dwell time is 16 times lower than at the scanning amplitude 0.25) provided stable contrast images without visible photodamage (Figure 48Q).

5.2.2 Effects of irradiation of live larvae with femtosecond NIR laser pulses with average power 5 mW

Two-photon imaging of larval tissues with ~5 mW femtosecond NIR laser pulses with durations of 19 fs and 42 fs and a peak power of ~3.0 kW and ~1.4 kW respectively during 100-300 seconds produced stable and high-contrast fluorescence images without visible photodamage on the level of the cellular pattern (Figure 49). The images produced with the shorter pulses were brighter and of higher contrast in most cases. A weak intracellular photoenhancement could be found in the samples. Imaging with 100 fs NIR laser pulses of the same average power 5 mW (peak power ~0.6 kW) did not provide images with satisfactory signal and contrast under our experimental conditions (not shown).

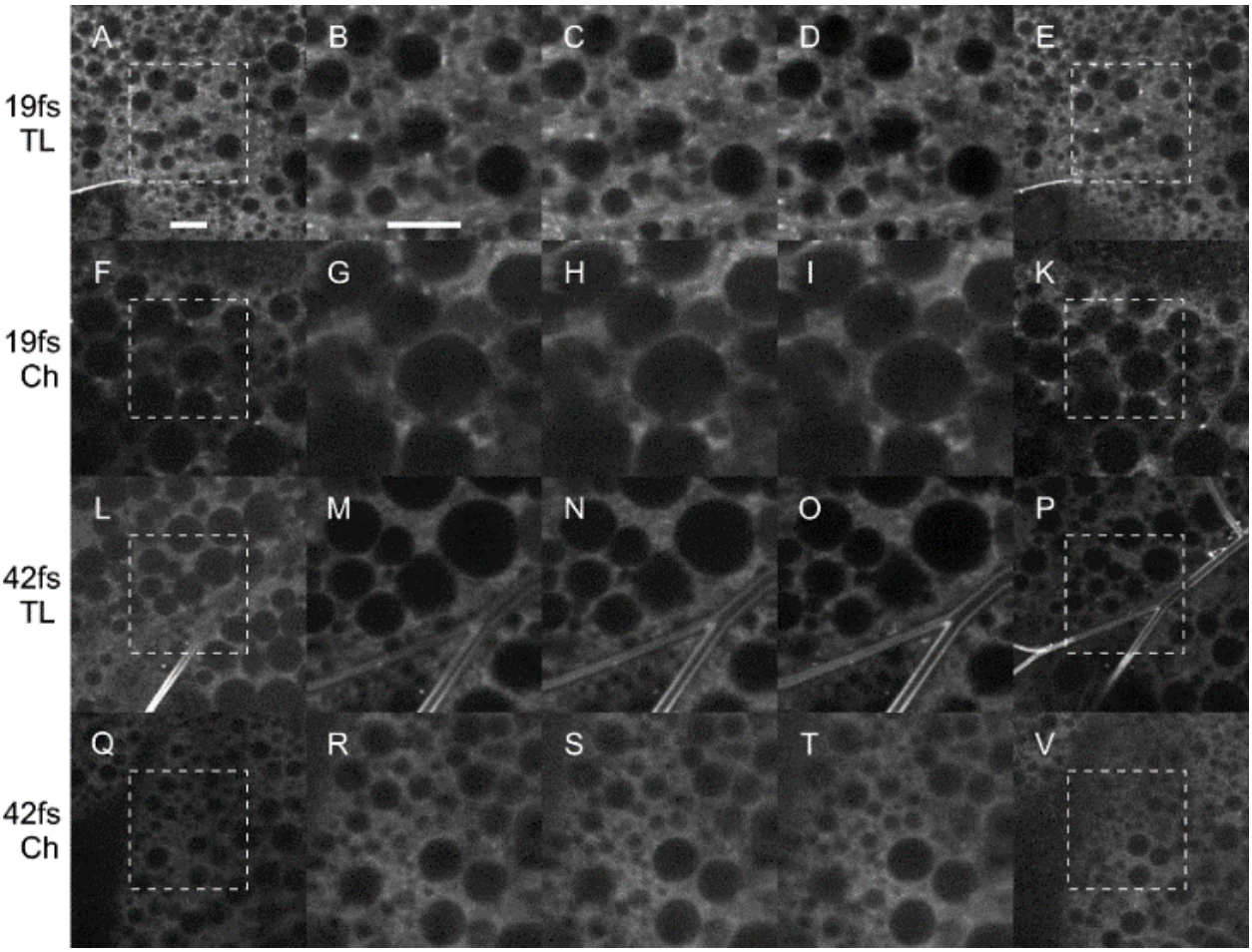

Figure 49. Fluorescence images of living tissues of *Drosophila* larvae, obtained with the use of 5 mW femtosecond pulses with 19 fs and 42 fs pulse duration (peak power ~3.0 kW and ~1.4 kW respectively). Basic conventions are essentially the same as in previous figures. Scale bar: 10 μm.

5.2.3 Observation of necrotic changes in irradiated tissues

At high energy fluence (115 J/m²) of irradiation pulses, necrotic changes in the irradiated larvae appeared the same or next day, in addition to swelling of the body, dark brown/black spots alongside the larva, dark "lines" inside the body on nerves and vessels, and a partial darkening of the trachea and surrounding tissues (Figure 50 left column). The maximum life span of necrotic larvae was three days, in which time necrotic spots became darker and wider. Two photographs of another larva irradiated for a duration of 10 min with 100 fs NIR pulses and with an energy fluence of 115 J/m² presented in Figure 50, right column. The top image was acquired 18 min after treatment, the bottom - 3 hours after irradiation. Several small necrotic (brown and black) spots, which appeared after laser treatment and became more visible with time, are indicated by white arrows. The irradiated larva also lost transparence.

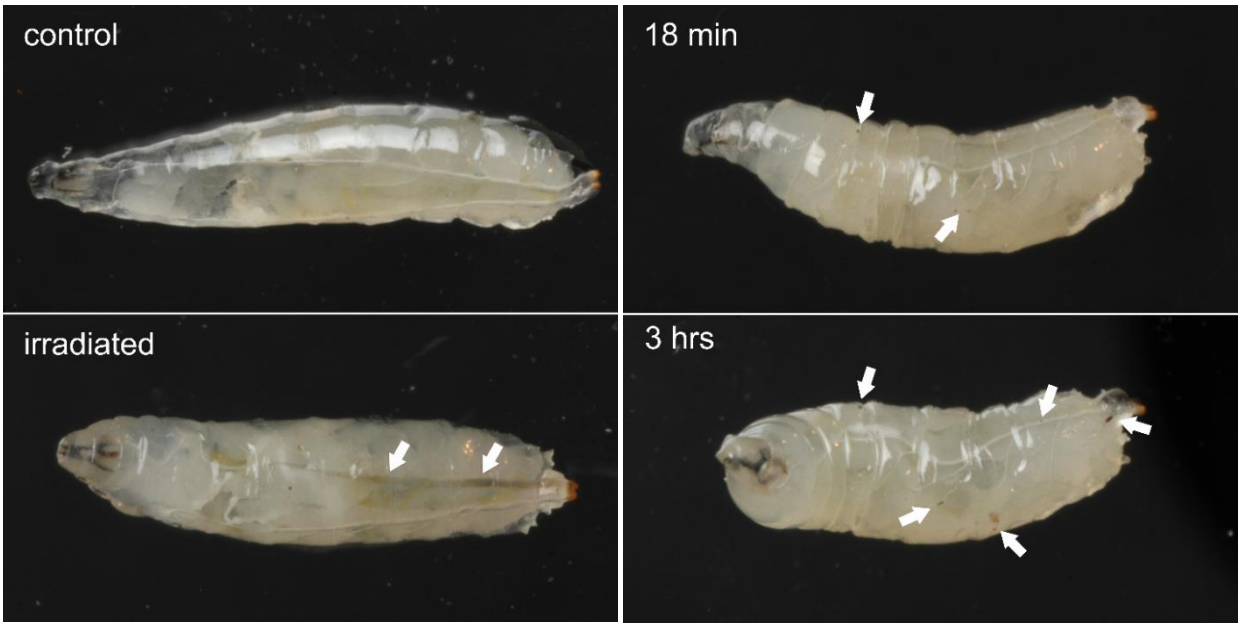

Figure 50. An example of necrotic changes (tracheal darkening) induced by femtosecond laser pulses in *Drosophila* larva (left column). Necrotic spots (right column) induced by femtosecond laser pulses in *Drosophila* larva.

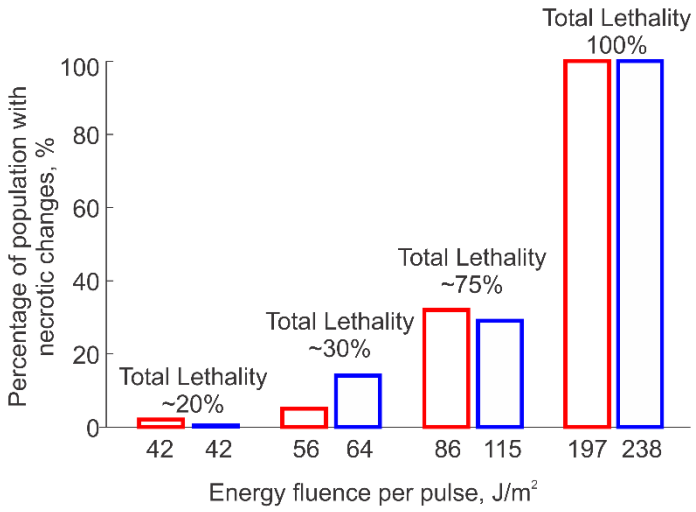

Figure 51. Percentage of larvae population with necrotic changes after irradiation with 37 fs (red scale bars) and 100 fs (blue scale bars) pulses.

Figure 51 reflects a comparison between 37 and 100 fs pulses in their ability to induce necrosis. 60-70 larvae were used for each group. No necrotic effects were seen in the controls or the larvae irradiated with NIR femtosecond pulses with energy fluence of ~27 J/m² (37 fs). Comparison between the lethality in population and the number of larvae exhibiting necrotic changes suggests that the level of necrosis had higher growth with increasing energy fluence for shorter pulses. Abnormalities of the necrotic larva's mobility that prevented them from moving and feeding indicates that the damage may have affected the central and peripheral nervous system and/or the neuromuscular apparatus in these larvae. This damage is considered necrotic due to the nature of the visible changes inside of the affected larvae, which accompanied impaired mobility and unusual behavior.

5.2.4 Apoptosis in populations of irradiated and control larvae

The ability of femtosecond NIR laser pulses to induce apoptosis was scored by measuring a portion of TUNEL-positive salivary gland cells' relative brightness in larvae irradiated with 42 J/m² (37 fs and 100 fs pulses), 86 J/m² (37 fs pulses) and 115 J/m² (100 fs pulses). The tissues were imaged utilizing multiphoton microscopy. A representative example microphotographs, used for the measurements, are shown in Figure 52, together with a plot of the results.

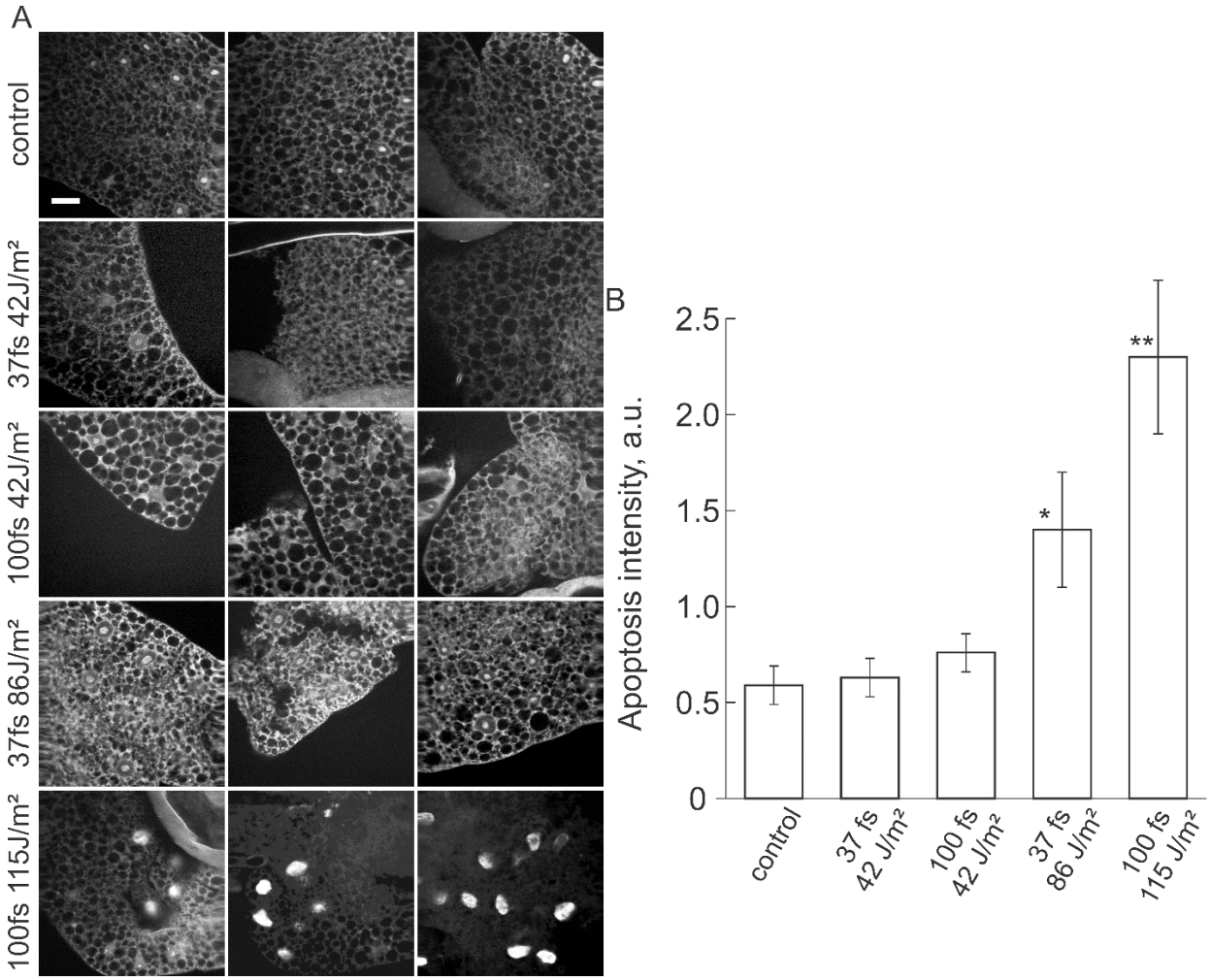

Figure 52. TUNEL-analysis of irradiated and control larvae. (A) Microphotographs of the salivary glands from *Drosophila* larvae exposed for 10 min to laser femtosecond pulses (37 and 100 fs) and various energy fluence (42, 86 and 115 J/m²). Irradiated larvae were allowed to develop an apoptotic response over the course of 3 hours and were then dissected to obtain salivary glands, which were processed for the TUNEL-assay. Control larvae were treated in the same manner but were not exposed to any laser pulses. Microphotographs were obtained using the multiphoton imaging system, which provided SHG-signal from unstained regions of imaged tissues (mostly cellular membranes) as well as a TUNEL-specific signal from positive cells (cytoplasm and nuclei). Each row consists of 3 representative single-section images of salivary glands from larvae treated under the same conditions. The greatest intensity of TUNEL-staining was observed in cells obtained from larvae irradiated with 100fs 115 J/m² pulses. In samples from larvae irradiated with 37 and 100fs pulses with energy fluence of 42 J/m², the apoptosis intensity, which is a result of multiplication of the portion of TUNEL-positive cells by their relative brightness, was similar to the level in the control samples. White scale bar is 20 μm. (B) Bars represent apoptotic intensities in the groups of control and irradiated larvae. Values are mean ± SE of at least six independent experiments. The P values for experimental groups were obtained by comparison with the control group: * $P<0.01$, ** - $P<0.0001$ (two-tailed U-Test).

When the non-irradiated (control) samples (n=17) were analyzed, we found 7.9 ± 0.6% of cells to be apoptotic with a total fluorescence intensity of 0.59±0.10 a.u. Larvae treated with laser pulses of relatively low energies (~42 J/m²) had similar levels of TUNEL-stained cells: 8.8±1.0% (37 fs) and 9.7±0.7% (100 fs) with a total brightness of TUNEL-staining of 0.63±0.10 a.u. and 0.76±0.10 a.u., respectively. These numbers did not differ significantly from the control larvae in a two-tailed U-test ($P>0.05$). Irradiation with 37 fs and 100 fs pulses with higher energy fluence of 86 J/m² and 115 J/m², respectively, increased the number of apoptotic cells in the salivary glands by 13.5±0.9% and 14.1±1.4%, respectively, ($P<0.0001$ for both) with a brightness intensity from the stain (1.4±0.3 a.u., $P<0.01$ and 2.30±0.4 a.u., $P<0.0001$, two-tailed U-test), a value significantly greater than observed in the control larvae.

5.2.5 Quantitative analysis of lethality as a function of energy fluence

The use of mathematical modeling allowed us to analyze the dependence of total lethality in populations of larvae irradiated with shorter and longer femtosecond pulses as a function of energy fluence (Figure 53).

Experimental data are fit using the dose-response function as a given in Equation 18. For both curves, the adjusted R-squared coefficients are close to 1.0. This shows that the dose-response function is adequate for modeling the experimental data on the dependence of lethality on energy fluence. Three regions can be identified on the curves. In the first region (energy density < 50 J/m²), the experimentally observed total lethality after irradiation (<20%) is not significantly higher than that observed in the control. In the second region (50-120 J/m²), the deaths increase from 27-30% to 70-73%, and in the third region (>120 J/m²) lethality approaches 95-100%. We note that the two functions describing the dependence of lethality on the energy fluence for shorter and longer femtosecond pulses are very similar. The value for E_m, or energy required to kill half of the population, is (76±1.5) J/m^2 and (94±2.1) J/m^2 for shorter and longer pulses respectively.

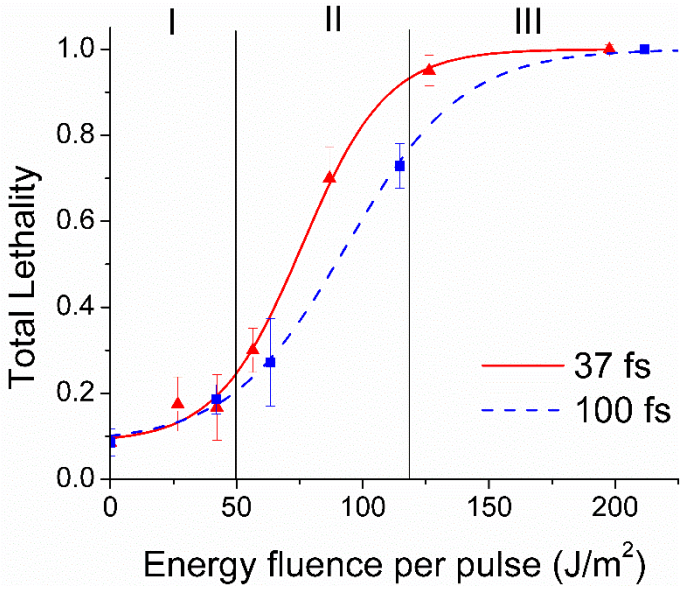

Figure 53. Total lethality as a function of energy fluence per pulse for 37 fs and 100 fs pulses represented by a dose-response relationship.

The energy parameters used for laser irradiation are chosen to be as similar as possible to conditions used during typical multiphoton imaging. To estimate the possible photodamage during multiphoton imaging due to illumination with femtosecond pulses of different duration, we compare the measured photodamage, described by an observed lethality, with the calculated two-photon signal resulting from the same energy fluence. As seen in Figure 53, irradiation with shorter (~37 fs) and longer (~100 fs) pulses of the same energy fluence causes different levels of photodamage. The same photodamage results from treatment with shorter or longer pulses of slightly different levels of energy (lower and higher respectively). However, a much higher two-photon signal for imaging is achieved by illumination with shorter pulses in comparison to longer pulses of the same or higher energy fluence.

The difference between longer and shorter pulses in terms of expected TPEF signal and lethality becomes clearer by plotting lethality versus two-photon signal, as shown in Figure 54 (Left). It shows that for a given two-photon signal, the shorter ~37 fs pulses cause less damage (lethality) than the longer ~100 fs pulses. This indicates that shorter pulses are a better choice for use in multiphoton imaging than longer pulses. This conclusion is based on the range of energies studied here, the wavelength of the excitation pulses (800 nm), and the fact that whole organisms were irradiated.

Relying on our experimental data of laser-induced lethality in Region II (Figure 53) and using Equation 22, we estimated the nonlinearity order of the photodamage process. Our calculations were based both on experimental data points and dose-response relationship, which parameters were obtained from fitting the experimental data into theoretical model. The average calculated non-linearity coefficient, *l*, was 1.28 ± 0.05, while a calculation based on our experimental data without fitting gave *l*=1.19 ± 0.2. Values of *l*<2 imply that non-linearity of photodamage process is lower than the nonlinearity of an optical signal, therefore shorter pulses are better in terms of producing higher two-photon optical signal as SHG and TPEF with lower photodamaging effect, while values of *l*>2 would imply that longer pulses are preferable for two-photon microscopy. For third-harmonic generation or three photon excitation microscopy, shorter pulses are always better, given the higher nonlinearity of the excitation process to induce the optical signal.

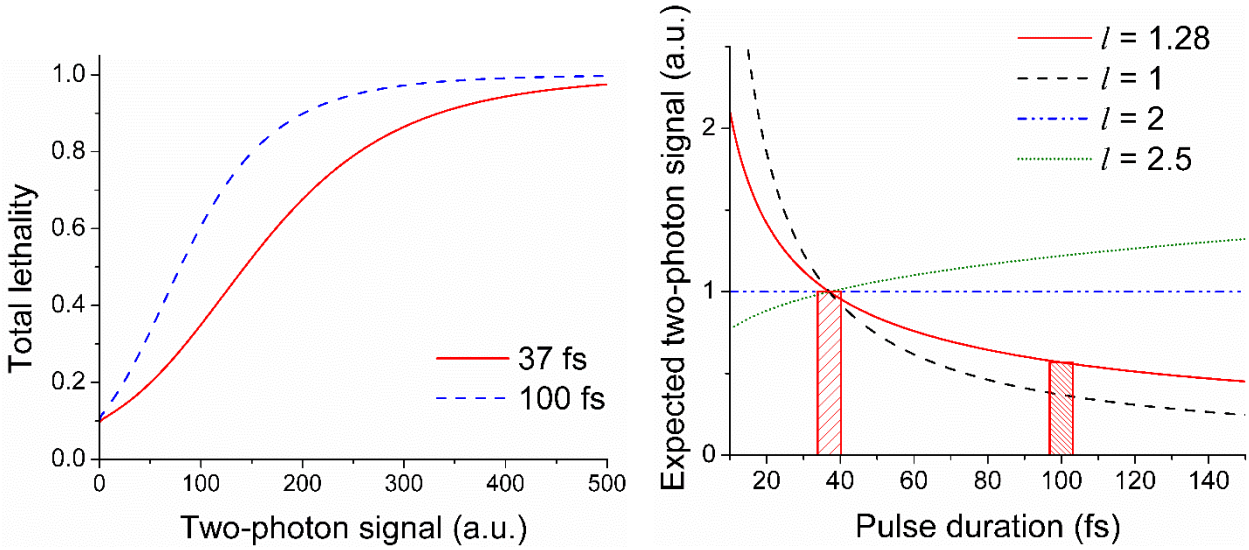

Figure 54. Theoretical model based on experimental lethality curves shows the total lethality as a function of theoretical two photon signal from 37 and 100 fs pulses (left); two-photon signal as a function of pulse duration for a total lethality equal to 54% (right). Two vertical bars correspond to our observed experimental results.

Using Equation 23, we estimated two-photon signals for a constant level of total lethality (54%) with different possible orders of photodamage processes: 1, 1.28, 2 and 2.5 (Figure 54 Right). As previously stated, *l* =1.28 is closest to the order found from our experimental data on lethality within region II. In the same graph, several multiphoton-photon processes of photodamage are depicted with *l* =1; *l*=2 and *l* =2.5.

As seen in Figure 54 Right, if photodamage has an l=2 order, then for a fixed photodamage level of 54%, the expected two-photon signal becomes independent of pulse duration. This occurs because it is necessary to adjust the pulse fluence in order to maintain the fixed photodamage level. On the other hand, for non-linear processes with l<2, the two-photon signal is inversely proportional to the pulse duration. This indicates that shorter femtosecond pulses, in comparison with longer pulses, provide greater signal for a fixed acceptable level of photodamage. The situation is reversed if the damaging mechanism is highly non-linear, for example three-photon DNA damage. For l >2 processes, longer pulses create more signal than shorter pulses based on a fixed acceptable level of photodamage.

5.3 Discussion and conclusion

Observation of qualitatively and quantitatively different effects of irradiation with femtosecond NIR laser pulses of different durations but the same average power of 15 mW (Figure 48) provides the evidence that the laser-induced damage, observed within the scored range of peak powers, is the nonlinear process.

Because pulsed irradiation at 5 mW did not produce any visible ablation, bubble formation, or tissue disruption in our experiments (Figure 49), we are not able to confirm the nonlinearity of a photodamage for these irradiation conditions, relying only on mechanical photodamage. However, considering the photoenhancement as an indication of femtosecond photodamage [170, 171], and observing the different degrees of photoenhancement (Figure 49) we conclude the nonlinear nature of photodamage, produced by femtosecond pulses of different durations at the same average power of 5 mW.

Tissue ablation is generally considered to be a result of multiphoton ionization and associated with plasma formation [153, 154, 159, 161, 162, 166]. Calculation of peak powers of femtosecond laser pulses shows that the tissue ablation in whole undissected unlabeled living organism was observed within the range of peak intensities (~10^{12}-10^{13} W/cm^2) predicted by the theoretical models [158, 159, 163]. This confirms that femtosecond pulses may produce multiphoton ionization (~10^{12} W/cm^2) and avalanche ionization (~10^{13} W/cm^2) *in vivo*, and supports our conclusion that the femtosecond laser-induced photodamage *in vivo* is a nonlinear process.

The observation of increased fluorescence (photoenhancement) experimentally in this study and previous studies [170-172] reflects a reduction from non-fluorescent NAD^+ to fluorescent NADH [119, 171, 173, 174]. A pattern of so called "punctuated fluorescence", observed in the intravital experiments and in previous experiments [130, 156, 175], confirms that fluorescent organelles irradiated with femtosecond pulses *in vivo* are likely mitochondria [130], and should be also considered in the course of developing safer intravital noninvasive imaging.

This study uses *D. melanogaster* as a model organism to estimate the photodamage caused by femtosecond NIR laser pulses with the energy fluence ranging from ~20 to ~240 J/m². We found that the observed photodamage, scored as the total percentage of deaths in the larva populations induced by laser radiation, can be fit to a sigmoid-shape, 3-region curve with a dose-response relationship as a function of energy fluence (Figure 53).

We consider the necrotic changes accompanying the early deaths in our experiments to be the result of primary and secondary necrotic processes induced by thermal injury from the femtosecond NIR laser irradiation. Counting the number of necrotized larvae in the population showed that the contribution of necrosis had positive correlation with survival. In the middle region of applied energy fluence (50-120 J/m²), 37 fs pulses produced more larvae with visible necrosis than 100 fs pulses (Figure 53). This difference disappeared when the total number of deaths, as well as the level of necrosis in the population, approached terminal levels (~100%). In contrast, the delayed deaths of the pupa are considered to be the result of secondary necrotic processes that follow the thermal or mechanical injuries triggered by the laser treatment. Based on the nature of secondary necrosis, the possible mechanism of delayed death can be due to induction of acute inflammation and immune response to denatured proteins in necrotic tissue. This would be a result of the overproduction of inflammatory mediators, which cause toxic effects on the body. These delayed deaths are less likely to be associated with DNA damage after the laser treatment, as non-reparable DNA damage in the genome should prevent survival of the irradiated larvae and continuation to the next stage in development.

The use of the TUNEL-assay for scoring apoptosis in the cells of salivary glands from larvae exposed to the laser provides evidence that pulses within our evaluated range of duration and energy may induce apoptosis in the irradiated tissues. We found a significant increase in the number of apoptotic cells in those larvae irradiated with energy fluences near ~100 J/m², while the observed level of apoptosis was not significantly different from that of the control when the applied energy fluence was <50 J/m².

Comparison between the percentage of deaths and the number of larva having necrotic changes provides evidence as to the sensitivity and accuracy of the two methods performed. It was determined that scoring the necrosis by counting the necrotic larvae in population was less effective than scoring the number of deaths in each stage. It is possible that the level of necrosis was underestimated when analyzing the larva, especially when low energy fluence pulses were used for irradiation, because of the low sensitivity of visual inspection method for necrotic changes at early stage. When relying on the approximate scoring of necrosis for 115 J/m² (100 fs) and 86 J/m² (37 fs) pulses, we estimate that the contribution of necrosis to the total number of deaths in the population to be as much as ~40% and 46% respectively. However, again, this level could be significantly underestimated. To improve this analysis, the use of a more sensitive cellular assay for detection, such as nuclear staining of high-mobility group box 1 (HMGB1) [176] would be suitable and more accurate for future experiments in addition to visual inspection for necrotic changes.

Another aspect of our study is the relationship between necrosis and apoptosis in damaged tissues. Using mammalian models of acute dermal burn injury, it has been found that thermal damage generally inhibits apoptosis [176, 177], while the intensity of necrosis increases [176]. Because inflammation and immune response; apoptosis and necrosis are being inextricably linked with their effectors modulating other processes [140], extrapolation of this mechanism on invertebrate organisms is possible. We suggest that this effect could exist in the irradiated larvae. Indeed, just a small increase in the number of apoptotic cells in our experiments could be the result of such inhibition. It should be considered that the apoptosis scored here could be partially caused by the primary necrotic process induced by the irradiation. However, due to the activity of mediators seen during the development of primary and secondary necrosis, we assume that

the presence of secondary apoptosis in the irradiated tissues to be a potential contributor of the process leading to the delayed deaths.

Combining our experimental data with mathematical modeling showed evidence that for a given two-photon signal, the lethality as a photodamage effect with 100 fs pulses is higher than that from 37 fs pulses. Moreover, calculations based on the dose-response fitting of experimental data and the comparison of experimental points gave similar levels of average non-linearity values to be ~1.2-1.3. This shows that damage that caused death in the population has a primarily linear character. This observation implies that most of the damage is thermal (l=1) with a small contribution of a nonlinear (possible l=2 or 3) photodamage. Our result seemingly contradict previously obtained data concerning the damaging effects of femtosecond pulses [115]. Previous data estimates that the damage caused by femtosecond pulses is the result of a 2.5 order process. This difference is likely associated with using different biological models, parameters, and observation times to study the effects of photodamage. Our results are in agreement with the study by Rockwell's group on the effects of laser pulse duration on damaging the retina, which were instrumental in the determination of laser safety standards [152].

Chapter 6 Summary and Outlook

Although invasive applications of nonlinear optical effects of high intensity lasers—cutting, welding and ablation—have created a breakthrough in medicine, non-invasive nonlinear optical microscopy has not been approved for use in clinics yet. The optimization of femtosecond pulses through adaptive spatio-temporal shaping for excitation of nonlinear signals in NLOM has been demonstrated. This allows the use of lower average power and, therefore, less thermal deposition in highly absorptive tissues.

The wide tunability of the two-photon excitation wavelength, fast switching rate between the selective excitation, and low photodamage (due to the low average power of the laser beam) enables the potential application of multiplexed selective excitation with quadrature detection for *in vivo* dynamic imaging in biological samples.

The results of my research demonstrate the potential of fiber-based and solid state ultrabroadband laser systems to address a key performance limitation related to NLOM technology, while simultaneously providing low barrier-to-access alternatives to current Ti:Sapphire sources that could help accelerate the movement of NLOM into clinical practice.

6.1 Applications of Yb-fiber lasers for depth-resolved skin imaging

The direct side-by-side comparison of a sub-50 fs, 1060 nm Yb-fiber oscillator to an integrated pulse shaper with a >100 fs, 800 nm Ti:Sapphire laser during multimodal imaging of human skin demonstrates the following benefits of using an Yb-fiber laser: shorter pulse duration with longer excitation wavelength; increased penetration depth by 100 μm in SHG imaging; and the use of two times less average power.

6.2 Imaging of RBCs

We have investigated TPEF, THG, and 3PEF for label-free non-invasive RBC imaging. Unlike conventional laser microscopy systems (>100 fs), the laser systems employed here produce very short pulses (15 fs for the Ti:Sapphire and 45 fs for the Yb-fiber lasers). Therefore, these short-pulse sources deposit less thermal energy and reduce photothermal damage to the RBCs. A TPEF signal increases as the

inverse of pulse duration; whereas, THG and 3PEF signals increase as the inverse of the pulse duration squared. Following successful TPEF imaging of RBCs, we explored the source of the fluorescence and concluded it originated from hemoglobin; this conclusion was based on fluorescence spectra and fluorescence lifetimes, as well as linear and transient absorption data. The images are sufficiently detailed to assess morphological anomalies of RBCs non-destructively without breaching sterility using commercially available compact femtosecond laser oscillators.

Multi-photon microscopy modalities such as THG, TPEF, and 3PEF can be used for non-invasive imaging of blood cells through a storage bag. Moreover, we demonstrated that THG imaging provided the best resolution and image sensitivity for noninvasive imaging of stored RBCs without photodamage. We conclude that using compact and reliable ultrafast laser oscillators may lead to improvements in non-invasive blood analysis, including point-of-care assessment of RBC morphology.

6.3 Laser induced damage studies based on *D. Melanogaster* larvae

The maximization of a nonlinear signal ultimately creates a need to use highly intense laser pulses. Conventionally, the average laser power at the focus of a high NA objective does not exceed 50 mW; however, the intensity of the laser field may go up to a tenth of TW/cm^2 because of spatial focusing and temporal compression. Thermal deposition and nonlinear photodamage may occur at such a high intensity.

The whole-organism model of photodamage that we used has several advantages over cell culture models. One advantage is that it allows us to evaluate the effects of laser pulses *in vivo*, which more closely reproduces the irradiation effects of imaging living tissues. This aspect is important as nonlinear optical imaging applications are being developed for *in vivo* diagnosis in humans. In addition, the cell culture model presents gross differences compared to living tissues or entire organisms. Another difference between our study and others in the literature is the time scale of irradiation; while our experiments ran for 10 min, experiments performed in previous studies were limited to 10-40 μs. It is important to note that the laser parameters utilized in this study are similar to those used in TPEF. To check for the possibility of latent tissue damage, we tracked lethality for 14 days after irradiation to give enough time for the

development of damage that was not immediately evident following laser exposure. Our conclusion regarding the near linearity of photodamage has been indirectly confirmed by another study carried out on skin tissue [84]. Masters and co-workers showed that decreasing average laser power while maintaining the same peak power decreases thermal mechanical damage to skin tissue.

Relying on this information, we consider the linearity of the process observed in our model within the middle region of the dose-dependence curve a result of cumulative photodamage at the level of the whole organism. This result does not, however, eliminate multi-photonic photodamage mechanisms created by femtosecond pulses. Our current work provides evidence that for a given two-photon signal intensity, the lethality provided by irradiation with 100 fs pulses is higher than the lethality induced by treatment with 37 fs pulses. This means that the use of shorter femtosecond pulses in comparison with longer pulses is safer.

APPENDICES

APPENDIX-I Wavelength and intensity calibration of a 16-channel PMT detector

Wavelength-resolved fluorescence lifetime measurements provide chemically specific spectroscopic information, which was used in Chapter 4 for identifying the source of fluorescence in RBCs by comparing spectrally resolved lifetime decays with known biologically relevant fluorophores. The spectroscopical data relies on correct measurements of wavelength and arrival time of photons, emitted from the studied sample. While the manufacturer guarantees the precision and accuracy of the measured time of arrival, the parameters of the spectral resolution and sensitivity require a separate calibration procedure due to the requirement that the instrument be flexible for the different conditions of the experiment.

The angle of the grating inside the TCSPC system's polychromator is adjustable in order to adjust the spectral window of interest (~200 nm) in the 350 nm to 800 nm range. In such a configuration, a 16-channel PMT detector (PML-16-C, Becker & Hickl GmbH, Berlin, Germany) provides 12.5 nm/channel spectral resolution. However, with different quantum efficiency and sensitivity for the wavelength of an incoming photon, it introduces an error in the signal intensity for each channel of PMT detector. This error also affects the effective bandwidth of each channel, leading to a negative quadratic term in the wavelength to the channel calibration.

In order to perform a channel-to-wavelength calibration of the multichannel PMT, the TPEF spectra of different color fluorescent plates (Chroma, USA) (Figure 55, left) and SHG were obtained using a factory calibrated spectrometer QE6500 (Ocean Optics Inc., FL, USA), as well as a multichannel PMT system. For each of the obtained spectrums, the PMT channel number and the wavelength of the peak emission was recorded. By plotting the wavelength of the peak versus the PMT channel number and fitting those data points with a second order polynomial, the calibration was obtained (Figure 55, right).

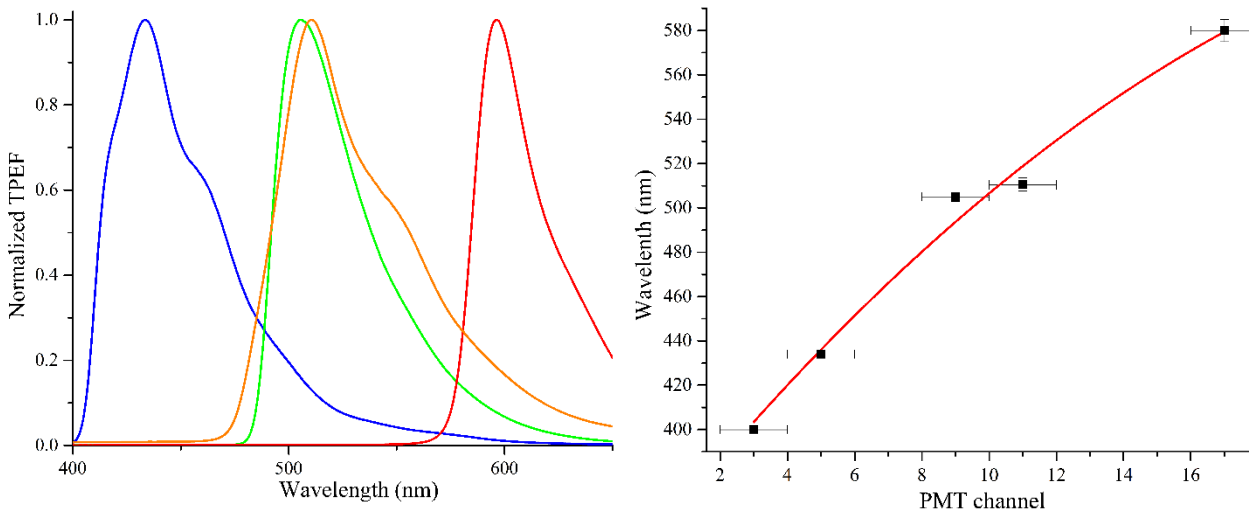

Figure 55. Left panel: TPEF spectra of fluorescent plates, obtained with factory-calibrated Ocean Optics QE6500 spectrometer. Right panel: Polynomial fitting of fluorescence spectral peaks versus PMT channel.

The spectral resolution of a factory-calibrated QE6500 spectrometer is 0.4 nm/pixel, whereas the spectral resolution of a multichannel PMT is around 12.5 nm/channel. The following MATLAB code performs binning of the spectra, obtained with a QE6500 spectrometer.

```
clear all; clc                          %clear screen and memory
i=0:17;                                 %the number of PMT channels with extra one channel
A=343.79;B=20.104;C=-0.36979;           %parameters of polynomial wavelength calibration curve
l=A+i.*B+C.*i.^2;                       %calculates the vector of wavelengths corresponding to
                                        %central wavelength for each PMT channel
[files,path]=uigetfile('*.*');          %opens dialog to upload a file containing a spectrum
data=importdata(fullfile(path,files));  %creates matrix with uploaded data from a file
lambda=data(:,1);Fl=data(:,2);          %first and second columns of the uploaded matrix
                                        %copied as wavelength and fluorescence intensity vectors
for j=1:16                              %beginning of for cycle for each PMT channel
    w_i_ind(j)=find(lambda>(l(j)+l(j+1))/2,1);   %finds the blue border wavelength for the PMT
                                                 %channel
```

```
w_f_ind(j)=find(lambda>(l(j+1)+l(j+2))/2,1); %finds the red border wavelength for the PMT
                                              %channel
area(j)=trapz((w_i_ind(j):w1_f_ind(j)),Fl(w1_i_ind(j):w1_f_ind(j)));   %integrates fluorescent
%intensity points through the wavelengths between blue and red border of a PMT channel
end                                           %end of cycle
N=max(area)/max(Fl);                          %normalization
plot(l(2:17),area,'*',lambda,Fl.*N);          %plot input and binned spectra
```

Applying the binning script for each of the TPEF spectra, obtained with QE6500, the new 16-point spectra are calculated with peaks in the different regions (blue, green, red). Comparing the values of the binned spectra with those obtained with a multichannel PMT, correction coefficients were obtained (Figure 56). Two channels, which correspond to wavelengths shorter than 400 nm, were omitted due to being out of the spectral window of our interest.

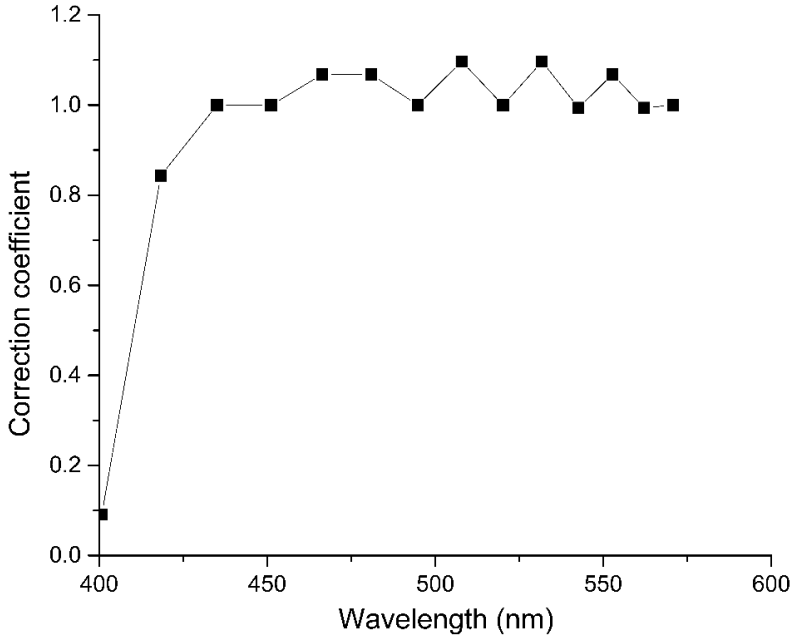

Figure 56. 14 intensity correction coefficients for channels of a PML-16-C detector. 2 channels are not corrected for a reason being out of the region of interest.

By performing wavelength and intensity calibration we ensure that the measured TPEF emission spectra with a multichannel PMT correspond to those reported in the literature.

APPENDIX-II Supplementary materials for scoring lethality in *D. melanogaster* population

S1 Modifications to the protocol for the visualization of apoptosis

During dissection, the larvae and tissues were kept ice-cold in 1X PBS at a pH of 7.4 (Ambion, Austin, TX). The PBS was then removed and a mixture of 500 µm of 4% paraformaldehyde in PBS was prepared from a 40% paraformaldehyde EM grade aqueous solution (Electron Microscopy Sciences, Hatfield, PA) and 500 µm of Heptane (obtained from Jade Scientific, Canton, MI) with rotation for 30 minutes was added. This fix was then removed and the samples were rinsed and washed twice with PBT, a mixture of PBS with 0.1% Tween-20 (Acros Organics, Morris Plains, NJ), while rotating for an additional 5 minutes. The samples were then rinsed and washed with methanol for another 30 minutes while rotating and stored in a fresh solution of methanol at -20ºC until they were processed for labeling.

To start this processing, the samples were first rehydrated through a series of 75%, 50%, and 25% methanol in PBT treatments. The tissues were then treated with Proteinase K (Fisher Scientific, Pittsburgh, PA), followed by 10 µg/mL of PBT for 5 minutes, two washes of PBT, post-fixed for 20 minutes in a solution of 4% paraformaldehyde in PB, and washed an additional five times (5 minutes each) in PBT. The samples were then equilibrated for 1 hour at room temperature in ApopTag® Equilibration Buffer and incubated overnight at 37°C in a reaction mixture consisting of ApopTag® reaction buffer and terminal deoxyribonucleotidyl transferase (Millipore, Temegula, CA) in a 2:1 ratio with 0.3% Triton X-100 (Promega, Madison, WI). On the following day, the reaction mixture was removed from the tissue and the samples were incubated in an ApopTag® stop-wash buffer (Millipore, Temegula, CA) diluted to a 1:34 ratio in water at 37°C for 4 hours (first with three quick washes, then once every 30 min). The stop-wash buffer was then removed and the samples were washed 3 times for 5 minutes each in PBT. The tissue samples were then blocked in a solution of 2 mg/mL BSA (Fisher Scientific, Fair Lawn, NJ) and 5% normal goat serum (Jackson ImmunoResearch Laboratories Inc, West Grove, PA) for 1 hour at room temperature and incubated with a 1:100 ratio mixture of Anti-Digoxigenin-Fluorescein Fab fragments (Roche, Indianapolis, IN) in PBT overnight at 4°C. The samples were finally washed four times for 20 minutes each

in PBT and mounted with DAKO fluorescent mounting medium (Dako Denmark, Glostrup, Denmark) to be imaged the following day.

S2 Deaths in populations of larvae irradiated with femtosecond pulses

Overall, early deaths contributed to 67% of the total deaths and showed to have a 6 ± 3% higher statistical impact when compared with the deaths that occurred during the later stages of development. The control larvae demonstrated a relatively low total number of deaths, 9±3% for n=140 (14 experiments).

When the larvae were treated with NIR femtosecond pulses with energy densities of ~40 J/m² or less, the survival of the experimental groups were not significantly different compared to the control groups ($P>0.05$, two-tailed U-test). The results under these energy densities were: 18±6% (27 J/m², 37 fs, n=40, 4 experiments); 17±9% (42 J/m², 37 fs, n=60, 6 experiments), and 19±3% (42 J/m², 100 fs, n=70, 7 experiments). For these three groups, early deaths were the major contributor to the total survival, where the percentages of early deaths were 71%, 60% and 77 %, respectively. As the energy density was increased to ~55 J/m² or more, the effect of the irradiation became more separated from the noise. The total rate of death achieved in this region were 30 ± 5% (56 J/m², 37 fs, n=60, 6 experiments) and 27 ± 10% (64 J/m², 100 fs, n=70, 7 experiments). For these experiments, early deaths contributed to 72% and 84% of the total number of deaths, respectively, and there was no statistically significant difference between the two pulse durations or the separate growth of early and late survival ($P>0.05$). There was, however, an observed difference between the total deaths of the group irradiated with 37 fs pulses and the control group ($P<0.01$). The rate of death in the larvae populations started to significantly increase in comparison with the control ($P<0.0001$) when energy densities approached 100 J/m² or more: 70±7%, (86 J/m², 37 fs, n=60, 6 experiments) and 73±5% (116 J/m², 100fs, n=70, 7 experiments). This rise in the total percentage of deaths was accompanied by significantly higher ($P\leq0.0001$) numbers during the early (larva) stage when compared to the controls: 62±11% and 60±7%, respectively (or 88% and 82% of total deaths, respectively). The use of these higher energy density pulses caused the larvae populations to reach terminal numbers: 95±4% (126 J/m², 37 fs, n=20, 2 experiments), 100±0% (197 J/m², 37 fs, n=20, 2 experiments) and 100±0% (238 J/m²,

100 fs, n=20, 2 experiments). For these, the early lethality contributed to ~95% of the total deaths, diminishing the impact of the delayed deaths.

In general, these results show that irradiation with higher energy densities increased the contribution of deaths during the early phase compared to the delayed deaths. By analyzing the dynamics of the delayed deaths in the pupa versus the fly stage, we found that the actually number of deaths during the pupa stage also had a gradual increase. For example, 37 fs and 100 fs pulses with energy flows of ~42 J/m² induced deaths of 8±6% (6 experiments) and 5±3% (7 experiments) of pupae, while 37 fs pulses at 86 J/m² increased the pupa death to 17±9% (6 experiments), 100 fs pulse at 115 J/m² (7 experiments) killed 30±7% ($P<0.01$), and 37 fs 126 J/m² pulses (6 experiments) killed 50±25% of pupae. Finally, 100% of the pupae died when we applied pulses with energy densities of ~200 J/m² (197 J/m² 37 fs and 238 J/m² 100 fs, 2 experiments in each case).

S3 Lethality as a function of n-photon signal

Lethality as function of energy density per pulse and pulse duration can be described by the Dose-response relationship[169]:

$$L(E_p, \tau) = C + \frac{1-C}{1+10^{-\frac{E_p - E_m(\tau)}{E_s(\tau)}}} \quad \text{(S1)}$$

where L is the lethality fraction, E_p is the energy fluence per pulse (J/m^2), τ is the pulse duration, C is the lethality fraction of the control group, E_m is the energy dose required to kill half the population proportional to the equation, $(\frac{1-C}{2} + C)$, and E_s is the energy sensitivity characteristic of the organism.

For pulsed irradiation, the n-photon absorption rate is given by:

$$R_a^{(n)} = f \frac{\sigma_n}{(hc/\lambda)^n} \int_0^{1/f} I^n(t) dt \quad \text{(S2)}$$

where R_a is the n-photon absorption rate, f is the repetition rate of laser pulses, h is Plank's constant, c is speed of light, λ is the wavelength, σ_n is n-photon absorption cross section, and $I(t)$ denotes the intensity of laser light. If the intensity profile has Gaussian shape, then the n-photon absorption rate can be written as:

$$R_a^{(n)} = R_0 \times {I_p}^n \times \tau = R_0 \times \frac{E_p^n}{\tau^n} \times \tau = R_0 \times \frac{E_p^n}{\tau^{n-1}} \quad \text{(S3)}$$

where I_p is the peak intensity of the pulse, and R_0 is a constant.

The N-photon signal coming out of a sample is proportional to the absorption rate. The signal, in arbitrary units (a.u.) and ignoring the constants, can be calculated as following:

$$S_p^{(n)} = \frac{E_p^n}{\tau^{n-1}} \quad \text{(S4)}$$

From this equation, the energy fluence per pulse can also be derived as a function of the n-photon signal:

$$E_p = \sqrt[n]{S_p^{(n)}} \times \tau^{\frac{n-1}{n}} \quad \text{(S5)}$$

Finally, using this equation, lethality as a function of *n*-photon signal in a.u. can be derived as the following:

$$L(S_p^{(n)}, \tau) = C + \frac{1-C}{1+10^{-\frac{\sqrt[n]{S_p^{(n)}} \times \tau^{\frac{n-1}{n}} - E_m(\tau)}{E_S(\tau)}}} \quad \text{(S6)}$$

S4 Calculation of the non-linearity level *l* in the intermediate region of the dose-response curve

From the experiments involving two different pulse durations, it is possible to find the same lethality level that gives rise to different energy fluences:

$$L(E_1, \tau_1) = L(E_2, \tau_2) \quad \text{(S7)}$$

In the intermediate region of the dose-response curve, we assumed an *l*-order process to be the primary cause of death:

$$L(E_p, \tau) = K \times \int_0^{1/f} I^n(t)dt = K^* \times \frac{E_p^l}{\tau^{l-1}} \quad \text{(S8)}$$

where *K* and K^* are constants. Using Eq. S7 and S8, we drew the conclusion that:

$$\frac{{E_1}^l}{{\tau_1}^{l-1}} \times \frac{{\tau_2}^{l-1}}{{E_2}^l} = 1 \quad \text{(S9)}$$

By taking the natural logarithm, l was found to be:

$$l = \frac{\ln(\tau_2/\tau_1)}{\ln\left(\frac{E_1 \times \tau_2}{E_2 \times \tau_1}\right)} \quad \text{(S10)}$$

It is also possible to calculate the order of the non-linearity using two different approaches: directly from experimental data or calculations after fitting. In the first case, energy fluences from experimental data for two different pulse durations are plugged into previously derived equations. For the set of data, the average value and dispersion was calculated to be:

$$l_{av} = \frac{\sum_{i=1}^{k} l_i}{k} \ , \qquad \sigma_l = \sqrt{\frac{\sum_{i=1}^{k} (l_i - l_{av})^2}{k}} \tag{S11}$$

where l_{av} is the average value of the non-linearity coefficient, σ_l is the dispersion of the calculated non-linearity coefficient, k is the total number of calculations, and i is the index of the non-linearity coefficient.

Fitting the experimental data into a dose-response curve provides analytical relations between energy fluences for experiments with two different pulse durations:

$$E_2 = E_m(\tau_2) - \frac{(E_m(\tau_1) - E_1) \times E_s(\tau_2)}{E_s(\tau_1)} \tag{S12}$$

Using this relation, the non-linearity coefficient can be derived as a function of energy fluence:

$$l = \frac{\ln(\tau_2/\tau_1)}{\ln\left(\frac{\tau_2}{\tau_1}\right) - \ln\left(\frac{E_m(\tau_2) - \frac{(E_m(\tau_1) - E_1) \times E_s(\tau_2)}{E_s(\tau_1)}}{E_1}\right)} \tag{S13}$$

Using smooth fitting curves, the non-linearity coefficient can be calculated for each lethality level. The average value and dispersion can be calculated using the equations:

$$l_{av} = \frac{\int_{E_I}^{E_{II}} l(E)dE}{E_{II} - E_I} \qquad \sigma_l = \sqrt{\frac{\int_{E_I}^{E_{II}} [l(E) - l_{av}]^2 dE}{E_{II} - E_I}} \tag{S14}$$

where E_I is the energy fluence where the intermediate region of the lethality curve begins and E_{II} is the energy fluence where the intermediate region of the lethality curve ends.

S5 *n*-photon signal as a function of pulse duration for a given lethality level

Calculation of the non-linearity coefficient l (Equation S10) using data from experiments with two different pulse durations allowed us to mathematically simulate the dependence of *n*-photon signal as a function of the laser pulse duration.

According to the Equation S9, the relation between energy fluences for different pulse durations can be rewritten as the following:

$$E(\tau) = E(\tau_1) \times \left(\frac{\tau}{\tau_1}\right)^{\frac{l-1}{l}} \quad \text{(S15)}$$

Combining the equation above with Equation S4, the expected normalized *n*-photon signal per pulse as a function of pulse duration for a fixed lethality level can be determined as:

$$S_p^{(n)}(\tau) = \big(E(\tau)\big)^n / \tau^{n-1} = \left(\frac{E_1}{\tau_1^{\frac{l-1}{l}}}\right)^n / \tau^{\frac{n}{l}-1} \quad \text{(S16)}$$

APPENDIX-III Publication List

1. I. Saytashev, R. Glenn, G.A. Murashova, S. Osseiran, D.M. Spence, C.L. Evans, and M. Dantus, "Multiphoton excited hemoglobin fluorescence and third harmonic generation for non-invasive microscopy of stored RBCs," in review.
2. I. Saytashev, M. Nairat, S. Bonora, V.V. Lozovoy, M. Dantus, "Deformable mirror for 400 nm pulse shaping", to be submitted.
3. R. Glenn, I. Saytashev, M. Dantus, "Measuring the Real and Imaginary Components of the Third-Order Molecular Polarization Using a Single Shaped Pulse," Phys. Rev. A., to be submitted.
4. I. Saytashev, M. Murphy, S. Osseiran, D.M. Spence, C.L. Evans, M. Dantus, "The nature of multiphoton fluorescence from red blood cells," SPIE BiOS, 97121W-97121W-4 (2016).
5. S.N. Arkhipov, I. Saytashev, M. Dantus, "Intravital Imaging Study on Photodamage Produced by Femtosecond Near-infrared Laser Pulses *In Vivo*," Photochemistry and photobiology 92 (2), 308-313 (2016).
6. M. Balu, I. Saytashev, J. Hou, M. Dantus, B.J. Tromberg, "Sub-40 fs, 1060-nm Yb-fiber laser enhances penetration depth in nonlinear optical microscopy of human skin," Journal of biomedical optics 20 (12), 120501-120501 (2015).
7. R. Mittal, R. Glenn, I. Saytashev, V.V. Lozovoy, M. Dantus, "Femtosecond nanoplasmonic dephasing of individual silver nanoparticles and small clusters," The journal of physical chemistry letters 6 (9), 1638-1644 (2015).
8. R. Mittal, R. Glenn, I. Saytashev, M. Dantus, "Femtosecond nanoplasmonic dephasing of individual silver nanoparticles," Bulletin of the American Physical Society 60 (2015).
9. I. Saytashev, M. Dantus, "Multimodal Imaging of highly pigmented tissues," Biomedical Optics, BT3A. 18 (2014).
10. I. Saytashev, B. Xu, M.T. Bremer, M. Dantus, "Simultaneous selective two-photon microscopy using MHz rate pulse shaping and quadrature detection of the time-multiplexed signal," SPIE BiOS, 89482F-89482F-4 (2014).
11. I. Saytashev, S.N. Arkhipov, N. Winkler, K. Zuraski, V.V. Lozovoy, M. Dantus, "Pulse duration and energy dependence of photodamage and lethality induced by femtosecond near infrared laser pulses in *Drosophila melanogaster*," Journal of Photochemistry and Photobiology B: Biology 115, 42-50 (2012).
12. B. Nie, I. Saytashev, A. Chong, H. Liu, S.N. Arkhipov, F.W. Wise, M. Dantus, "Multimodal microscopy with sub-30 fs Yb-fiber laser oscillator," Biomedical optics express 3 (7), 1750-1756 (2012).
13. I. Saytashev, B. Nie, A. Chong, H. Liu, S. Arkhipov, F.W. Wise, M. Dantus, "Multiphoton imaging with sub-30 fs Yb-fiber laser," SPIE BiOS, 82261I-82261I-6 (2012).

BIBLIOGRAPHY

BIBLIOGRAPHY

1. M. Göppert-Mayer, "Über Elementarakte mit zwei Quantensprüngen," **401**, 273-294 (1931).

2. S. M. Hankin, D. M. Villeneuve, P. B. Corkum, and D. M. Rayner, "Intense-field laser ionization rates in atoms and molecules," **64**, 013405 (2001).

3. P. A. Franken, A. E. Hill, C. W. Peters, and G. Weinreich, "Generation of Optical Harmonics," **7**, 118-119 (1961).

4. W. Denk, J. H. Strickler, and W. W. Webb, "2-Photon Laser Scanning Fluorescence Microscopy," Science **248**, 73-76 (1990).

5. E. G. Robertson and G. Baxter, "Tumour seeding following percutaneous needle biopsy: The real story!," **66**, 1007-1014 (2011).

6. D. Yelin and Y. Silberberg, "Laser scanning third-harmonic-generation microscopy in biology," Opt. Express **5**, 169-175 (1999).

7. N. G. Horton, K. Wang, D. Kobat, C. G. Clark, F. W. Wise, C. B. Schaffer, and C. Xu, "In vivo three-photon microscopy of subcortical structures within an intact mouse brain," Nat Photonics **7**, 205-209 (2013).

8. K. König, "Multiphoton microscopy in life sciences," Journal of microscopy **200**, 83-104 (2000).

9. R. W. Boyd, *Nonlinear Optics* (Academic Press, 2003).

10. R. M. Williams, W. R. Zipfel, and W. W. Webb, "Interpreting Second-Harmonic Generation Images of Collagen I Fibrils," **88**, 1377-1386 (2005).

11. Y. Barad, H. Eisenberg, M. Horowitz, and Y. Silberberg, "Nonlinear scanning laser microscopy by third harmonic generation," Appl Phys Lett **70**, 922-924 (1997).

12. L. G. Gouy, *Sur une propriété nouvelle des ondes lumineuses* (Gauthier-Villars, 1890).

13. J. X. Cheng and X. S. Xie, "Green's function formulation for third-harmonic generation microscopy," J Opt Soc Am B **19**, 1604-1610 (2002).

14. D. Débarre, N. Olivier, and E. Beaurepaire, "Signal epidetection in third-harmonic generation microscopy of turbid media," Opt. Express **15**, 8913-8924 (2007).

15. D. Debarre, W. Supatto, A. M. Pena, A. Fabre, T. Tordjmann, L. Combettes, M. C. Schanne-Klein, and E. Beaurepaire, "Imaging lipid bodies in cells and tissues using third-harmonic generation microscopy," Nat Methods **3**, 47-53 (2006).

16. C. Xu, W. Zipfel, J. B. Shear, R. M. Williams, and W. W. Webb, "Multiphoton fluorescence excitation: new spectral windows for biological nonlinear microscopy," PNAS **93**, 10763-10768 (1996).

17. D. Sinefeld, H. P. Paudel, D. G. Ouzounov, T. G. Bifano, and C. Xu, "Adaptive optics in multiphoton microscopy: comparison of two, three and four photon fluorescence," Opt Express **23**, 31472-31483 (2015).

18. W. R. Zipfel, R. M. Williams, and W. W. Webb, "Nonlinear magic: multiphoton microscopy in the biosciences," Nature biotechnology **21**, 1369-1377 (2003).

19. P. Xi, Y. Andegeko, D. Pestov, V. V. Lovozoy, and M. Dantus, "Two-photon imaging using adaptive phase compensated ultrashort laser pulses," J. Biomed. Opt. **14**, 014002 (2009).

20. M. Balu, C. B. Zachary, R. M. Harris, T. B. Krasieva, K. Konig, B. J. Tromberg, and K. M. Kelly, "In Vivo Multiphoton Microscopy of Basal Cell Carcinoma," JAMA dermatology **151**, 1068-1074 (2015).

21. M. J. Booth, M. A. Neil, R. Juskaitis, and T. Wilson, "Adaptive aberration correction in a confocal microscope," PNAS **99**, 5788-5792 (2002).

22. D. Debarre, E. J. Botcherby, T. Watanabe, S. Srinivas, M. J. Booth, and T. Wilson, "Image-based adaptive optics for two-photon microscopy," Opt. Lett. **34**, 2495-2497 (2009).

23. M. Born, E. Wolf, A. B. Bhatia, D. Gabor, A. R. Stokes, A. M. Taylor, P. A. Wayman, and W. L. Wilcock, *Principles of Optics: Electromagnetic Theory of Propagation, Interference and Diffraction of Light* (Cambridge University Press, 2000).

24. J. D. Jackson, *Classical electrodynamics* (Wiley, 1975).

25. B. Xu, J. M. Gunn, J. M. D. Cruz, V. V. Lozovoy, and M. Dantus, "Quantitative investigation of the multiphoton intrapulse interference phase scan method for simultaneous phase measurement and compensation of femtosecond laser pulses," J. Opt. Soc. Am. B **23**, 750-759 (2006).

26. V. V. Lozovoy, I. Pastirk, and M. Dantus, "Multiphoton intrapulse interference 4; Characterization and compensation of the spectral phase of ultrashort laser pulses," Opt. Lett. **29**, 775-777 (2004).

27. D. Pestov, V. V. Lozovoy, and M. Dantus, "Multiple Independent Comb Shaping (MICS): Phase-only generation of optical pulse sequences," Opt. Express **17**, 14351-14361 (2009).

28. A. Konar, V. V. Lozovoy, and M. Dantus, "Electronic dephasing of molecules in solution measured by nonlinear spectral inteferometry," **4**, 26 (2014).

29. M. Dantus and V. V. Lozovoy, "Experimental Coherent Laser Control of Physicochemical Processes," Chem Rev **104**, 1813-1860 (2004).

30. P. Brumer and M. Shapiro, "Laser Control of Molecular Processes," Annual review of physical chemistry **43**, 257-282 (1992).

31. W. S. Warren, H. Rabitz, and M. Dahleh, "Coherent Control of Quantum Dynamics: The Dream Is Alive," Science **259**, 1581-1589 (1993).

32. C. J. Bardeen, V. V. Yakovlev, K. R. Wilson, S. D. Carpenter, P. M. Weber, and W. S. Warren, "Feedback quantum control of molecular electronic population transfer," Chem Phys Lett **280**, 151-158 (1997).

33. T. Brixner, N. H. Damrauer, P. Niklaus, and G. Gerber, "Photoselective adaptive femtosecond quantum control in the liquid phase," Nature **414**, 57-60 (2001).

34. A. Konar, V. V. Lozovoy, and M. Dantus, "Solvent Environment Revealed by Positively Chirped Pulses," The journal of physical chemistry letters **5**, 924-928 (2014).

35. K.-C. Tang and R. J. Sension, "The influence of the optical pulse shape on excited state dynamics in provitamin D3," Faraday discussions **153**, 117-129 (2011).

36. M. Wollenhaupt and T. Baumert, "Ultrafast laser control of electron dynamics in atoms, molecules and solids," Faraday discussions **153**, 9-26 (2011).

37. C. J. Bardeen, Q. Wang, and C. V. Shank, "Femtosecond chirped pulse excitation of vibrational wave packets in LD690 and bacteriorhodopsin," J Phys Chem A **102**, 2759-2766 (1998).

38. A. M. Weiner, "Femtosecond pulse shaping using spatial light modulators," Rev Sci Instrum **71**, 1929-1960 (2000).

39. M. Hacker, G. Stobrawa, R. Sauerbrey, T. Buckup, M. Motzkus, M. Wildenhain, and A. Gehner, "Micromirror SLM for femtosecond pulse shaping in the ultraviolet," Appl Phys B-Lasers O **76**, 711-714 (2003).

40. M. Roth, M. Mehendale, A. Bartelt, and H. Rabitz, "Acousto-optical shaping of ultraviolet femtosecond pulses," Appl Phys B **80**, 441-444 (2005).

41. B. J. Pearson and T. C. Weinacht, "Shaped ultrafast laser pulses in the deep ultraviolet," Opt. Express **15**, 4385-4388 (2007).

42. S. Coudreau, D. Kaplan, and P. Tournois, "Ultraviolet acousto-optic programmable dispersive filter laser pulse shaping in KDP," Opt. Lett. **31**, 1899-1901 (2006).

43. N. T. Form, R. Burbidge, J. Ramon, and B. J. Whitaker, "Parameterization of an acousto-optic programmable dispersive filter for closed-loop learning experiments," J Mod Optic **55**, 197-209 (2008).

44. A. Cartella, S. Bonora, M. Först, G. Cerullo, A. Cavalleri, and C. Manzoni, "Pulse shaping in the mid-infrared by a deformable mirror," Opt. Lett. **39**, 1485-1488 (2014).

45. S. Bonora, D. Brida, P. Villoresi, and G. Cerullo, "Ultrabroadband pulse shaping with a push-pull deformable mirror," Opt. Express **18**, 23147-23152 (2010).

46. R. Tyson, *Adaptive Optics Engineering Handbook* (CRC Press, 1999).

47. Y. Coello, V. V. Lozovoy, T. C. Gunaratne, B. Xu, I. Borukhovich, C.-h. Tseng, T. Weinacht, and M. Dantus, "Interference Without an Interferometer: a Different Approach to Measuring, Compressing, and Shaping Ultrashort Laser Pulses," J. Opt. Soc. Am. B **25**, A140-A150 (2008).

48. A. Konar, V. V. Lozovoy, and M. Dantus, "Solvation Stokes-Shift Dynamics Studied by Chirped Femtosecond Laser Pulses," J. Phys. Chem. Lett. **3**, 2458-2464 (2012).

49. A. Yu, C. A. Tolbert, D. A. Farrow, and D. M. Jonas, "Solvatochromism and Solvation Dynamics of Structurally Related Cyanine Dyes," J Phys Chem A **106**, 9407-9419 (2002).

50. G. Jones, W. R. Jackson, and A. M. Halpern, "Medium effects on fluorescence quantum yields and lifetimes for coumarin laser dyes," **72**, 391-395 (1980).

51. N. Olivier, D. Debarre, and E. Beaurepaire, "Dynamic aberration correction for multiharmonic microscopy," Opt. Lett. **34**, 3145-3147 (2009).

52. D. Burke, B. Patton, F. Huang, J. Bewersdorf, and M. J. Booth, "Adaptive optics correction of specimen-induced aberrations in single-molecule switching microscopy," Optica **2**, 177-185 (2015).

53. B. Nie, D. Pestov, F. W. Wise, and M. Dantus, "An ultrafast fiber laser with self-similar evolution in the gain segment," Opt. Photon. News **22**, 47-47 (2011).

54. Y. Jian, J. Xu, M. A. Gradowski, S. Bonora, R. J. Zawadzki, and M. V. Sarunic, "Wavefront sensorless adaptive optics optical coherence tomography for in vivo retinal imaging in mice," Biomed. Opt. Express **5**, 547-559 (2014).

55. S. Bonora and R. J. Zawadzki, "Wavefront sensorless modal deformable mirror correction in adaptive optics: optical coherence tomography," Opt. Lett. **38**, 4801-4804 (2013).

56. I. Pastirk, J. Dela Cruz, K. Walowicz, V. Lozovoy, and M. Dantus, "Selective two-photon microscopy with shaped femtosecond pulses," Opt. Express **11**, 1695-1701 (2003).

57. V. V. Lozovoy, I. Pastirk, K. A. Walowicz, and M. Dantus, "Multiphoton intrapulse interference. II. Control of two- and three-photon laser induced fluorescence with shaped pulses," **118**, 3187-3196 (2003).

58. G. Labroille, R. S. Pillai, X. Solinas, C. Boudoux, N. Olivier, E. Beaurepaire, and M. Joffre, "Dispersion-based pulse shaping for multiplexed two-photon fluorescence microscopy," Opt. Lett. **35**, 3444-3446 (2010).

59. P. Xi, Y. Andegeko, L. R. Weisel, V. V. Lozovoy, and M. Dantus, "Greater signal, increased depth, and less photobleaching in two-photon microscopy with 10 fs pulses," Opt Commun **281**, 1841-1849 (2008).

60. S. Maiti, J. B. Shear, R. M. Williams, W. R. Zipfel, and W. W. Webb, "Measuring serotonin distribution in live cells with three-photon excitation," Science **275**, 530-532 (1997).

61. J. A. Squier, M. Muller, G. J. Brakenhoff, and K. R. Wilson, "Third harmonic generation microscopy," Opt Express **3**, 315-324 (1998).

62. D. Yelin, D. Oron, E. Korkotian, M. Segal, and Y. Silberberg, "Third-harmonic microscopy with a titanium-sapphire laser," Appl Phys B-Lasers O **74**, S97-S101 (2002).

63. C. K. Sun, S. W. Chu, S. P. Tai, S. Keller, U. K. Mishra, and S. P. DenBaars, "Scanning second-harmonic/third-harmonic generation microscopy of gallium nitride," Appl Phys Lett **77**, 2331 (2000).

64. A. Chong, J. Buckley, W. Renninger, and F. Wise, "All-normal-dispersion femtosecond fiber laser," Opt. Express **14**, 10095-10100 (2006).

65. A. Chong, H. Liu, B. Nie, B. G. Bale, S. Wabnitz, W. H. Renninger, M. Dantus, and F. W. Wise, "Pulse generation without gain-bandwidth limitation in a laser with self-similar evolution," Opt Express **20**, 14213-14220 (2012).

66. A. C. Millard, P. W. Wiseman, D. N. Fittinghoff, K. R. Wilson, J. A. Squier, and M. M¸ller, "Third-harmonic generation microscopy by use of a compact, femtosecond fiber laser source," Appl Optics **38**, 7393-7397 (1999).

67. G. J. Liu, K. Kieu, F. W. Wise, and Z. P. Chen, "Multiphoton microscopy system with a compact fiber-based femtosecond-pulse laser and handheld probe," J Biophotonics **4**, 34-39 (2011).

68. B. Nie, D. Pestov, F. W. Wise, and M. Dantus, "Generation of 42-fs and 10-nJ pulses from a fiber laser with self-similar evolution in the gain segment," Opt. Express **19**, 12074-12080 (2011).

69. S. H. Huang, A. A. Heikal, and W. W. Webb, "Two-photon fluorescence spectroscopy and microscopy of NAD(P)H and flavoprotein," Biophys J **82**, 2811-2825 (2002).

70. B. Nie, I. Saytashev, A. Chong, H. Liu, S. N. Arkhipov, F. W. Wise, and M. Dantus, "Multimodal microscopy with sub-30 fs Yb fiber laser oscillator," Biomed. Opt. Express **3**, 1750-1756 (2012).

71. C. Xu and F. W. Wise, "Recent advances in fibre lasers for nonlinear microscopy," Nat Photonics **7**, 875-882 (2013).

72. M. Balu, K. M. Kelly, C. B. Zachary, R. M. Harris, T. B. Krasieva, K. Konig, A. J. Durkin, and B. J. Tromberg, "Distinguishing between benign and malignant melanocytic nevi by in vivo multiphoton microscopy," Cancer research **74**, 2688-2697 (2014).

73. E. Dimitrow, M. Ziemer, M. J. Koehler, J. Norgauer, K. Konig, P. Elsner, and M. Kaatz, "Sensitivity and specificity of multiphoton laser tomography for in vivo and ex vivo diagnosis of malignant melanoma," The Journal of investigative dermatology **129**, 1752-1758 (2009).

74. M. Balu, A. Mazhar, C. K. Hayakawa, R. Mittal, T. B. Krasieva, K. Konig, V. Venugopalan, and B. J. Tromberg, "In vivo multiphoton NADH fluorescence reveals depth-dependent keratinocyte metabolism in human skin," Biophys J **104**, 258-267 (2013).

75. Y. H. Liao, W. C. Kuo, S. Y. Chou, C. S. Tsai, G. L. Lin, M. R. Tsai, Y. T. Shih, G. G. Lee, and C. K. Sun, "Quantitative analysis of intrinsic skin aging in dermal papillae by in vivo harmonic generation microscopy," Biomed. Opt. Express **5**, 3266-3279 (2014).

76. M. J. Koehler, K. Konig, P. Elsner, R. Buckle, and M. Kaatz, "In vivo assessment of human skin aging by multiphoton laser scanning tomography," Opt. Lett. **31**, 2879-2881 (2006).

77. R. Bazin, F. Flament, A. Colonna, R. Le Harzic, R. Buckle, B. Piot, F. Laize, M. Kaatz, K. Konig, and J. W. Fluhr, "Clinical study on the effects of a cosmetic product on dermal extracellular matrix components using a high-resolution multiphoton tomograph," Skin research and technology : official journal of International Society for Bioengineering and the Skin **16**, 305-310 (2010).

78. M. Balu, T. Baldacchini, J. Carter, T. B. Krasieva, R. Zadoyan, and B. J. Tromberg, "Effect of excitation wavelength on penetration depth in nonlinear optical microscopy of turbid media," J. Biomed. Opt. **14**, 010508 (2009).

79. D. Kobat, M. E. Durst, N. Nishimura, A. W. Wong, C. B. Schaffer, and C. Xu, "Deep tissue multiphoton microscopy using longer wavelength excitation," Opt Express **17**, 13354-13364 (2009).

80. S. Tang, T. B. Krasieva, Z. Chen, G. Tempea, and B. J. Tromberg, "Effect of pulse duration on two-photon excited fluorescence and second harmonic generation in nonlinear optical microscopy," J. Biomed. Opt. **11**, 020501 (2006).

81. P. Theer, M. T. Hasan, and W. Denk, "Two-photon imaging to a depth of 1000 microm in living brains by use of a Ti:Al2O3 regenerative amplifier," Opt. Lett. **28**, 1022-1024 (2003).

82. W. Min, S. Lu, S. Chong, R. Roy, G. R. Holtom, and X. S. Xie, "Imaging chromophores with undetectable fluorescence by stimulated emission microscopy," Nature **461**, 1105-1109 (2009).

83. S. Y. Chen, H. Y. Wu, and C. K. Sun, "In vivo harmonic generation biopsy of human skin," J. Biomed. Opt. **14**, 060505 (2009).

84. B. R. Masters, P. T. So, C. Buehler, N. Barry, J. D. Sutin, W. W. Mantulin, and E. Gratton, "Mitigating thermal mechanical damage potential during two-photon dermal imaging," J. Biomed. Opt. **9**, 1265-1270 (2004).

85. J. N. Bixler, B. H. Hokr, M. L. Denton, G. D. Noojin, A. D. Shingledecker, H. T. Beier, R. J. Thomas, B. A. Rockwell, and V. V. Yakovlev, "Assessment of tissue heating under tunable near-infrared radiation," J. Biomed. Opt. **19**, 070501 (2014).

86. R. Galli, V. Sablinskas, D. Dasevicius, A. Laurinavicius, F. Jankevicius, E. Koch, and G. Steiner, "Non-linear optical microscopy of kidney tumours," J Biophotonics **7**, 23-27 (2014).

87. S. Tang, J. Liu, T. B. Krasieva, Z. P. Chen, and B. J. Tromberg, "Developing compact multiphoton systems using femtosecond fiber lasers," J Biomed Opt **14**, 030508 (2009).

88. D. Fu, T. Ye, T. E. Matthews, B. J. Chen, G. Yurtserver, and W. S. Warren, "High-resolution in vivo imaging of blood vessels without labeling," Opt. Lett. **32**, 2641-2643 (2007).

89. W. H. Renninger, A. Chong, and F. W. Wise, "Self-similar pulse evolution in an all-normal-dispersion laser," Physical review. A **82**(2010).

90. R. Jimenez and F. E. Romesberg, "Excited state dynamics and heterogeneity of folded and unfolded states of cytochrome C," J. Phys. Chem. B **106**, 9172-9180 (2002).

91. W. Zheng, D. Li, Y. Zeng, Y. Luo, and J. Y. Qu, "Two-photon excited hemoglobin fluorescence," Biomed. Opt. Express **2**, 71-79 (2010).

92. E. Chaigneau, M. Oheim, E. Audinat, and S. Charpak, "Two-photon imaging of capillary blood flow in olfactory bulb glomeruli," PNAS **100**, 13081-13086 (2003).

93. S. M. Frank, B. Abazyan, M. Ono, C. W. Hogue, D. B. Cohen, D. E. Berkowitz, P. M. Ness, and V. M. Barodka, "Decreased erythrocyte deformability after transfusion and the effects of erythrocyte storage duration," Anesth. Analg. **116**, 975-981 (2013).

94. O. N. Salaria, V. M. Barodka, C. W. Hogue, D. E. Berkowitz, P. M. Ness, J. O. Wasey, and S. M. Frank, "Impaired red blood cell deformability after transfusion of stored allogeneic blood but not autologous salvaged blood in cardiac surgery patients," Anesth. Analg. **118**, 1179-1187 (2014).

95. A. B. Zimrin and J. R. Hess, "Current issues relating to the transfusion of stored red blood cells," Vox Sang. **96**, 93-103 (2009).

96. G. Edgren, M. Kamper-Jørgensen, S. Eloranta, K. Rostgaard, B. Custer, H. Ullum, E. L. Murphy, M. P. Busch, M. Reilly, M. Melbye, H. Hjalgrim, and O. Nyrén, "Duration of red blood cell storage and survival of transfused patients (CME)," Transfusion **50**, 1185-1195 (2010).

97. S. D. Robinson, C. Janssen, E. B. Fretz, B. Berry, A. J. Chase, A. D. Siega, R. G. Carere, A. Fung, G. Simkus, W. P. Klinke, and J. D. Hilton, "Red blood cell storage duration and mortality in patients undergoing percutaneous coronary intervention," Am. Heart J. **159**, 876-881 (2010).

98. A. H. M. van Straten, M. A. Soliman Hamad, A. A. van Zundert, E. J. Martens, J. F. ter Woorst, A. M. de Wolf, and V. Scharnhorst, "Effect of duration of red blood cell storage on early and late mortality after coronary artery bypass grafting," J. Thorac. Cardiovasc. Surg. **141**, 231-237 (2011).

99. S. D. Shukla, R. Coleman, J. B. Finean, and R. H. Michell, "The use of phospholipase C to detect structural changes in the membranes of human erythrocytes aged by storage," Biochim. Biophys. Acta **512**, 341-349 (1978).

100. B. Blasi, A. D'Alessandro, N. Ramundo, and L. Zolla, "Red blood cell storage and cell morphology," Transfus. Med. **22**, 90-96 (2012).

101. I. Moon, F. Yi, Y. H. Lee, B. Javidi, D. Boss, and P. Marquet, "Automated quantitative analysis of 3D morphology and mean corpuscular hemoglobin in human red blood cells stored in different periods," Opt. Express **21**, 30947-30957 (2013).

102. G. O. Clay, C. B. Schaffer, and D. Kleinfeld, "Large two-photon absorptivity of hemoglobin in the infrared range of 780-880 nm," J. Chem. Phys. **126**, 025102 (2007).

103. W. Jy, M. Ricci, S. Shariatmadar, O. Gomez-Marin, L. H. Horstman, and Y. S. Ahn, "Microparticles in stored red blood cells as potential mediators of transfusion complications," Transfusion **51**, 886-893 (2011).

104. R. D. Schaller, J. C. Johnson, and R. J. Saykally, "Nonlinear Chemical Imaging Microscopy: Near-Field Third Harmonic Generation Imaging of Human Red Blood Cells," Anal. Chem. **72**, 5361-5364 (2000).

105. G. O. Clay, A. C. Millard, C. B. Schaffer, J. Aus-der-Au, P. S. Tsai, J. A. Squier, and D. Kleinfeld, "Spectroscopy of third-harmonic generation: evidence for resonances in model compounds and ligated hemoglobin," J. Opt. Soc. Am. B **23**, 932-950 (2006).

106. J. A. Meyer, J. M. Froelich, G. E. Reid, W. K. Karunarathne, and D. M. Spence, "Metal-activated C-peptide Facilitates Glucose Clearance and the Release of a Nitric Oxide Stimulus via the GLUT1 Transporter," Diabetologia **51**, 175-182 (2008).

107. Y. Wang, A. Giebink, and D. M. Spence, "Microfluidic evaluation of red cells collected and stored in modified processing solutions used in blood banking," Integr. Biol.-Uk **6**, 65-75 (2014).

108. R. Dasgupta, S. Ahlawat, R. S. Verma, A. Uppal, and P. K. Gupta, "Hemoglobin degradation in human erythrocytes with long-duration near-infrared laser exposure in Raman optical tweezers," J. Biomed. Opt. **15**, 055009 (2010).

109. J. P. Greer, D. A. Arber, B. Glader, A. F. List, R. T. Means, F. Paraskevas, and G. M. Rodgers, *Wintrobe's Clinical Hematology* (Lippincott Williams & Wilkins, 2013), p. 3094.

110. G. Brecher and M. Bessis, "Present status of spiculed red cells and their relationship to the discocyte-echinocyte transformation: a critical review," **40**, 333-344 (1972).

111. Y. Zeng, B. Yan, Q. Sun, S. K. Teh, W. Zhang, Z. Wen, and J. Y. Qu, "Label-free in vivo imaging of human leukocytes using two-photon excited endogenous fluorescence," J. Biomed. Opt. **18**, 040504 (2013).

112. L. M. Snyder, F. Garver, S. C. Liu, L. Leb, J. Trainor, and N. L. Fortier, "Demonstration of hemoglobin associated with isolated, purified spectrin from senescent human red-cells," Brit. J. Haematol. **61**, 415-419 (1985).

113. Q. Q. Sun, W. Zheng, J. N. Wang, Y. Luo, and J. N. Y. Qu, "Mechanism of two-photon excited hemoglobin fluorescence emission," J. Biomed. Opt. **20**, 105014 (2015).

114. P. P. Ho and R. R. Alfano, "Optical Kerr Effect in Liquids," Physical review. A **20**, 2170-2187 (1979).

115. A. Hopt and E. Neher, "Highly nonlinear photodamage in two-photon fluorescence microscopy," Biophys J **80**, 2029-2036 (2001).

116. W. R. Zipfel, R. M. Williams, R. Christie, A. Y. Nikitin, B. T. Hyman, and W. W. Webb, "Live tissue intrinsic emission microscopy using multiphoton-excited native fluorescence and second harmonic generation," P Natl Acad Sci USA **100**, 7075-7080 (2003).

117. J. M. Dela Cruz, J. McMullen, R. M. Williams, and W. Zipfel, "Feasibility of using multiphoton excited tissue autofluorescence for in vivo human histopathology," **1**, 1320-1330 (2010).

118. A. J. Welch and M. J. C. Van Gemert, *Optical-Thermal Response of Laser-Irradiated Tissue*, Plenum Press, New York (1995).

119. K. König, H. Liang, M. W. Berns, and B. J. Tromberg, "Cell-Damage by near-Ir Microbeams," Nature **377**, 20-21 (1995).

120. Y. Andegeko, D. Pestov, V. V. Lozovoy, and M. Dantus, "Ultrafast multiphoton microscopy with high-order spectral phase distortion compensation," in 2009), 71830W.

121. H. J. Koester, D. Baur, R. Uhl, and S. W. Hell, "Ca2+ fluorescence imaging with pico- and femtosecond two-photon excitation: Signal and photodamage," Biophys J **77**, 2226-2236 (1999).

122. K. König, T. W. Becker, P. Fischer, I. Riemann, and K. J. Halbhuber, "Pulse-length dependence of cellular response to intense near-infrared laser pulses in multiphoton microscopes," Opt. Lett. **24**, 113-115 (1999).

123. K. König, P. T. C. So, W. W. Mantulin, and E. Gratton, "Cellular response to near-infrared femtosecond laser pulses in two-photon microscopes," Opt. Lett. **22**, 135-136 (1997).

124. X. Kong, S. K. Mohanty, J. Stephens, J. T. Heale, V. Gomez-Godinez, L. Z. Shi, J.-S. Kim, K. Yokomori, and M. W. Berns, "Comparative analysis of different laser systems to study cellular responses to DNA damage in mammalian cells," Nucleic acids research **37**, e68 (2009).

125. S. W. Botchway, P. Reynolds, A. W. Parker, and P. O'Neill, "Use of near infrared femtosecond lasers as sub-micron radiation microbeam for cell DNA damage and repair studies," **704**, 38-44 (2010).

126. V. Shafirovich, A. Dourandin, N. P. Luneva, C. Singh, F. Kirigin, and N. E. Geacintov, "Multiphoton near-infrared femtosecond laser pulse-induced DNA damage with and without the photosensitizer proflavine," Photochem Photobiol **69**, 265-274 (1999).

127. P.-O. Mari, B. I. Florea, S. P. Persengiev, N. S. Verkaik, H. T. Brueggenwirth, M. Modesti, G. Giglia-Mari, K. Bezstarosti, J. A. A. Demmers, T. M. Luider, A. B. Houtsmuller, and D. C. van Gent, "Dynamic assembly of end-joining complexes requires interaction between Ku70/80 and XRCC4," P Natl Acad Sci USA **103**, 18597-18602 (2006).

128. A. Vogel, J. Noack, G. Huttman, and G. Paltauf, "Mechanisms of femtosecond laser nanosurgery of cells and tissues," Appl Phys B-Lasers O **81**, 1015-1047 (2005).

129. Y. Liu, D. K. Cheng, G. J. Sonek, M. W. Berns, C. F. Chapman, and B. J. Tromberg, "Evidence for Localized Cell Heating Induced by Infrared Optical Tweezers," Biophys J **68**, 2137-2144 (1995).

130. B. R. Masters, P. T. C. So, and E. Gratton, "Multiphoton excitation fluorescence microscopy and spectroscopy of in vivo human skin," Biophys J **72**, 2405-2412 (1997).

131. J. Paoli, M. Smedh, A.-M. Wennberg, and M. B. Ericson, "Multiphoton laser scanning microscopy on non-melanoma skin cancer: Morphologic features for future non-invasive diagnostics," The Journal of investigative dermatology **128**, 1248-1255 (2008).

132. J. V. Harper, P. Reynolds, E. L. Leatherbarrow, S. W. Botchway, A. W. Parker, and P. O'Neill, "Induction of Persistent Double Strand Breaks Following Multiphoton Irradiation of Cycling and G(1)-arrested Mammalian Cells-Replication-induced Double Strand Breaks," Photochemistry and photobiology **84**, 1506-1514 (2008).

133. F. Fischer, B. Volkmer, S. Puschmann, R. Greinert, W. Breitbart, J. Kiefer, and R. Wepf, "Risk estimation of skin damage due to ultrashort pulsed, focused near-infrared laser irradiation at 800 nm," J Biomed Opt **13**(2008).

134. U. K. Tirlapur, K. Konig, C. Peuckert, R. Krieg, and K. J. Halbhuber, "Femtosecond near-infrared laser pulses elicit generation of reactive oxygen species in mammalian cells leading to apoptosis-like death," Experimental cell research **263**, 88-97 (2001).

135. P. E. Hockberger, T. A. Skimina, V. E. Centonze, C. Lavin, S. Chu, S. Dadras, J. K. Reddy, and J. G. White, "Activation of flavin-containing oxidases underlies light-induced production of H2O2 in mammalian cells," PNAS **96**, 6255-6260 (1999).

136. A. Mayevsky and G. G. Rogatsky, "Mitochondrial function in vivo evaluated by NADH fluorescence: from animal models to human studies," American journal of physiology. Cell physiology **292**, C615-C640 (2007).

137. K. A. Franco W, Ronan SJ, Grekin RC, McCalmont TH., "Hyperthermic injury to adipocyte cells by selective heating of subcutaneous fat with a novel radiofrequency device: feasibility studies.," Laser Surg Med **42**, 361-370 (2010).

138. G. Arturson and S. Mellander, "Acute Changes in Capillary Filtration and Diffusion in Experimental Burn Injury," Acta physiologica Scandinavica **62**, 457-463 (1964).

139. H. P. Friedl, G. O. Till, O. Trentz, and P. A. Ward, "Roles of Histamine, Complement and Xanthine-Oxidase in Thermal-Injury of Skin," Am. J. Pathol. **135**, 203-217 (1989).

140. D. Li, W. Zheng, Y. Zeng, Y. Luo, and J. Y. Qu, "Two-photon excited hemoglobin fluorescence provides contrast mechanism for label-free imaging of microvasculature in vivo," Opt. Lett. **36**, 834-836 (2011).

141. M. A. Tycon, A. Chakraborty, and C. J. Fecko, "Generation of DNA photolesions by two-photon absorption of a frequency-doubled Ti:sapphire laser," Journal of photochemistry and photobiology. B, Biology **102**, 161-168 (2011).

142. Matthew K. Daddysman and Christopher J. Fecko, "DNA Multiphoton Absorption Generates Localized Damage for Studying Repair Dynamics in Live Cells," Biophys J **101**, 2294-2303 (2011).

143. K. B. Roos WP, "DNA damage-induced cell death by apoptosis.," Trends in molecular medicine **2**, 440-450 (2006).

144. E. Reefman, P. C. Limburg, C. G. M. Kallenberg, and M. Bijl, "Apoptosis in Human Skin: Role in Pathogenesis of Various Diseases and Relevance for Therapy.," Ann Ny Acad Sci **1051**, 52-63 (2005).

145. J. Y. J. Wang, "DNA damage and apoptosis," Cell death and differentiation **8**, 1047-1048 (2001).

146. W. Nordstrom and J. M. Abrams, "Guardian ancestry: fly p53 and damage-inducible apoptosis," Cell death and differentiation **7**, 1035-1038 (2000).

147. T. M. Buttke and P. A. Sandstrom, "Oxidative Stress as a Mediator of Apoptosis," **15**, 7-10 (1994).

148. J. J. Haddad, "Redox and oxidant-mediated regulation of apoptosis signaling pathways: immuno-pharmaco-redox conception of oxidative siege versus cell death commitment," International immunopharmacology **4**, 475-493 (2004).

149. R. A. Meldrum, S. W. Botchway, C. W. Wharton, and G. J. Hirst, "Nanoscale spatial induction of ultraviolet photoproducts in cellular DNA by three-photon near-infrared absorption," EMBO reports **4**, 1144-1149 (2003).

150. C. Eggeling, A. Volkmer, and C. A. Seidel, "Molecular photobleaching kinetics of Rhodamine 6G by one- and two-photon induced confocal fluorescence microscopy," Chemphyschem : a European journal of chemical physics and physical chemistry **6**, 791-804 (2005).

151. K. König, H. Liang, M. W. Berns, and B. J. Tromberg, "Cell damage in near-infrared multimode optical traps as a result of multiphoton absorption," Opt Lett **21**, 1090-1092 (1996).

152. R. J. Thomas, G. D. Noojin, D. J. Stolarski, R. T. Hall, C. P. Cain, C. A. Toth, and B. A. Rockwell, "A comparative study of retinal effects from continuous wave and femtosecond mode-locked lasers," Laser Surg Med **31**, 9-17 (2002).

153. A. A. Oraevsky, L. B. Da Silva, A. M. Rubenchik, M. D. Feit, M. E. Glinsky, M. D. Perry, B. M. Mammini, W. Small, and B. C. Stuart, "Plasma mediated ablation of biological tissues with nanosecond-to-femtosecond laser pulses: relative role of linear and nonlinear absorption," Ieee J Sel Top Quant **2**, 801-809 (1996).

154. W. Watanabe, N. Arakawa, S. Matsunaga, T. Higashi, K. Fukui, K. Isobe, and K. Itoh, "Femtosecond laser disruption of subcellular organelles in a living cell," Opt. Express **12**, 4203-4213 (2004).

155. C. L. Arnold, A. Heisterkamp, and H. Lubatschowski, "Modeling Nonlinear Plasma Formation for Femtosecond Processing of Transparent Materials and Biological Cells at High NA Focusing," J Laser Micro Nanoen **4**, 39-44 (2009).

156. K. Kuetemeyer, R. Rezgui, H. Lubatschowski, and A. Heisterkamp, "Influence of laser parameters and staining on femtosecond laser-based intracellular nanosurgery," Biomed. Opt. Express **1**, 587-597 (2010).

157. U. K. Tirlapur and K. Konig, "Femtosecond near-infrared laser pulse induced strand breaks in mammalian cells," Cell Mol Biol **47 Online Pub**, OL131-134 (2001).

158. C. B. Schaffer, N. Nishimura, E. N. Glezer, A. M. T. Kim, and E. Mazur, "Dynamics of femtosecond laser-induced breakdown in water from femtoseconds to microseconds," Opt Express **10**, 196-203 (2002).

159. N. Nishimura, C. B. Schaffer, and D. Kleinfeld, "In vivo manipulation of biological systems with femtosecond laser pulses," P Soc Photo-Opt Ins **6261**, 62611J-62611J (2006).

160. A. Uchugonova, K. Konig, R. Bueckle, A. Isemann, and G. Tempea, "Targeted transfection of stem cells with sub-20 femtosecond laser pulses," Opt. Express **16**, 9357-9364 (2008).

161. S. Kalies, K. Kuetemeyer, and A. Heisterkamp, "Mechanisms of high-order photobleaching and its relationship to intracellular ablation," Biomed. Opt. Express **2**, 805-816 (2011).

162. J. Jiao and Z. X. Guo, "Analysis of plasma-mediated ablation in aqueous tissue," Appl Surf Sci **258**, 6266-6271 (2012).

163. A. A. Voronin and A. M. Zheltikov, "Ionization penalty in nonlinear optical bioimaging," Phys Rev E **81**, 051918 (2010).

164. V. Venugopalan, A. Guerra, 3rd, K. Nahen, and A. Vogel, "Role of laser-induced plasma formation in pulsed cellular microsurgery and micromanipulation," Physical review letters **88**, 078103 (2002).

165. A. Vogel and V. Venugopalan, "Mechanisms of pulsed laser ablation of biological tissues," Chem Rev **103**, 577-644 (2003).

166. K. König, U. Simon, and K. J. Halbhuber, "3D resolved two-photon fluorescence microscopy of living cells using a modified confocal laser scanning microscope," Cell Mol Biol **42**, 1181-1194 (1996).

167. K. McCall, J. S. Baum, K. Cullen, and J. S. Peterson, "Visualizing Apoptosis," in *Drosophila Cytogenetics Protocols*, D. S. Henderson, ed. (Humana Press, Totowa, New Jersey, 2004), pp. 431-442.

168. K. McCall, J. S. Peterson, and T. L. Pritchett, "Detection of Cell Death in Drosophila," in *Apoptosis: Methods and Protocols, Second Edition*, P. Erhardt and A. Toth, eds. (Humana Press, Totowa, NJ, 2009), pp. 343-356.

169. J. Berkson, "Application of the logistic function to bio-assay," J Am Stat Assoc **39**, 357-365 (1944).

170. R. Galli, O. Uckermann, E. F. Andresen, K. D. Geiger, E. Koch, G. Schackert, G. Steiner, and M. Kirsch, "Intrinsic Indicator of Photodamage during Label-Free Multiphoton Microscopy of Cells and Tissues," Plos One **9**, e110295 (2014).

171. D. Pestov, Y. Andegeko, V. V. Lozovoy, and M. Dantus, "Photobleaching and photoenhancement of endogenous fluorescence observed in two-photon microscopy with broadband laser sources," J Optics-Uk **12**(2010).

172. D. Debarre, N. Olivier, W. Supatto, and E. Beaurepaire, "Mitigating Phototoxicity during Multiphoton Microscopy of Live Drosophila Embryos in the 1.0-1.2 mu m Wavelength Range," Plos One **9**, e104250 (2014).

173. J. Eng, R. M. Lynch, and R. S. Balaban, "Nicotinamide adenine dinucleotide fluorescence spectroscopy and imaging of isolated cardiac myocytes," Biophys J **55**, 621-630 (1989).

174. B. Chance, P. Cohen, F. Jobsis, and B. Schoener, "Intracellular oxidation-reduction states in vivo," Science **137**, 499-508 (1962).

175. K. Konig, P. T. C. So, W. W. Mantulin, B. J. Tromberg, and E. Gratton, "Two-photon excited lifetime imaging of autofluorescence in cells during UVA and NIR photostress," J Microsc-Oxford **183**, 197-204 (1996).

176. A. R. McNamara, K. D. Zamba, J. C. Sokolich, A. D. Jaskille, T. D. Light, M. A. Griffin, and D. K. Meyerholz, "Apoptosis is Differentially Regulated by Burn Severity and Dermal Location," J Surg Res **162**, 258-263 (2010).

177. G. Gravante, D. Deloyu, M. B. Palmieri, G. Santeusanio, A. Montone, and G. Esposito, "Inverse relationship between the apoptotic rate and the time elapsed from thermal injuries in deep partial thickness burns," Burns **34**, 228-233 (2008).